Durham E-Theses

Development of non-local density functional methods

Jochym, Dominik Bogdan

Development of Non-Local Density Functional Methods

Dominik Bogdan Jochym

A thesis submitted for the degree of

Doctor of Philosophy
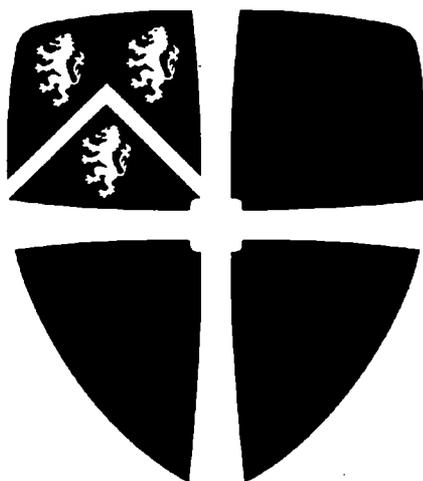
Department of Physics

University of Durham

2008

1 6 MAR 2009

Abstract

Density functional theory (DFT) is a popular approach to solving the many-electron Schrödinger equation, in order to investigate the properties of matter from first principles. While DFT can give the exact ground state electronic density of a system, in practice, an approximation is required for the many-body effects contained in the exchange-correlation functional. The accuracy of calculations performed using DFT is strongly related to the choice of approximation. In this thesis we will investigate and build upon a fully non-local approach to modeling exchange-correlation in the form of the weighted density approximation (WDA). Central to the WDA is the model function chosen for the coupling-constant averaged pair-correlation function (PCF). We show that a model PCF can be selected from a set to give excellent bulk properties for a particular system. However, this model is not necessarily transferable to other systems and there is no method of selecting an appropriate model from this set *a priori*. We suggest that the model PCF can be improved systematically by satisfying known physical constraints. One such constraint is the Kimball cusp condition, which we include in our model and implement. We demonstrate that surfaces are systems that require a non-local treatment of exchange-correlation by applying the WDA to metal surfaces and investigate the dissociative adsorption of H_2 on the Cu(100) surface. A new framework for a model PCF with spin resolution is developed, providing a route for more physical constraints to be satisfied within a weighted spin density approximation (WSDA). A simple model is suggested and implemented and comparisons are made to the coupling-constant averaged PCF in the homogeneous electron gas. We then apply a selection of our new models to a number of materials and show that our model for the WSDA gives improved band gaps over the local density approximation. Application of the WSDA to spin polarised materials reveals shortcomings in our simple model. We then suggest further refinements to our implementation of the WSDA. It is expected that the inclusion of additional physical constraints will systematically improve results given in a weighted-density based approximation to exchange-correlation.

Declaration

I confirm that the work undertaken in this thesis, at the Department of Physics, University of Durham, has not previously been submitted for a degree at this or any other university. This thesis is the original work of the author unless stated otherwise.

D. B. Jochym

December 2008

Acknowledgements

I would like to extend my thanks to Stewart Clark for his supervision over the past few years. Thanks also to the members of the condensed matter theory group both past and present. Particularly, Mike Gibson for invaluable discussions, and Dawn Geatches and Claire Platts for bearing the brunt of thesis related rants.

Thanks to all those who have been involved with the various badminton clubs during my time in Durham. I am indebted to all those who have asked me for computer help over the years – much was learned while solving those problems. Finally, I would like to thank my family and friends for their support throughout.

Look at me still talking when there's science to do...

Jonathan Coulton, "Still Alive"

Publications

This thesis has contributed to work being published or to be submitted for publication:

Dominik B. Jochym and Stewart J. Clark, *Exchange-correlation holes in metal surfaces using nonlocal density-functional theory*, Phys. Rev. B, **76**, 075411, (2007).

D. B. Jochym and S. J. Clark, *A fully nonlocal implementation of the weighted density approximation with spin resolution*, to be submitted.

D. B. Jochym and S. J. Clark, *Inclusion of the Kimball cusp condition in the weighted density approximation*, to be submitted.

D. B. Jochym and S. J. Clark, *Dissociative adsorption of H_2 on $Cu(100)$ surface using nonlocal density functional theory*, to be submitted.

Contents

List of Figures

List of Tables

Chapter 1

Introduction

The rapid increase in computer processing power and use of parallel computing are allowing larger and more complex numerical simulations to be feasible. Simulation methods are being used to so much success that they are providing what can be seen as a "third way", after experimentation and theory, of exploring nature. As they can be based in theory and/or on empirical models, numerical simulations can provide a bridge between the interpretation of experimental data and theoretical models, while remaining complementary to both. This thesis will look at the application of numerical simulations to the calculation of electronic structure in condensed matter systems.

Specifically, we will focus on density functional theory (DFT), one of the more popular approaches to solving the many-electron problem. We can use this method to investigate the physical properties of matter from first principles, providing accurate simulations of matter without bias from expectations associated with knowledge of experimental results. It is a general method that can be applied to many condensed matter systems of interest. This includes, but is not limited to, semiconductors, magnetic materials, pharmaceuticals and biological chemistry. An advantage of such simulations is that materials that may be prohibitively expensive to produce for experiment can be investigated computationally. This would be particularly useful in studies that, if done experimentally, would require much trial and error or in investigations of a large number of similar materials. Conditions that can not be produced in the laboratory can also be simulated, for example, the high pres-

sures found in the centre of our and other planets can create structures we cannot produce experimentally. Physical properties of these structures, such as elastic constants, can be predicted and used by seismologists to further knowledge of vibrations propagating through the Earth.

1.1   Many-Body Quantum Mechanics

Quantum mechanics has proven to be one of the most accurate theories in physics, providing a description of matter beyond the classical, to systems on the atomic scale. Mathematically, a system can be described by its wavefunction, Ψ, which contains the probability amplitude for each configuration of the constituent particles. In condensed matter systems, this must account for all the nuclei and the associated electrons:

$$\Psi\left(r_1, r_2, \ldots, r_N, R_1, R_2, \ldots, R_I\right),\tag{1.1}$$

where time dependance is omitted, r_N are positions (including spin information) for all N electrons and R_I are positions for all I nuclei. The time evolution of a wavefunction is described by the Schrödinger equation (ignoring relativistic effects):

$$i\frac{\partial}{\partial t}\Psi = \hat{H}\Psi,\tag{1.2}$$

where we abbreviate the many-body wavefunction as Ψ and $\hat{H}$ is the many-body hamiltonian. Throughout this thesis we will use atomic units, unless specified otherwise, where Planck's constant $\hbar$, the electron charge e, the electron mass m_e, the Bohr radius a_0, Coulomb's constant $1/(4\pi\varepsilon_0)$ and the Hartree energy are all set to unity. The last two quantities are not independent of the first four and take a value of unity as a consequence of normalising the first four.

The hamiltonian operator can be split into a sum of kinetic energy and potential operators, $\hat{T}$ and $\hat{V}$, respectively. The many-body kinetic energy operator can be

expressed as:

$$\hat{T} = -\frac{1}{2} \left(\sum_N \nabla_N^2 + \sum_I \frac{1}{M_I} \nabla_I^2 \right), \tag{1.3}$$

where M_I are the masses of the nuclei and the Laplacian operator for electron N in Cartesian coordinates is:

$$\nabla_N^2 = \frac{\partial^2}{\partial x_N} + \frac{\partial^2}{\partial y_N} + \frac{\partial^2}{\partial z_N}. \tag{1.4}$$

The potential energy operator, neglecting any external fields, is made up of the Coulomb interactions between electrons and nuclei:

$$\hat{V} = \sum_{N,I} \frac{Z_I}{|r_N - R_I|} + \frac{1}{2} \sum_{N \neq M} \frac{1}{|r_N - r_M|} + \frac{1}{2} \sum_{I \neq J} \frac{Z_I Z_J}{|R_I - R_J|}. \tag{1.5}$$

The three terms are the electron-nuclear, electron-electron and nuclear-nuclear interactions, respectively. The factors of a half are to account for double counting of the individual interactions and Z_I are the nuclear charges.

As the nuclei are much more massive than the electrons, we can assume the nuclei are stationary on the timescale of electronic relaxation – this is the Born-Oppenheimer approximation [1]. This allows the nuclear degrees of freedom to be separated from the electronic ones, thus:

$$\Psi(r_1, r_2, \ldots, r_N, R_1, R_2, \ldots, R_I) = \psi(r_1, r_2, \ldots, r_N)\phi(R_1, R_2, \ldots, R_I), \tag{1.6}$$

where we represent the many-electron and nuclei wavefunctions as ψ and ϕ, respectively. The nuclear kinetic energy term can then be set to zero and the nuclear-nuclear term can be considered a constant.

Ideally, we can then use the many-body wavefunction to give *ab initio* predictions for our chosen condensed matter systems. This means that we can get physical properties of matter without any prior bias, i.e. a first principles approach that uses only the fundamental physical interactions of particles. The challenge we face is in finding a wavefunction that satisfies the Schrödinger equation, a task that is analytically impossible for all but the most trivial of systems. Even attempts to solve the problem numerically are unfeasible as we still have $3N$ electronic degrees of freedom to take into account. Here we turn to a popular approach to the problem, DFT.

1.2 Density Functional Theory

Density functional theory (DFT), in the Hohenberg-Kohn-Sham formulation [2, 3], has established itself as the what is probably the most popular of approaches for electronic structure calculations. Essentially, it takes the time independant Schrödinger equation for the electrons:

$$\hat{H}\psi = E\psi, \tag{1.7}$$

and recasts it in terms of the electron density, which can be determined from the electronic wavefunction:

$$n(r) = N \sum_{\sigma} \int dr_2 \ldots \int dr_N \psi^*(r_1, r_2, \ldots, r_N) \psi(r_1, r_2, \ldots, r_N), \tag{1.8}$$

where we include the sum over spin coordinate σ. The system can then be treated as N single particle equations, as we will see in the following discussion. It is then possible to determine, in principle, the exact ground state of the system. At this point it should be pointed out that this discussion is by no means intended to be pedagogical. In-depth reviews of DFT can be found in references [4] and [5], and references therein.

1.2.1 The Hohenberg-Kohn Theorems

The two Hohenberg-Kohn theorems [2] are the first step in constructing a successful DFT. We start by writing the hamiltonian for a general many-electron system in an external potential $v(r_N)$, as:

$$\hat{H} = -\frac{1}{2}\sum_N \nabla_N^2 + \sum_N v(r_N) + \frac{1}{2}\sum_{N \neq M} \frac{1}{|r_N - r_M|},$$

(1.9)

where the external potential is for all effects external to the electrons, including the Coulomb potential from the stationary nuclei, but other fields could be applied also.

Theorem 1: The external potential is a unique functional of the electron density in the ground state, and therefore the total energy is also a functional of the ground state electron density. A consequence of the first Hohenberg-Kohn theorem is that all properties of a system are determined from only the ground state electron density.

Proof: We proceed by *reductio ad absurdum*, following reference [2]. We have a ground state electronic wavefunction ψ that gives an electron density $n(r)$ for an external potential $v(r)$. Assume we have a second external potential $v'(r)$ that has a ground state ψ', which gives the same density $n(r)$. The corresponding hamiltonian and ground state energy for ψ, ψ' are $\hat{H}$, $\hat{H}'$ and E, E', respectively. As ψ' is not the ground state of $\hat{H}$, we can say that:

$$E = \langle\psi|\hat{H}|\psi\rangle < \langle\psi'|\hat{H}|\psi'\rangle = \langle\psi'|\hat{H}'|\psi'\rangle + \langle\psi'|\hat{H} - \hat{H}'|\psi'\rangle \quad (1.10)$$

$$= E' + \int [v(r) - v'(r)]\, n(r)dr, \quad (1.11)$$

so we have:

$$E < E' + \int [v(r) - v'(r)]\, n(r)dr. \quad (1.12)$$

If the unprimed and primed indices are reversed, we also have:

$$E' < E + \int \left[v'(r) - v(r) \right] n(r) dr. \tag{1.13}$$

Addition of equations 1.12 and 1.13 leads to the contradiction:

$$E + E' < E' + E. \tag{1.14}$$

So, to within a constant, the external potential $v(r)$ is a unique functional of the ground state electron density $n(r)$, as was set out to be shown.

Theorem 2: The total energy of a system, which is a functional of the ground state electron density through the first theorem, is minimised for the correct ground state energy. Hohenberg and Kohn defined a universal functional, that is valid for any system of electrons, regardless of the external potential. For a given external potential, $v(r)$, we have the total energy functional $E[n]$ as:

$$E[n] = F[n] + \int v(r) n(r) dr, \tag{1.15}$$

where we neglect the energy from the interaction of the nuclei. The universal functional $F[n]$ includes all of the electronic energy:

$$F[n] = T[n] + V_{ee}[n], \tag{1.16}$$

where we have the kinetic energy functional $T[n]$ and the potential energy functional $V_{ee}[n]$ from electron-electron interactions.

For a system with a ground state electron density $n(\mathbf{r})$, the ground state energy E is equivalent to the total energy functional $E[n]$, which is equal to the expectation value of the hamiltonian for the ground state wavefunction ψ, thus:

$$E = E[n] = \langle \psi | \hat{\boldsymbol{H}} | \psi \rangle. \tag{1.17}$$

For a different density $n'(\mathbf{r})$, with wavefunction ψ', it follows from the variational principle that the energy corresponding to this state, E' is greater than the ground state energy:

$$E = \langle \psi | \hat{\boldsymbol{H}} | \psi \rangle < \langle \psi' | \hat{\boldsymbol{H}} | \psi' \rangle = E'. \tag{1.18}$$

Therefore the total energy functional $E[n]$ gives the exact ground state energy only for the exact ground state density. If the universal functional $F[n]$ is known, then the total energy can be minimised with respect to $n(\mathbf{r})$ and the exact ground state electron density and total energy would be found. Simple yet powerful as the Hohenberg-Kohn theorems are, they do not provide a route to construct functionals or a method to calculate the ground state density.

1.2.2 The Kohn-Sham Formulation

Almost exactly a year after the Hohenberg-Kohn theorems were published, Kohn and Sham published [3] an approach that makes DFT feasible. The Kohn-Sham ansatz is that the exact ground state density can be written as the ground state density of a fictitious system of noninteracting particles. This then gives us a set of independent particle equations that can be solved numerically. Through the Hohenberg-Kohn theorems, these independent particle equations have their own ground state energy functional. Kohn and Sham chose to write the total energy functional as:

$$E[n] = \int v(\mathbf{r})n(\mathbf{r})d\mathbf{r} + \frac{1}{2}\int\int \frac{n(\mathbf{r})n(\mathbf{r}')}{|\mathbf{r}-\mathbf{r}'|}d\mathbf{r}d\mathbf{r}' + T_s[n] + E_{\mathrm{xc}}[n]. \tag{1.19}$$

We have the external potential, $v(\boldsymbol{r})$, introduced earlier, the classical Coulomb interaction energy for the electron density with itself (the Hartree energy), and the kinetic energy of the independent particles. Here, all the many-body effects of the electron-electron interactions are combined into a single entity called the exchange-correlation energy functional.

By definition, the exchange-correlation energy is the difference between the exact total energy and the other known quantities. Physically, it is the energy from Pauli exclusion and many-body Coulomb interactions, which must include a self interaction term required to cancel that in the Hartree energy. It also includes the difference between the many-body and single particle kinetic energies. In principle, the Kohn-Sham formulation can allow the exact ground state to be determined. However, the form of the exchange-correlation energy functional is not known. In practice approximations are made so that DFT can be used for physical systems. Discussion of these approximations will be postponed until Chapter 2.

Kohn-Sham DFT gives a set of variational equations that are solved self consistently. We have a set of Schrödinger like equations:

$$\hat{H}_{\text{KS}}\psi_i(\boldsymbol{r}) = \varepsilon_i\psi_i(\boldsymbol{r}), \tag{1.20}$$

for the independent particle Kohn-Sham orbitals $\psi_i(\boldsymbol{r})$ governed by an effective hamiltonian $\hat{H}_{\text{KS}}$ with eigenvalues ε_i. Note that we neglect spin indices for brevity. The Kohn-Sham orbitals are related to the electron density of N electrons by:

$$n(\boldsymbol{r}) = \sum_i^N |\psi_i(\boldsymbol{r})|^2, . \tag{1.21}$$

and, in principle, this density is exact. The effective hamiltonian is given by:

$$H_{\text{KS}}(\boldsymbol{r}) = -\frac{1}{2}\nabla^2 + v_{\text{KS}}(\boldsymbol{r}), \tag{1.22}$$

where we have the effective Kohn-Sham potential:

$$v_{KS}(\mathbf{r}) = v_{ext}(\mathbf{r}) + v_H(\mathbf{r}) + v_{xc}(\mathbf{r}), \tag{1.23}$$

which is the sum of the external, Hartree and exchange-correlation potentials, respectively. A self consistent iterative procedure would start from an initial electron density that can be used to calculate the Kohn-Sham potential. Then, through solution of equation 1.20, and use of the relation in equation 1.21 we can obtain a new electron density. If the initial and new densities are identical, then the ground state density has been found. Otherwise one must select a new trial density through minimisation of the total energy and continue to repeat the iterative procedure.

In practice, such a self consistent calculation must be performed computationally, we will now discuss a popular approach to doing this – the plane wave pseudopotential method.

1.3 Plane Wave Pseudopotential Method

One way of implementing the Kohn-Sham formulation of DFT is the plane wave pseudopotential method. As with the previous section, this discussion is not intended to be pedagogical and the interested reader will find reviews in references [4] and [5], and references therein.

1.3.1 Plane Waves as a Basis

When studying the electronic structure of condensed matter systems, one is investigating the behaviour of a number of electrons in the order of $\sim 10^{28}$ per mole of atoms. Many extended systems are periodic in structure, corresponding to one of the Bravais lattices, so one can define an infinite periodic system and perform calculations for only the electrons in the periodic cell.

Bloch's theorem shows that the wavefunction, ψ_n, of an electron in band n, for a periodic system can be expressed as a combination of a plane wave part and a

periodic cell part [6]:

$$\psi_n(\boldsymbol{r}) = u_n(\boldsymbol{r})e^{i\boldsymbol{k}\cdot\boldsymbol{r}}, \tag{1.24}$$

where the plane wave part has wave vector $\boldsymbol{k}$, which is confined to the first Brillouin zone. The periodic part has the same periodicity as the lattice, i.e. $u_n(\boldsymbol{r} + \boldsymbol{R}) = u_n(\boldsymbol{r})$, where $\boldsymbol{R}$ is one of the lattice vectors.

This leads us to choose a plane wave basis set to describe the wavefunction within the periodic cell. The periodic part of the wavefunction can then be written as:

$$u_n(\boldsymbol{r}) = \sum_{\boldsymbol{G}} c_{n,\boldsymbol{G}} e^{i\boldsymbol{G}\cdot\boldsymbol{r}}, \tag{1.25}$$

where we have plane wave coefficients $c_{n,\boldsymbol{G}}$ and $\boldsymbol{G}$ are the reciprocal lattice vectors that satisfy the relation $\boldsymbol{G}\cdot\boldsymbol{R} = 2\pi m$, where m is an integer. If we combine equations 1.24 and 1.25, the Kohn-Sham orbitals can therefore be written as an infinite sum of plane waves:

$$\psi_n(\boldsymbol{r}) = \sum_{\boldsymbol{G}} c_{n,(\boldsymbol{k}+\boldsymbol{G})} e^{i(\boldsymbol{k}+\boldsymbol{G})\cdot\boldsymbol{r}}, \tag{1.26}$$

where $c_{n,\boldsymbol{k}+\boldsymbol{G}}$ are the coefficients of the plane waves describing the wavefunction.

Bloch's theorem allows us to take an infinite system but only calculate a finite number of electronic wavefunctions. However, this leaves an infinite number of k-points as each electron occupies a definite $\boldsymbol{k}$. In practice, we need only choose a sample of k-points as the wavefunction varies slowly over small regions of k-space. The electronic wavefunctions at k-points that are close will be nearly identical. Therefore a region of k-space can be represented by the wavefunction at a single k-point. Efficient k-point sampling schemes have been developed, such as the one given by Monkhorst and Pack [7]. The symmetry of the lattice can be used to reduce the number of k-points required. The Brillouin zone can be made irreducible

by applying the point group symmetries of the lattice, leaving no k-points related by symmetry.

The sum over G vectors in equation 1.26 is infinite in order to fully describe the wavefunction, i.e. for the plane wave basis set to be complete. When devising a computational implementation one must choose a finite end to the sum. For most realistic wavefunctions, there will be a scale below which the wavefunction can be described as smoothly varying. This means that the coefficients $c_{n,k+G}$ will become small for large $|k + G|$. The cutoff point is referred to as the plane wave kinetic energy cutoff:

$$E_{cut} \geq \frac{1}{2}|k + G|^2, \tag{1.27}$$

i.e. it is greater than or equal to the highest kinetic energy of the plane waves used. This corresponds to a sphere in reciprocal space within which all the used $|k + G|$ vectors lie.

When performing calculations one must always be careful to select an appropriate sampling of k-points and plane wave cutoff energy. This is done by performing calculations at successively higher cutoff energies and finer grids of k-points until the quantities of interest no longer change – a test of convergence. An example of this for the total energy of silicon in the diamond structure is shown in Figure 1.1.

The use of plane waves as a basis set is advantageous in a number of ways. In terms of the accuracy required for the system in question, one can always improve the accuracy by increasing the plane wave cutoff energy and therefore tending towards the complete basis set. Real space quantities, such as potentials, can be easily transformed to reciprocal space using standard numerical techniques, in order to obtain the plane wave coefficients. Derivatives in real space become multiplications in reciprocal space, so quantities such as the kinetic energy of the Kohn-Sham orbitals can be easily evaluated. The use of plane waves treats all regions of space equally, so can be applied generally, even for non-periodic systems, if an appropriate periodic supercell is used. We make use of this in our investigation of surfaces in Chapter 3. A simple schematic of the supercell approximation is shown in Figure 1.2. However,
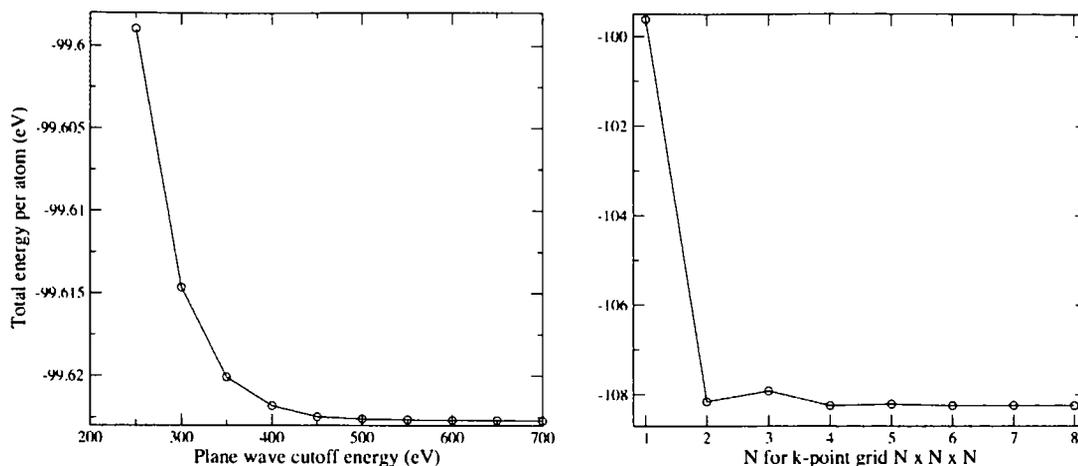
Figure 1.1: Graphs for the total energy per atom in silicon against plane wave cutoff energy and k-point grid size.

this includes regions of vacuum, so there is an added memory and computational cost in such cases. A plane wave basis set also lends well to distribution of data and processing in a parallel computing environment. This allows larger and more complicated systems to be simulated with higher accuracy.

1.3.2 The Pseudopotential Approximation

Electrons in the vicinity of the nuclei will be under the influence of a steep Coulomb potential and have rapidly varying wavefunctions in the nuclear regions. This requires a correspondingly large number of plane waves to adequately describe the wavefunction and the nuclear potential. This expense is reduced by the pseudopotential approximation [8, 9, 10], taking the number of plane waves required down by many orders of magnitude.

We can consider the electrons in condensed matter to be of two categories – core and valence. Core electrons are those that are localised in the vicinity of the nucleus, essentially those in closed shells. Valence electrons are those outside the core region and for most situations are responsible for the physical properties of a system. As the core electrons are left unchanged in most situations they can be replaced, along with the nuclear potential, to create a relatively weak pseudopotential. This pseudopotential acts on a set of pseudo wavefunctions that, outside of a specified
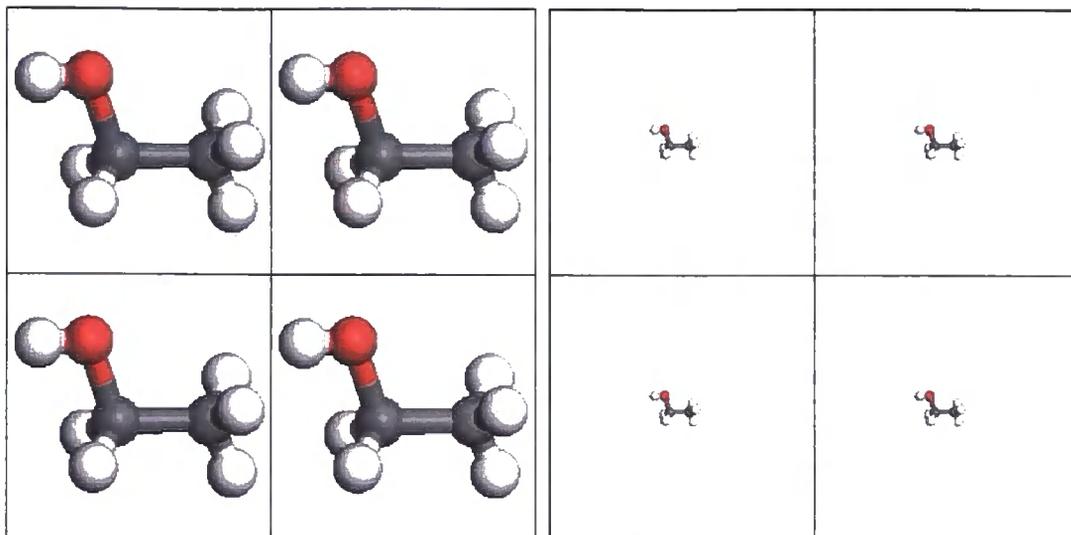
Figure 1.2: A schematic of the supercell approximation. Vacuum padding of the cell reduces the effect of the molecule "seeing" its own image in the next repeating unit. Here we have increased the size of the right hand cell by five times over the left hand cell. The same principle can be applied to defects in solids and to surfaces.

core radius, are identical to the wavefunctions where all the electrons are taken into account. These pseudo wavefunctions have no nodes in the core region, and therefore greatly reduces the number of plane waves required for the calculation by many orders of magnitude. The memory required for the calculation is also reduced because there are fewer Kohn-Sham orbitals required, as the core electrons are not explicitly treated. An example of a pseudo wavefunction and pseudopotential compared to the all-electron counterparts are shown in Figure 1.3.

There are a number of methods popularly used to construct pseudopotentials. The two most widely used methods are the norm-conserving approach of Kleinman and Bylander [11] and the ultrasoft approach of Vanderbilt [12]. Norm-conservation refers to the constraint that the charge within the core radius for the true system is equal to the charge within the core radius for the pseudo wavefunction. With ultrasoft pseudopotentials this constraint is relaxed and therefore a more slowly varying pseudopotential can be chosen, further reducing the number of plane waves required. Ultrasoft pseudopotentials also show better transferability between dif-
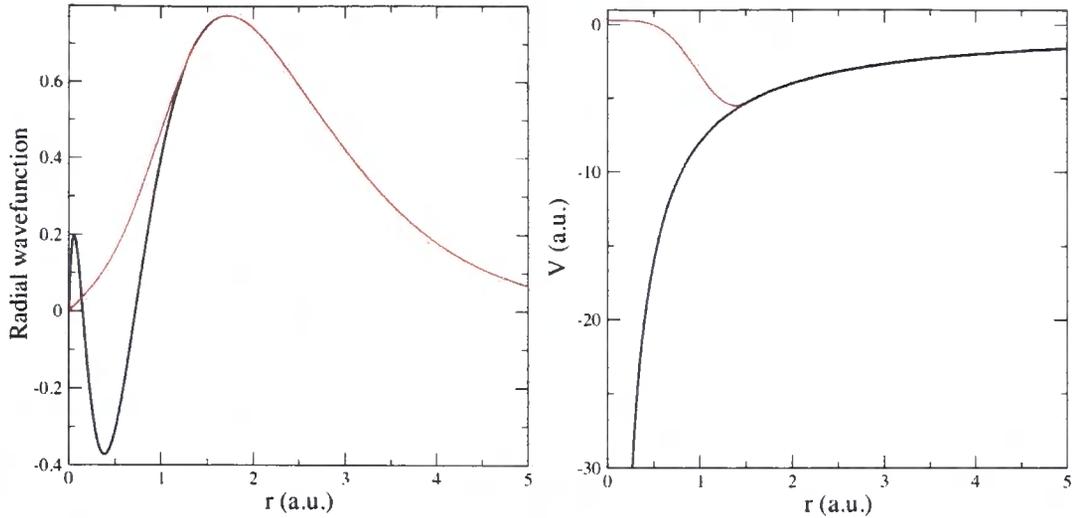
Figure 1.3: Left: The all-electron wavefunction (black) and pseudo wavefunction (red) for the 3s orbital in Si. Right: The all-electron potential (black) and the pseudopotential felt by the pseudised 3s state (red).

ferent condensed matter systems [12]. In this thesis we will generally use ultrasoft pseudopotentials because of these benefits.

1.3.3 Minimisation of the Total Energy

The Kohn-Sham equations (equation 1.20) become a problem of matrix diagonalisation when expressed in terms of plane waves. However, numerical algorithms for matrix diagonalisation do not scale well with the size of the matrix in question. This both limits the number of plane waves and number of atoms in the periodic cell that can be practically used. Alternative methods involve direct minimisation of the Kohn-Sham total energy functional. This is done through variation of the plane wave coefficients of the Kohn-Sham orbitals while ensuring that each band is orthogonal to the others.

Among those methods one of the most efficient is the conjugate gradients technique [13]. This proceeds by taking an initial search direction to be that with the steepest gradient for the function and variable in question. That line is then followed to find the minimum. Subsequent search directions are then chosen such that they are independent of any previous minimisation directions. This then guarantees the

minimum will be found in the same number of steps as there are dimensions in the system. In practice, each band is treated one at a time to save memory costs in computation, made possible by keeping the bands orthogonal.

The minimisation procedure can be improved by using a preconditioning scheme [14, 15]. This is because the plane waves with high kinetic energy dominate the search directions even though the corresponding coefficients in the wavefunction are small. Preconditioning is generally performed through multiplying the hamiltonian by a diagonal matrix consisting of the inverse kinetic energy operator for the high kinetic energy plane waves and a constant for the low kinetic energy plane waves. For the high kinetic energy plane waves, the energies will be dominated by the kinetic energy so any errors introduced by such an approximate preconditioning matrix will be small. In practice this allows convergence within tens of iterations for a basis set containing $\sim 10^6$ plane waves.

1.4 The CASTEP Code

The calculations and methods developed in this thesis were performed using, and implemented in, CASTEP [16, 17]. It is an implementation of the plane wave pseudopotential approach to Kohn-Sham DFT using the methods summarised above. CASTEP also provides a vast range of tools for obtaining meaningful physical quantities from the ground state electronic wavefunction. The code is written in Fortran 90 as a complete re-implementation of the original Fortran 77 CAmbridge Serial Total Energy Package, allowing for better maintainability and increased speed of development. It makes use of efficient implementations of linear algebra and fast Fourier transform libraries. It is also designed to run in parallel using data distribution schemes that parallelise over G-vectors, k-points and, most recently, bands [18].

1.5 Summary and Outline of Thesis

In this chapter we have briefly introduced the many-body problem in quantum mechanics and the formally exact solution provided by the Kohn-Sham formulation of

density functional theory. The plane wave pseudopotential method of performing DFT calculations was discussed. One of the numerical methods used in minimising the total energy was mentioned. The implementation of the above in CASTEP was introduced. Much of the remainder of this thesis will be dedicated to discussing approximations used for the exchange-correlation energy functional and, in particular, the development and implementation of a non-local description of exchange and correlation. The outline of the thesis is as follows:

Chapter 2

We begin by discussing a number of the popular and currently available approaches to approximating the exchange-correlation energy functional. We then introduce the fully non-local weighted density approximation (WDA) and derive the required parts for an implementation in the context of a plane wave basis set. A number of possible model pair-correlation functions for use in the WDA are described and extensively applied to calculate bulk properties of copper. Improving model pair-correlation functions through including known physical constraints is suggested. One such constraint, the Kimball cusp condition, is incorporated into our model pair-correlation functions, implemented, tested, and applied to bulk silicon.

Chapter 3

There are many condensed matter systems that require non-local interactions to be described accurately. Here we apply the WDA to surface systems. Specifically we demonstrate that the exchange-correlation hole for metallic surfaces is highly non-local. We then apply the WDA to obtain part of the potential energy surface describing the dissociative adsorption of H_2 on Cu(100). Comparisons are made between results obtained with the local density approximation (LDA) and the WDA.

Chapter 4

We derive a new framework for model pair-correlation functions in the WDA that includes spin resolution. This weighted spin density approximation (WSDA) pro-

vides an avenue for refining the approximation by satisfying constraints on the spin resolved pair-correlation function as well as allowing spin polarised systems to be studied. An initial implementation of the WSDA is proposed.

Chapter 5

The homogeneous electron gas, while fictitious, is valuable in constructing and testing exchange-correlation energy functionals. It provides a known physical limit that some would argue that all approximations to exchange-correlation should fulfill. We compare the spin resolved pair-correlation function for our implementation of the WSDA with quantum Monte-Carlo data for the pair-correlation function in the uniform electron gas. On-top values of the pair-correlation function are compared for a number of models. The importance of including a modified cusp condition when describing the coupling-constant averaged pair-correlation function is emphasised. An implementation of the modified cusp condition is then added to our WSDA. The coupling-constant averaged pair-correlation function in our WSDA model is compared to a first principles model at a number of uniform densities and spin polarisations.

Chapter 6

The WDA including the cusp condition from Chapter 2 is extended to include the modified cusp condition. The bulk properties and electronic band structure of silicon and germanium are calculated and compared for our new model functionals. Band gaps for a number of materials are calculated with our modified cusp WDA and WSDA to be compared with the LDA. The WSDA will then be applied to spin polarised systems in the form of iron and iron(II) oxide.

Chapter 7

Finally, we will summarise the conclusions of the previous chapters and discuss possibilities for refinement of the models in future work.

Chapter 2

Exchange-Correlation Functionals

As discussed in the previous chapter, DFT allows us, in principle, to solve the many-electron Schrödinger equation exactly. In practice approximations are made, and a (by no means exhaustive) discussion of these will make up the first part of this chapter. We will then describe in detail a non-local functional called the weighted density approximation (WDA). A discussion will follow on some of the functional forms that can be used within the WDA and trends within "families" of models. A possible improvement to the WDA in the form of imposing the Kimball cusp condition [19] will be implemented, tested, and applied.

2.1   Local, Semi-local and Beyond

The simplest of all the available models in DFT is the local density approximation (LDA) [3, 20]. This takes the exchange-correlation energy density at each point in space to be the same as that for a homogeneous electron gas with the electron density for that point. The LDA can also be applied to spin polarised systems [21] and is often referred to as the LSDA (local spin-density approximation). The exchange-correlation energy in the L(S)DA can be expressed as:

$$E_{\text{xc}}^{\text{LSDA}}[n_\uparrow, n_\downarrow] = \int n(r)\varepsilon_{\text{xc}}^{\text{LDA}}[n_\uparrow(r), n_\downarrow(r)]dr, \tag{2.1}$$

with the exchange-correlation energy per electron in a uniform gas with spin densities

18

$n_\uparrow(r)$ and $n_\downarrow(r)$ given by:

$$\varepsilon_{xc}^{LDA}[n_\uparrow(r), n_\downarrow(r)] = \frac{1}{2} \int n(r') \left(\bar{g}^{HEG}\left[|r - r'|, n_\uparrow(r), n_\downarrow(r)\right] - 1 \right) dr', \qquad (2.2)$$

where $\bar{g}^{HEG}$ is the coupling-constant averaged pair-correlation function in the homogeneous electron gas. The exchange energy density in the uniform limit can be determined analytically. However, the correlation energy density is only known numerically through quantum Monte Carlo calculations [22]. Parameterisations of this are available, for example, that by Perdew and Zunger [23] is widely used. In spite of its simplicity, the LDA has been and still is used to considerable success, particularly for solids, where the electron density can vary relatively slowly. This success is due to the overestimation in correlation energy being cancelled by the underestimation in that of exchange. The LDA performs less well for single atoms and molecules, as would be expected considering the highly inhomogeneous electron density in these systems. The LDA generally over binds, predicting shorter bond lengths than in experiment [24]. It also gives a non-zero contribution from correlation in single electron systems and fails to counteract the Hartree self interaction in this limit.

A natural extension beyond the LDA is to include the local density gradients $\nabla n_\uparrow(r)$ and $\nabla n_\downarrow(r)$ [25, 26, 27]:

$$E_{xc}^{GGA}[n_\uparrow, n_\downarrow] = \int n(r)\varepsilon_{xc}^{GGA}[n_\uparrow(r), n_\downarrow(r), \nabla n_\uparrow(r), \nabla n_\downarrow(r)]dr. \qquad (2.3)$$

There are many different generalised gradient approximation (GGA) functional forms available, both non-empirical and empirical. Arguably the best non-empirical GGA is that of Perdew, Burke and Ernzerhof (PBE) [26], which reverts to the LDA in the uniform limit, fulfills some exact constraints on the exchange and correlation holes, and also satisfies some exact constraints on the correlation energy. This fitting to physical constraints makes PBE much more transferable than its empirical counterparts that are fitted to perform well for a favoured set of molecules [28].

Continuing along these lines we arrive at the meta-GGA [29] that, in addition to the components in a GGA, also makes use of the Laplacians $\nabla^2 n_\uparrow(r)$ and $\nabla^2 n_\downarrow(r)$ of the electron density or the kinetic energy density τ_σ:

$$E_{\text{XC}}^{\text{GGA}}[n_\uparrow, n_\downarrow] = \tag{2.4}$$

$$\int n(r)\varepsilon_{\text{XC}}^{\text{GGA}}[n_\uparrow(r), n_\downarrow(r), \nabla n_\uparrow(r), \nabla n_\downarrow(r), \nabla^2 n_\uparrow(r), \nabla^2 n_\downarrow(r), \tau_\uparrow(r), \tau_\downarrow(r)]dr,$$

where the kinetic energy density for the occupied Kohn-Sham orbitals $\psi_{i\sigma}(r)$ are implicit functionals of the electron density:

$$\tau_\sigma(r) = \frac{1}{2} \sum_i^{occ.} |\nabla \psi_{i\sigma}(r)|^2. \tag{2.5}$$

In the limit of slowly varying density the kinetic energy density contains the same information as the Laplacians. Because of this and the ability to fit more physical constraints, the explicit dependance on the Laplacians can be neglected. A non-empirical meta-GGA comes in the form given by that of Tao, Perdew, Staroverov and Scuseria (TPSS) [30]. Tests of this functional show improvements over PBE, particularly with atomisation and surface energies [31, 32, 33, 34]. This is likely to be because TPSS has no self interaction in the single electron limit, which is not satisfied at the LDA or GGA level.

It is unclear whether including yet higher derivatives of the electron density would continue to provide improvements. In fact, there is no guarantee that an expansion of the exchange-correlation energy in this fashion is going to converge on the exact exchange-correlation functional. A popular direction is to use exact (Hartree-Fock) exchange in combination with local correlation – a so-called hybrid functional. A hybrid widely used in the chemistry community is B3LYP [35]. This functional consists of fractions of LDA exchange, Hartree-Fock exchange, Becke's density gradient correction to exchange [36], GGA correlation due to Lee, Yang and

Parr [37], and LDA correlation from the parameterisation of Vosko, Wilk and Nusair [38]. The coefficients for these components are determined from three parameters, which are often fitted to molecular data. While very successful for certain sets of molecules, the B3LYP hybrid does not transfer well to all systems. It also fails to retain the known correlation energy in the uniform limit [39], and overestimates the exchange energy in this limit.

A hybrid containing the TPSS meta-GGA has been shown to give some improvements over "plain" TPSS, but contains one empirical parameter [31]. Inclusion of Hartree-Fock exchange does allow for more physical constraints to be satisfied, but it has been argued that a so-called hyper-GGA encompassing the meta-GGA and exact exchange must contain at least one empirical parameter [40]. This suggests that even the "best" possible hyper-GGA could suffer from problems with transferability. Beyond the hyper-GGA, it has been suggested that all occupied and unoccupied Kohn-Sham orbitals can be used to construct a generalised random phase approximation (RPA) [41, 42, 43, 44]. This addition of the unoccupied orbitals removes the need for empiricism that is unavoidable in a hyper-GGA [40, 45].

One can also perform a non-local treatment of exchange and correlation by screening the effect of Hartree-Fock exchange at long range [46, 47]. This models some of the effects of correlation by performing an exponential cutoff of the exchange energy. An LDA treatment of the local exchange-correlation energy is also included. The exact exchange (EXX) functional [48, 49, 50] is not to be confused with Hartree-Fock exchange. The distinction comes from Hartree-Fock using a non-local operator while EXX uses only a local potential. However, both methods do treat exchange exactly. Implementations of EXX often contain an LDA treatment of correlation and requires an implementation of the optimised effective potential (OEP) method [51, 52] in order to be applied self consistently.

The weighted density approximation (WDA) [53, 54] takes a different approach in treating exchange and correlation non-locally. It starts from the definition of the exchange-correlation energy in terms of the Coulomb interaction between the electron density and its coupling-constant averaged exchange-correlation hole. Physically this can be pictured as the region in the vicinity of an electron that is depleted

of other electrons through the effects of Pauli exclusion and Coulomb repulsion. An approximation is then made in an attempt to model the shape of the exchange-correlation hole (in fact, the approximation is made to the pair-correlation function, which is closely related to the exchange-correlation hole) such that for a given value of a parameter at each point in space, the weighted density, the sum rule for the exchange-correlation hole is satisfied. It is also constructed such that the LDA exchange-correlation energy is regained in the homogeneous limit. This is enforced by ensuring the weighted density becomes the electron density in the homogeneous electron gas. In the next section we will go into more detail in defining the WDA.

2.2 Weighted Density Approxmination

We start from an exact definition of the exchange-correlation energy, we have:

$$E_{\mathrm{xc}}[n] = \frac{1}{2} \int n(r)dr \int \frac{n_{\mathrm{xc}}(r,r')}{|r-r'|}dr', \tag{2.6}$$

which is the Coulomb interaction between the electron density $n(r)$ and the coupling-constant averaged exchange-correlation hole $n_{\mathrm{xc}}(r,r')$:

$$n_{\mathrm{xc}}(r,r') = \int_0^1 n_{\mathrm{xc}}^\lambda(r,r')d\lambda. \tag{2.7}$$

The coupling constant λ takes us from the non-interacting Kohn-Sham system at $\lambda = 0$ to the full Coulomb interaction at $\lambda = 1$, or $\lambda = e^2$ if we were not using atomic units. We can relate the exchange-correlation hole to the pair probability density and pair-correlation function:

$$n_{\mathrm{xc}}^\lambda(r,r') = \frac{P(r,r')}{n(r)} - n(r') = n(r')[g_{\mathrm{xc}}^\lambda(r,r') - 1], \tag{2.8}$$

where $P(r,r')$ is the probability of finding electrons simultaneously at positions r

and r'. Physically, $n(r')g_{xc}^{\lambda}(r, r')dr'$ is the number of electrons expected at point r', per volume element dr', given that an electron is present at point r. Thus we can state that g_{xc}^{λ}, n_{xc}^{λ} and their coupling-constant averages must be non-negative. The coupling-constant averaged pair-correlation function has a similar relation as in equation 2.7 with 'g' substituted for 'n'.

The WDA models the coupling-constant averaged pair-correlation function to approximate the coupling-constant averaged exchange-correlation hole [53, 54]:

$$n_{xc}^{\text{WDA}}(r, r') = n(r')G^{\text{WDA}}[r, r'; \tilde{n}(r)], \tag{2.9}$$

where we will refer to G^{WDA} as the model pair-correlation function. The weighted density $\tilde{n}(r)$ is a non-local parameter determined such that the sum rule is satisfied:

$$\int n_{xc}^{\text{WDA}}(r, r')dr' = -1. \tag{2.10}$$

Gunnarsson and Jones [55] proposed a simple form for G^{WDA}:

$$G^{\text{WDA}}[r, r'; \tilde{n}(r)] = C(\tilde{n}(r))f\left(\frac{|r - r'|}{\lambda(\tilde{n}(r))}\right), \tag{2.11}$$

where f is an analytic function that varies from 1 at zero separation to zero at infinite separation. C and λ are scalar fields that describe the weighted density and take values to simultaneously satisfy the sum rule and return the LDA energy in the homogeneous limit.

2.2.1 WDA Exchange-Correlation Potential

In order to construct a self consistent implementation of the WDA, the exchange-correlation potential is required. It is the functional derivative of the exchange-

correlation energy with respect to the electron density that gives us three terms:

$$v_{\text{xc}}^{\text{WDA}}(\boldsymbol{r}) = \frac{\delta E_{\text{xc}}^{\text{WDA}}[n]}{\delta n(\boldsymbol{r})} = v_1(\boldsymbol{r}) + v_2(\boldsymbol{r}) + v_3(\boldsymbol{r}). \tag{2.12}$$

The first term, $v_1(\boldsymbol{r})$, is equivalent to the WDA exchange-correlation energy density:

$$v_1(\boldsymbol{r}) = \frac{1}{2} \int \frac{n(\boldsymbol{r}')G^{\text{WDA}}[\boldsymbol{r}, \boldsymbol{r}'; \tilde{n}(\boldsymbol{r})]}{|\boldsymbol{r} - \boldsymbol{r}'|} d\boldsymbol{r}' = \varepsilon_{\text{xc}}^{\text{WDA}}(\boldsymbol{r}). \tag{2.13}$$

The second term, $v_2(\boldsymbol{r})$, is very similar to the first and arises because the functional derivative $\delta n(\boldsymbol{r}')/\delta n(\boldsymbol{r}) = \delta(\boldsymbol{r} - \boldsymbol{r}')$, the Dirac delta function. One of the two integrals then becomes trivial and we obtain the same as 2.13 but with the weighted density taken at point $\boldsymbol{r}'$:

$$v_2(\boldsymbol{r}) = \frac{1}{2} \int \frac{n(\boldsymbol{r}')G^{\text{WDA}}[\boldsymbol{r}, \boldsymbol{r}'; \tilde{n}(\boldsymbol{r}')]}{|\boldsymbol{r} - \boldsymbol{r}'|} d\boldsymbol{r}'. \tag{2.14}$$

It should be noted that physically, the coupling-constant averaged pair-correlation function is symmetric under interchange of $\boldsymbol{r}$ and $\boldsymbol{r}'$, which means the second term would simply be $v_2(\boldsymbol{r}) = \varepsilon_{\text{xc}}(\boldsymbol{r})$. However, a model pair-correlation function like that used in equation 2.11 does not have this symmetry. This results in the large separation limit, $|\boldsymbol{r} - \boldsymbol{r}'| = r \to \infty$, of the exchange-correlation potential being:

$$\lim_{r \to \infty} v_{\text{xc}}^{\text{WDA}}(\boldsymbol{r}) = -\frac{1}{2r}, \tag{2.15}$$

which is a factor of two from the correct $-1/r$ limit.

The third potential term $v_3(\boldsymbol{r})$ takes into account the implied dependence of the weighted density on the electron density:

$$v_3(\boldsymbol{r}) = \frac{1}{2} \int n(\boldsymbol{r}')d\boldsymbol{r}' \int \frac{n(\boldsymbol{r}'')}{|\boldsymbol{r}' - \boldsymbol{r}''|} \times \frac{\delta G^{\text{WDA}}[\boldsymbol{r}', \boldsymbol{r}''; \tilde{n}(\boldsymbol{r}')]}{\delta n(\boldsymbol{r})} d\boldsymbol{r}''. \tag{2.16}$$

Using the chain rule, we can rewrite the functional derivative of the model pair-correlation function:

$$\frac{\delta G^{\text{WDA}}[r', r''; \tilde{n}(r')]}{\delta n(r)} = \frac{\partial G^{\text{WDA}}[r', r''; \tilde{n}(r')]}{\partial \tilde{n}(r')} \times \frac{\delta \tilde{n}(r')}{\delta n(r)}. \tag{2.17}$$

The derivative of the weighted density can be determined by taking the functional derivative of the sum rule, $\int n(r'') G^{\text{WDA}}[r', r''; \tilde{n}(r')] dr'' = -1$, and rearranging:

$$\frac{\delta \tilde{n}(r')}{\delta n(r)} = -\frac{G^{\text{WDA}}[r, r'; \tilde{n}(r')]}{\int n(r'') \partial G^{\text{WDA}}[r', r''; \tilde{n}(r')]/\partial \tilde{n}(r') dr''}. \tag{2.18}$$

Taking equations 2.17 and 2.18 and substituting back into equation 2.16 we obtain a form for $v_3(r)$ in terms of quantities we can calculate:

$$v_3(r) = -\frac{1}{2} \int n(r') \frac{h_1(r')}{h_2(r')} G^{\text{WDA}}[r, r'; \tilde{n}(r')] dr', \tag{2.19}$$

where the terms h_1 and h_2 are given by:

$$h_1(r') = \int \frac{n(r'')}{|r' - r''|} \frac{\partial G^{\text{WDA}}[r', r''; \tilde{n}(r')]}{\partial \tilde{n}(r')} dr'', \tag{2.20}$$

$$h_2(r') = \int n(r'') \frac{\partial G^{\text{WDA}}[r', r''; \tilde{n}(r')]}{\partial \tilde{n}(r')} dr''. \tag{2.21}$$

From this starting point, we now recast the problem to be used in the context of a plane wave pseudopotential code.

2.2.2 Implementation in Reciprocal Space

To apply the WDA efficiently for periodic systems, it should be noted that each of the integrals above are in the form of convolutions. We can therefore use the

convolution theorem to perform the integrals as multiplications in reciprocal space, using efficient numerical FFTs as needed. If we denote $\mathcal{F}$ as the Fourier transform operator, the convolution theorem is:

$$\mathcal{F}\{f * g\} = \mathcal{F}\{f\}\mathcal{F}\{g\}, \tag{2.22}$$

where f and g are functions and $*$ represents a convolution:

$$[f * g](t) \equiv \int_0^t f(\tau)g(t - \tau)d\tau. \tag{2.23}$$

If we take the WDA exchange-correlation energy density as an example:

$$\varepsilon_{\text{xc}}^{\text{WDA}}(\boldsymbol{r}) = \frac{1}{2}\int n(\boldsymbol{r}')\frac{G^{\text{WDA}}[\boldsymbol{r}, \boldsymbol{r}'; \tilde{n}(\boldsymbol{r})]}{|\boldsymbol{r} - \boldsymbol{r}'|}d\boldsymbol{r}', \tag{2.24}$$

we see that this is a convolution of the electron density $n(\boldsymbol{r}')$ and the model pair-correlation function over the particle separation. The electron density can be written as a sum of Fourier components:

$$n(\boldsymbol{r}) = \sum_{\boldsymbol{G}} \bar{n}(\boldsymbol{G})e^{i\boldsymbol{G}\cdot\boldsymbol{r}}, \tag{2.25}$$

where $\boldsymbol{G}$ are our reciprocal lattice vectors. The Fourier coefficients $\bar{n}(\boldsymbol{G})$ are easily obtainable using an FFT. All the other functions to be transformed depend on the particle separation $|\boldsymbol{r} - \boldsymbol{r}'|$, so we can use the three dimensional spherical Fourier transform:

$$\mathcal{F}\{s(|\boldsymbol{r}-\boldsymbol{r}'|)\} = S(|\boldsymbol{G}|) = 4\pi \int_0^\infty s(|\boldsymbol{r}-\boldsymbol{r}'|)\frac{\sin(|\boldsymbol{G}||\boldsymbol{r}-\boldsymbol{r}'|)}{|\boldsymbol{G}|}|\boldsymbol{r}-\boldsymbol{r}'|\,d|\boldsymbol{r}-\boldsymbol{r}'|, \tag{2.26}$$

where s is some radial function and S is its Fourier transform.

If we take equation 2.2 and make the substitution $u = |r - r'|/\lambda(\tilde{n}(r))$, our general model pair-correlation function can be written as:

$$G^{\text{WDA}}[u, \tilde{n}(r)] = C(\tilde{n}(r))f(u). \tag{2.27}$$

We can then rewrite our spherical Fourier transform in terms of u, from equation 2.26:

$$
\begin{aligned}
\mathcal{F}\{s(u)\} &= 4\pi\lambda^2(\tilde{n}(r)) \int_0^\infty s(u)\frac{\sin(|G|\lambda(\tilde{n}(r))u)}{|G|}u\, du \\
&= 4\pi\lambda^3(\tilde{n}(r)) \int_0^\infty s(u)\frac{\sin(qu)}{q}u\, du,
\end{aligned}
\tag{2.28}
$$

where we make the substitution $q = \lambda(\tilde{n}(r))|G|$.

Exchange-Correlation Energy Density

Continuing with the exchange-correlation energy density as an example, we use the convolution theorem to rewrite equation 2.24 as:

$$\varepsilon_{\text{xc}}^{\text{WDA}}(r) = \frac{1}{2}\sum_G \tilde{n}(G)e^{iG\cdot r} \times \mathcal{F}\left\{\frac{G^{\text{WDA}}[u, \tilde{n}(r)]}{u\lambda(\tilde{n}(r))}\right\}. \tag{2.29}$$

Using our relation for the spherical Fourier transform in terms of the variable u, equation 2.28, we have:

$$\mathcal{F}\left\{\frac{G^{\text{WDA}}[u, \tilde{n}(r)]}{u\lambda(\tilde{n}(r))}\right\} = 4\pi\lambda^2(\tilde{n}(r)) \int_0^\infty G^{\text{WDA}}[u, \tilde{n}(r)]\frac{\sin(qu)}{q}du. \tag{2.30}$$

The exchange-correlation energy density, in an easily calculable form, becomes:

$$\varepsilon_{\mathrm{xc}}^{\mathrm{WDA}}(\boldsymbol{r}) = 2\pi C(\tilde{n}(\boldsymbol{r}))\lambda^2(\tilde{n}(\boldsymbol{r}))\sum_{\boldsymbol{G}}\bar{n}(\boldsymbol{G})e^{i\boldsymbol{G}\cdot\boldsymbol{r}}F_1(q), \tag{2.31}$$

where $F_1(q)$ is given by:

$$F_1(q) = \frac{1}{q}\int_0^\infty f(u)\sin(qu)\,du. \tag{2.32}$$

and can be calculated and stored for a particular choice of model function $f(u)$.

Exchange-Correlation Hole Sum Rule

The sum rule in equation 2.10 is also in the form of a convolution:

$$\int n(\boldsymbol{r}')G^{\mathrm{WDA}}[\boldsymbol{r},\boldsymbol{r}';\tilde{n}(\boldsymbol{r})]d\boldsymbol{r}' = -1, \tag{2.33}$$

and can be rewritten by using the convolution theorem:

$$-1 = \sum_{\boldsymbol{G}}\bar{n}(\boldsymbol{G})e^{i\boldsymbol{G}\cdot\boldsymbol{r}} \times \mathcal{F}\{G^{\mathrm{WDA}}[u,\tilde{n}(\boldsymbol{r})]\}. \tag{2.34}$$

The spherical Fourier transform of the model pair-correlation function is:

$$\mathcal{F}\{G^{\mathrm{WDA}}[u,\tilde{n}(\boldsymbol{r})]\} = 4\pi\lambda^3(\tilde{n}(\boldsymbol{r}))\int_0^\infty G^{\mathrm{WDA}}[u,\tilde{n}(\boldsymbol{r})]\frac{\sin(qu)}{q}u\,du, \tag{2.35}$$

so the sum rule in a calculable form is given by:

$$-1 = 4\pi C(\tilde{n}(\boldsymbol{r}))\lambda^3(\tilde{n}(\boldsymbol{r}))\sum_{\boldsymbol{G}}\bar{n}(\boldsymbol{G})e^{i\boldsymbol{G}\cdot\boldsymbol{r}}F_2(q). \tag{2.36}$$

As for the exchange-correlation energy density, we have the function $F_2(q)$, which is:

$$F_2(q) = \frac{1}{q} \int_0^\infty f(u) \sin(qu) u \, du, \tag{2.37}$$

and, for a given model function $f(u)$, can be pre-calculated to increase the efficiency of our implementation with only a small increase in memory use.

Scalar Fields C and λ

The scalar fields $C(\tilde{n}(\boldsymbol{r}))$ and $\lambda(\tilde{n}(\boldsymbol{r}))$ are determined to simultaneously satisfy the sum rule of equation 2.10 and to revert to the LDA energy in the uniform limit. For the homogeneous electron gas, the weighted density becomes the electron density and only the constant $|\boldsymbol{G}| = q = 0$ coefficients of the Fourier transforms contribute. Therefore the exchange-correlation energy density and the sum rule of equations 2.31 and 2.36, respectively, become:

$$\varepsilon_{\text{XC}}^{\text{LDA}}(\tilde{n}(\boldsymbol{r})) = \frac{1}{2}\tilde{n}(\boldsymbol{r})C(\tilde{n}(\boldsymbol{r}))\lambda^2(\tilde{n}(\boldsymbol{r}))I_1, \tag{2.38}$$

$$-1 = \tilde{n}(\boldsymbol{r})C(\tilde{n}(\boldsymbol{r}))\lambda^3(\tilde{n}(\boldsymbol{r}))I_2. \tag{2.39}$$

The constants I_1 and I_2 have to be calculated for a particular choice of model function $f(u)$, and are given by:

$$I_1 = 4\pi F_1(0) = 4\pi \int_0^\infty u f(u) \, du, \tag{2.40}$$

$$I_2 = 4\pi F_2(0) = 4\pi \int_0^\infty u^2 f(u) \, du, \tag{2.41}$$

where these relations are obtained by simply taking the $q \to 0$ limit of equations 2.32 and 2.37. See appendix A for details on calculating the values of I_1 and I_2 in general for functions of the four types described later in this chapter. We can solve equations 2.38 and 2.39 simultaneously for $C(\tilde{n}(r))$ and $\lambda(\tilde{n}(r))$ to get:

$$\lambda(\tilde{n}(r)) = \frac{-I_1}{2\varepsilon_{\text{XC}}^{\text{LDA}}(\tilde{n}(r))I_2},$$ (2.42)

$$C(\tilde{n}(r)) = \frac{-1}{\tilde{n}(r)\lambda^3(\tilde{n}(r))I_2}.$$ (2.43)

The LDA exchange-correlation energy density for a given electron density is easily obtained using a standard LDA parameterisation.

Exchange-Correlation Potential

As discussed in section 2.2.1, the exchange-correlation potential in the WDA can be expressed as the sum of three terms, the first of which is simply the exchange-correlation energy density. The second (equation 2.14) and third (equation 2.19 terms are in the form of convolutions, so their Fourier components can be calculated and an FFT can be used to return the result to real space. The Fourier coefficients $\bar{v}_2(G)$ of the second term $v_2(r)$ come from multiplying two Fourier transforms:

$$\bar{v}_2(G) = \frac{1}{2}\mathcal{F}\{n(r')\}\mathcal{F}\left\{\frac{G^{\text{WDA}}[u, \tilde{n}(r')]}{u\lambda(\tilde{n}(r'))}\right\}.$$ (2.44)

If we use equations 2.30 and 2.32 from the exchange-correlation energy density, the coefficients are given by:

$$\bar{v}_2(G) = \frac{2\pi}{\Omega}\int n(r')C(\tilde{n}(r'))\lambda^2(\tilde{n}(r'))e^{-iG\cdot r'}F_1(q)\ dr',$$ (2.45)

where Ω is the volume of the periodic simulation cell. The equivalent equations for

the third potential term also come from use of the convolution theorem, where we can write the Fourier coefficients $\bar{v}_3(G)$ as the multiple of two Fourier transforms:

$$\bar{v}_3(G) = -\frac{1}{2}\mathcal{F}\left\{ n(r')\frac{h_1(r')}{h_2(r')} \right\} \mathcal{F}\left\{ G^{\text{WDA}}[r, r'; \tilde{n}(r')] \right\}. \qquad (2.46)$$

In analogy to the sum rule, we can use equations 2.35 and 2.37 to write:

$$\bar{v}_3(G) = -\frac{2\pi}{\Omega}\int n(r')\frac{h_1(r')}{h_2(r')}C(\tilde{n}(r'))\lambda^3(\tilde{n}(r'))e^{-iG\cdot r'}F_2(q)\ dr'. \qquad (2.47)$$

The added complication in calculating the third potential term comes from the two functions h_1 and h_2 themselves being integrals in the form of convolutions. Here we shall construct each as a function of r rather than r', for simplicity. Both of these functions include the derivative of the model pair-correlation function with respect to the weighted density. As we have our general form specified in terms of the scalar fields C and λ (implicitly through u), we use the chain rule to obtain the derivative:

$$\frac{\partial G^{\text{WDA}}[u, \tilde{n}(r)]}{\partial \tilde{n}(r)} = \frac{\partial G^{\text{WDA}}[u, \tilde{n}(r)]}{\partial C(\tilde{n}(r))}\frac{\partial C(\tilde{n}(r))}{\partial \tilde{n}(r)} + \frac{\partial G^{\text{WDA}}[u, \tilde{n}(r)]}{\partial u}\frac{\partial u}{\partial \tilde{n}(r)}. \qquad (2.48)$$

Because u is a function of λ we shall apply the chain rule to the second term in the above equation, making use of the fact that $u = |r - r'|/\lambda(\tilde{n}(r)) \Rightarrow \partial u/\partial\lambda(\tilde{n}(r)) = -|r - r'|/\lambda^2(\tilde{n}(r)) = -u/\lambda(\tilde{n}(r))$:

$$\frac{\partial G^{\text{WDA}}[u, \tilde{n}(r)]}{\partial \tilde{n}(r)} = \frac{G^{\text{WDA}}[u, \tilde{n}(r)]}{C(\tilde{n}(r))}\frac{\partial C(\tilde{n}(r))}{\partial \tilde{n}(r)} - \frac{u}{\lambda(\tilde{n}(r))}\frac{\partial G^{\text{WDA}}[u, \tilde{n}(r)]}{\partial u}\frac{\partial\lambda(\tilde{n}(r))}{\partial \tilde{n}(r)}. \qquad (2.49)$$

We can then substitute this back into equations 2.20 and 2.21 for h_1 and h_2 to get:

$$h_1(\boldsymbol{r}) = \int \frac{n(\boldsymbol{r'})}{|\boldsymbol{r} - \boldsymbol{r'}|} \frac{G^{\text{WDA}}[u, \tilde{n}(\boldsymbol{r})]}{C(\tilde{n}(\boldsymbol{r}))} \frac{\partial C(\tilde{n}(\boldsymbol{r}))}{\partial \tilde{n}(\boldsymbol{r})} d\boldsymbol{r'} - \int n(\boldsymbol{r'}) \frac{C(\tilde{n}(\boldsymbol{r}))}{\lambda^2(\tilde{n}(\boldsymbol{r}))} \frac{df(u)}{du} \frac{\partial \lambda(\tilde{n}(\boldsymbol{r}))}{\partial \tilde{n}(\boldsymbol{r})} d\boldsymbol{r'},$$

(2.50)

$$h_2(\boldsymbol{r}) = \int n(\boldsymbol{r'}) \frac{G^{\text{WDA}}[u, \tilde{n}(\boldsymbol{r})]}{C(\tilde{n}(\boldsymbol{r}))} \frac{\partial C(\tilde{n}(\boldsymbol{r}))}{\partial \tilde{n}(\boldsymbol{r})} d\boldsymbol{r'} - \int n(\boldsymbol{r'}) \frac{C(\tilde{n}(\boldsymbol{r}))}{\lambda(\tilde{n}(\boldsymbol{r}))} u \frac{df(u)}{du} \frac{\partial \lambda(\tilde{n}(\boldsymbol{r}))}{\partial \tilde{n}(\boldsymbol{r})} d\boldsymbol{r'}.$$

(2.51)

The first term in each of the above equations is proportional to the exchange-correlation energy density in the case of h_1, and the sum rule in the case of h_2. The second terms are convolutions and can be treated in analogous fashion to the sum rule and exchange-correlation energy density. We now have h_1 and h_2 in a calculable form:

$$h_1(\boldsymbol{r}) = \frac{2\varepsilon_{\text{XC}}^{\text{WDA}}(\boldsymbol{r})}{C(\tilde{n}(\boldsymbol{r}))} \frac{\partial C(\tilde{n}(\boldsymbol{r}))}{\partial \tilde{n}(\boldsymbol{r})} - 4\pi C(\tilde{n}(\boldsymbol{r}))\lambda(\tilde{n}(\boldsymbol{r})) \frac{\partial \lambda(\tilde{n}(\boldsymbol{r}))}{\partial \tilde{n}(\boldsymbol{r})} \sum_{\boldsymbol{G}} \tilde{n}(\boldsymbol{G}) e^{i\boldsymbol{G} \cdot \boldsymbol{r}} F_3(q),$$

(2.52)

$$h_2(\boldsymbol{r}) = \frac{-1}{C(\tilde{n}(\boldsymbol{r}))} \frac{\partial C(\tilde{n}(\boldsymbol{r}))}{\partial \tilde{n}(\boldsymbol{r})} - 4\pi C(\tilde{n}(\boldsymbol{r}))\lambda^2(\tilde{n}(\boldsymbol{r})) \frac{\partial \lambda(\tilde{n}(\boldsymbol{r}))}{\partial \tilde{n}(\boldsymbol{r})} \sum_{\boldsymbol{G}} \tilde{n}(\boldsymbol{G}) e^{i\boldsymbol{G} \cdot \boldsymbol{r}} F_4(q),$$

(2.53)

where $F_3(q)$ and $F_4(q)$ are related to the spherical Fourier transform of the derivatives of the model function $df(u)/du$:

$$F_3(q) = \frac{1}{q} \int_0^\infty u \frac{df(u)}{du} \sin(qu) \, du,$$

(2.54)

$$F_4(q) = \frac{1}{q} \int_0^\infty u^2 \frac{df(u)}{du} \sin(qu) \, du.$$

(2.55)

All that remains for our implementation is to calculate the derivatives of the scalar fields C and λ. Using the chain rule on equation 2.42 for λ we have:

$$\frac{\partial \lambda(\tilde{n}(r))}{\partial \tilde{n}(r)} = \frac{I_1}{2\tilde{n}(r)I_2} \left(\frac{v_{\text{XC}}^{\text{LDA}}(\tilde{n}(r)) - \varepsilon_{\text{XC}}^{\text{LDA}}(\tilde{n}(r))}{[\varepsilon_{\text{XC}}^{\text{LDA}}(\tilde{n}(r))]^2} \right),$$ (2.56)

where $v_{\text{XC}}^{\text{LDA}}$ is the LDA exchange-correlation potential. This comes from considering the definition of the exchange-correlation potential and rearranging the following:

$$\frac{\partial E_{\text{XC}}^{\text{LDA}}[\tilde{n}(r)]}{\partial \tilde{n}(r)} = \frac{\partial(\tilde{n}(r)\varepsilon_{\text{XC}}^{\text{LDA}}(\tilde{n}(r)))}{\partial \tilde{n}(r)} = \varepsilon_{\text{XC}}^{\text{LDA}}(\tilde{n}(r)) + \tilde{n}(r)\frac{\partial \varepsilon_{\text{XC}}^{\text{LDA}}(\tilde{n}(r))}{\partial \tilde{n}(r)} = v_{\text{XC}}^{\text{LDA}}(\tilde{n}(r)).$$ (2.57)

The derivative of C comes easily from equation 2.43:

$$\frac{\partial C(\tilde{n}(r))}{\partial \tilde{n}(r)} = \frac{1}{\tilde{n}(r)\lambda^3(\tilde{n}(r))I_2} \left(\frac{1}{\tilde{n}(r)} + \frac{3}{\lambda(\tilde{n}(r))}\frac{\partial \lambda(\tilde{n}(r))}{\partial \tilde{n}(r)} \right).$$ (2.58)

This completes the required components to implement the WDA in a plane wave pseudopotential code.

2.2.3 Algorithm Details

The time consuming step in performing WDA calculations is in determining the weighted density at all points in space. The implementation in CASTEP uses a logarithmic lookup table over the weighted density so that only a limited number of G-vector sums are required. Even so, generating this lookup table is computationally expensive in comparison to the calculations in semi-local approximations. This is balanced by the almost trivial parallelisation of the G-vector sums, which gives us excellent scaling with the number of processors used. The values for the sums

in equations 2.31, 2.36, 2.52 and 2.53 are stored for each weighted density in the logarithmic grid, to be used once an accurate value for the weighted density is determined. A simple search through the values of the sum rule is made and an accurate value for the weighted density is determined through a four point interpolation of the stored data. Armed with the weighted density at all points we can then interpolate our stored data for the exchange-correlation energy density, h_1 and h_2. The integrals for the Fourier coefficients of the second and third potential terms are then performed and the result transformed back to real space using an FFT. With the exchange-correlation energy and potential calculated, the existing CASTEP code for self consistent total energy minimisation can be used.

2.3 Model Pair-Correlation Functions

The method presented in the previous section allows us great flexibility in the choice of a model function. Charlesworth [56] was one of the first to present a systematic study of model pair-correlation functions. Four different classes of model were used that each have a characteristic form of $f(u)$:

(i) Gaussian,

$$f(u) = p(u)e^{-u^2},$$

(2.59)

where $p(u)$ is a polynomial of order N, where N is a multiple of 2, of the form:

$$p(u) = \sum_{n=0,\text{even}}^{N} \frac{u^n}{\frac{n}{2}!}.$$

(2.60)

(ii) Fourth order Gaussian, referred to as such to be consistent with reference [57],

$$f(u) = p(u)e^{-u^4},$$

(2.61)

where $p(u)$ is a polynomial of order $2N$, where $2N$ is a multiple of 4, of the form:

$$p(u) = \sum_{n=0,\text{even}}^{N} \frac{u^{2n}}{\frac{n}{2}!}.$$

(2.62)

(iii) Lorentzian

$$f(u) = \frac{1}{1 + u^n}.$$

(2.63)

(iv) Gunnarsson and Jones

$$f(u) = 1 - e^{-1/u^n},$$

(2.64)

where in each case, n is an integer. In Charlesworth's study, later repeated by Rushton [57], a total of twelve models were tested, three from each class. For the two Gaussian related forms, values of $N/2 = 0, 1$ and 2 were taken. The remaining two forms took values of $n = 4, 5$ and 6. It should be noted that both Charlesworth and Rushton used a form for the $n = 2$ fourth order Gaussian that was inconsistent with the general form. They used $f(u) = (1+u^4+u^8)e^{-u^4}$ when, if the trend was followed, one should use $f(u) = (1 + u^4 + \frac{1}{2}u^8)e^{-u^4}$. We show the difference graphically in Figure 2.1, illustrating the undesirable turning point in the Charlesworth form. For a comparison of the twelve functional forms in the homogeneous electron gas, see Figure 1 of reference [57].
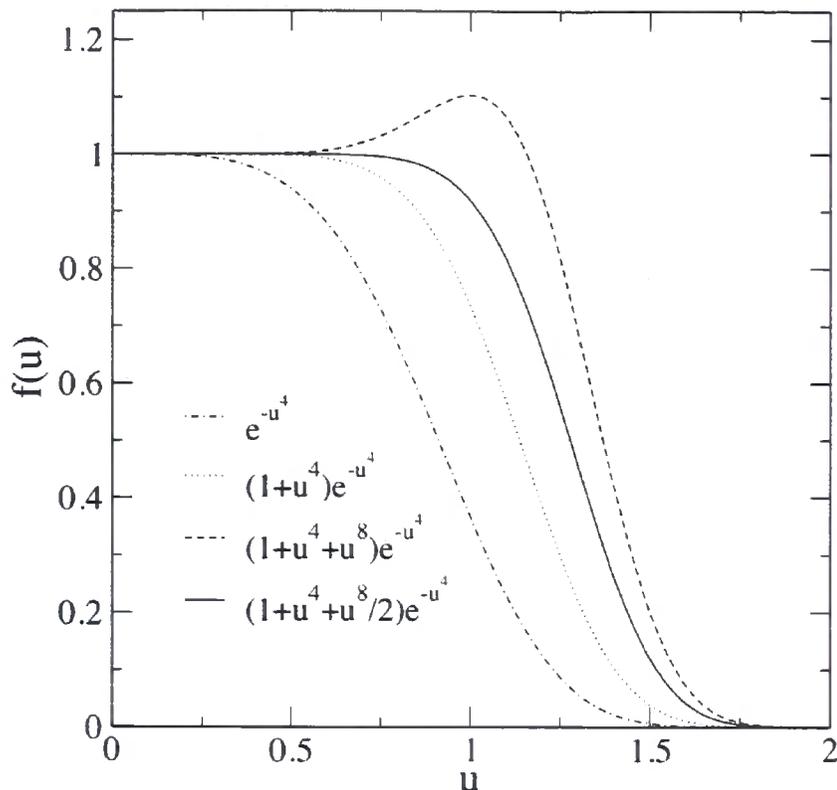
Figure 2.1: Model functions $f(u)$ of the fourth order Gaussian type. The model used by Charesworth for $n = 2$ (dashed line) clearly stands out from the desired trend.

2.3.1 Comparison of Models – Bulk Copper

The previous study [57] of only three functions from each class showed relatively little difference in the lattice parameter of silicon within one class, particularly with the Gaussian based functions. In the next chapter we will be presenting simulations involving copper surfaces. As a preliminary to these surface calculations, we repeat and extend the investigation of model functionals to bulk copper. In Table 2.1, we present the equilibrium lattice parameter, a_0, of the face centered cubic cell, and bulk modulus, B_0, of Cu for a considerably larger range of model functionals than has been previously attempted. For comparison, we also provide results using the LDA and the PBE GGA. We use a cell that is the primitive of the face centred cubic structure (as shown in Figure 2.2) with the first lattice vector doubled.

This is so that we have two Cu atoms per cell and can treat the whole system as spin unpolarised. In all of these calculations we used LDA ultrasoft pseudopotentials. Ideally, pseudopotentials constructed consistently with each approximation for exchange-correlation would be used. In practice we do not have a method for generating WDA pseudopotentials available. This is discussed further in Chapter 7. By using a single pseudopotential, it could be considered that we are comparing the performance of each model for exchange-correlation for the same external potential. A plane wave cutoff energy of 400 eV and a sampling of the Brillouin zone using a Monkhorst-Pack grid of $3 \times 6 \times 6$ k-points. This converges total energy differences to better than 10 meV per atom.
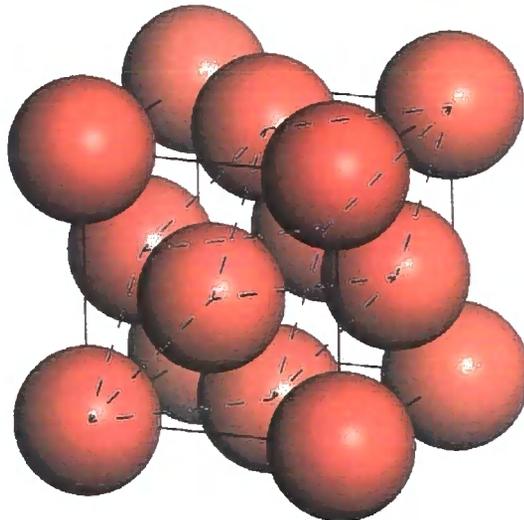
Figure 2.2: The face centred cubic structure of copper (solid lines) with the primitive cell overlaid (dashed lines).

To obtain the physical properties in Table 2.1, we performed total energy calculations at a number of lattice parameter values. We then fitted the resulting energy-volume curves for each functional form to the Murnaghan equation of state [58] and hence obtain the equilibrium lattice constant and the bulk modulus. The Gaussian based model pair-correlation functions go from overestimating the lattice parameter and underestimating the bulk modulus to the opposite, when moving from the simple Gaussian to a Gaussian in combination with an eighth order polynomial. The crossing point for giving experimental values is between the Guassian

Table 2.1: Equilibrium lattice parameters and bulk moduli for Cu using a range of model pair-correlation functions. Percentage error from experiment in parentheses.

Pair Correlation Function	a_0 (Å)	B_0 (GPa)
e^{-u^2}	3.709 (2.61)	112 (-20.0)
$(1 + u^2)e^{-u^2}$	3.649 (0.93)	129 (-7.86)
$(1 + u^2 + \frac{1}{2}u^4)e^{-u^2}$	3.623 (0.22)	138 (-1.43)
$(1 + u^2 + \frac{1}{2}u^4 + \frac{1}{3!}u^6)e^{-u^2}$	3.609 (-0.15)	143 (2.14)
$(1 + u^2 + \frac{1}{2}u^4 + \frac{1}{3!}u^6 + \frac{1}{4!}u^8)e^{-u^2}$	3.601 (-0.38)	147 (5.00)
e^{-u^4}	3.603 (-0.33)	146 (4.29)
$(1 + u^4)e^{-u^4}$	3.587 (-0.78)	153 (9.29)
$(1 + u^4 + \frac{1}{2}u^8)e^{-u^4}$	3.581 (-0.93)	155 (10.7)
$(1 + u^4 + u^8)e^{-u^4}$	3.576 (-1.07)	158 (12.9)
$(1 + u^4 + \frac{1}{2}u^8 + \frac{1}{3!}u^{12})e^{-u^4}$	3.579 (-1.00)	157 (12.1)
$1/(1 + u^4)$	unbound	
$1/(1 + u^5)$	4.188 (15.86)	28.7 (-79.5)
$1/(1 + u^6)$	3.798 (5.06)	85.2 (-39.1)
$1/(1 + u^7)$	3.692 (2.13)	114 (-18.6)
$1/(1 + u^8)$	3.647 (0.88)	129 (-7.86)
$1/(1 + u^9)$	3.622 (0.20)	138 (-1.43)
$1/(1 + u^{10})$	3.608 (-0.20)	144 (2.86)
$1/(1 + u^{11})$	3.598 (-0.46)	147 (5.00)
$1 - e^{-1/u^4}$	unbound	
$1 - e^{-1/u^5}$	4.069 (12.55)	38.8 (-72.3)
$1 - e^{-1/u^6}$	3.755 (3.88)	94.5 (-32.5)
$1 - e^{-1/u^7}$	3.669 (1.49)	121 (-13.6)
$1 - e^{-1/u^8}$	3.630 (0.41)	135 (-3.57)
$1 - e^{-1/u^9}$	3.610 (-0.13)	142 (1.43)
$1 - e^{-1/u^{10}}$	3.599 (-0.45)	147 (5.00)
LDA	3.513 (-2.81)	185 (32.1)
PBE	3.598 (-0.47)	146 (4.29)
Expt.	3.615	140

combined with a fourth order and sixth order polynomial, where the sixth order gives a slightly better lattice parameter and the fourth order giving a slightly better bulk modulus.

Model pair-correlation functions based on fourth order Gaussians start by underestimating the lattice parameter and overestimating the bulk modulus. These misestimates only become worse as higher order polynomials are included. We include both the Charlesworth version and our corrected version using an eighth order polynomial. The lattice parameters in this case only differ by 0.005 Å and the bulk modulus by only 3 GPa, suggesting that the turning point in the Charlesworth model has little effect on determining physical quantities.

The first of the original three Lorentzian based functions (containing an exponent of 4) predicts that the lowest energy is for isolated atoms. The remainder of the functions initially under-bind, eventually over binding when an exponent of 10 or higher is used. A similar trend is present for the Gunnarsson-Jones-like functions, predicting over binding only when an exponent of 9 or more is used. Again, the first of the original three models of this class, containing an exponent of 4, predicts that the system is not bound. It is encouraging to note that for all four classes of model function, the closest lattice parameters simultaneously predict the closest bulk moduli to experiment.

This study of functional trends shows that with the ability to tune the model *ad infinitum*, that one can find at least one model that matches experiment. However, this does not mean that any one model pair-correlation function transfers well between systems. There is also no way to select a model function of this type that compares well with experiment for a system *a priori*. Therefore we turn to improving our model pair-correlation functions by enforcing known physical constraints on the pair-correlation function. A possible approach is given in the next section.

2.4   Kimball Cusp Condition

In his PhD thesis, Rushton [59] suggested a new form of model functional that incorporates a constraint on the pair-correlation function called the Kimball cusp

condition [19]. This arises from correlation effects involving antiparallel spin pairs and relates the value $g_{\mathrm{xc}}(\boldsymbol{r}, \boldsymbol{r}')$ to its derivative with respect to pair separation, $r = |\boldsymbol{r} - \boldsymbol{r}'|$, in the limit of zero separation:

$$\frac{\partial g_{\mathrm{xc}}(\boldsymbol{r}, \boldsymbol{r}')}{\partial r}\bigg|_{r \to r'} = g_{\mathrm{xc}}(\boldsymbol{r}, \boldsymbol{r}')|_{r \to r'}. \tag{2.65}$$

For our model $G^{\mathrm{WDA}}[r, \tilde{n}(\boldsymbol{r})] = g_{\mathrm{xc}}^{\mathrm{WDA}}(\boldsymbol{r}, \boldsymbol{r}') - 1$, we have $G^{\mathrm{WDA}}[0, \tilde{n}(\boldsymbol{r})] = C(\tilde{n}(\boldsymbol{r}))$ and therefore require that $\partial G^{\mathrm{WDA}}[r, \tilde{n}(\boldsymbol{r})]/\partial r = C(\tilde{n}(\boldsymbol{r})) + 1$ as $r \to 0$. One way of doing this is to build on the existing models by adding a second term:

$$G^{\mathrm{CWDA}}[\boldsymbol{r}, \boldsymbol{r}'; \tilde{n}(\boldsymbol{r})] = G^{a}[\boldsymbol{r}, \boldsymbol{r}'; \tilde{n}(\boldsymbol{r})] + G^{b}[\boldsymbol{r}, \boldsymbol{r}'; \tilde{n}(\boldsymbol{r})], \tag{2.66}$$

where $G^{a}[\boldsymbol{r}, \boldsymbol{r}'; \tilde{n}(\boldsymbol{r})]$ is one of our previous functional forms and $G^{b}[\boldsymbol{r}, \boldsymbol{r}'; \tilde{n}(\boldsymbol{r})]$ is used to alter the short range behaviour of the old model function. We use CWDA to label our cusp condition satisfying model. If we have the first term as one of our old model functions:

$$G^{a}[\boldsymbol{r}, \boldsymbol{r}'; \tilde{n}(\boldsymbol{r})] = C(\tilde{n}(\boldsymbol{r}))f\left(\frac{|\boldsymbol{r} - \boldsymbol{r}'|}{\lambda(\tilde{n}(\boldsymbol{r}))}\right) = C(\tilde{n}(\boldsymbol{r}))f(u), \tag{2.67}$$

then we can choose the second term to be of the form:

$$\begin{aligned} G^{b}[\boldsymbol{r}, \boldsymbol{r}'; \tilde{n}(\boldsymbol{r})] &= (C(\tilde{n}(\boldsymbol{r})) + 1)|\boldsymbol{r} - \boldsymbol{r}'|f\left(\frac{|\boldsymbol{r} - \boldsymbol{r}'|}{\kappa\lambda(\tilde{n}(\boldsymbol{r}))}\right) \\ &= (C(\tilde{n}(\boldsymbol{r})) + 1)\lambda(\tilde{n}(\boldsymbol{r}))uf\left(\frac{u}{\kappa}\right), \end{aligned} \tag{2.68}$$

where κ controls the range of the alteration to the old model. This approach will work providing the derivative of the function $f(u)$ with respect to u as $u \to 0$

is itself zero. The value of κ can be chosen such that the physical constraint of $0 \leq g_{\mathrm{xc}}(\boldsymbol{r}, \boldsymbol{r}) \leq 0.5$ is satisfied in the uniform limit, or at least satisfied as closely as possible.

2.4.1 Reciprocal Space Implementation

We can construct an efficient implementation of this new type of model pair-correlation function by following section 2.2.2. For ease, we will write our model pair-correlation function as:

$$G^{\mathrm{CWDA}}[u, \tilde{n}(\boldsymbol{r})] = C(\tilde{n}(\boldsymbol{r}))f^a(u) + (C(\tilde{n}(\boldsymbol{r})) + 1)\lambda(\tilde{n}(\boldsymbol{r}))f^b(u), \qquad (2.69)$$

where $f^a(u)$ is one of our original model $f(u)$ functions and $f^b(u) = uf^a(u/\kappa)$.

Exchange-Correlation Energy Density and Sum Rule

We follow from equation 2.24, rewriting it in reciprocal space using the convolution theorem to obtain an analogue of equation 2.31:

$$\varepsilon_{\mathrm{xc}}^{\mathrm{CWDA}}(\boldsymbol{r}) = 2\pi C(\tilde{n}(\boldsymbol{r}))\lambda^2(\tilde{n}(\boldsymbol{r})) \sum_{\boldsymbol{G}} \bar{n}(\boldsymbol{G})e^{i\boldsymbol{G}\cdot\boldsymbol{r}}H_1(q). \qquad (2.70)$$

Where the function $H_1(q)$ replaces $F_1(q)$ in equation 2.31 and is given by:

$$H_1(q) = F_1^a(q) + \left(1 + \frac{1}{C(\tilde{n}(\boldsymbol{r}))}\right)\lambda(\tilde{n}(\boldsymbol{r}))F_1^b(q), \qquad (2.71)$$

where $F_1^a(q)$ and $F^b(q)$ are related to the spherical Fourier transform of each part of the model pair-correlation function:

$$F_1^a(q) = \frac{1}{q}\int_0^\infty f^a(u)\sin(qu)\,du, \qquad (2.72)$$

$$F_1^b(q) = \frac{1}{q} \int_0^\infty f^b(u) \sin(qu) \, du. \tag{2.73}$$

Similarly, we can write the sum rule in reciprocal space using the convolution theorem with equation 2.10 and replacing $F_2(q)$ with $H_2(q)$ in equation 2.36:

$$-1 = 4\pi C(\tilde{n}(\boldsymbol{r}))\lambda^3(\tilde{n}(\boldsymbol{r})) \sum_{\boldsymbol{G}} \bar{n}(\boldsymbol{G}) e^{i\boldsymbol{G}\cdot\boldsymbol{r}} H_2(q), \tag{2.74}$$

where $H_2(q)$ is given by:

$$H_2(q) = F_2^a(q) + \left(1 + \frac{1}{C(\tilde{n}(\boldsymbol{r}))}\right) \lambda(\tilde{n}(\boldsymbol{r})) F_2^b(q), \tag{2.75}$$

and $F_2^a(q)$ and $F_2^b(q)$ are given by:

$$F_2^a(q) = \frac{1}{q} \int_0^\infty f^a(u) \sin(qu) u \, du, \tag{2.76}$$

$$F_2^b(q) = \frac{1}{q} \int_0^\infty f^b(u) \sin(qu) u \, du. \tag{2.77}$$

and are related to spherical Fourier transforms of the model functions.

Scalar Fields C and λ

The extra term in the model pair-correlation function makes calculating the scalar fields C and λ slightly more complicated. Our equations 2.70 and 2.74 for the exchange-correlation energy and the sum rule can be written in the homogeneous limit as:

$$\varepsilon_{\text{xc}}^{\text{LDA}}(\tilde{n}(r)) = \frac{\tilde{n}(r)}{2}C(\tilde{n}(r))\lambda^2(\tilde{n}(r))\left(I_1^a + \left(1 + \frac{1}{C(\tilde{n}(r))}\right)\lambda(\tilde{n}(r))I_1^b\right),$$

$$(2.78)$$

$$-1 = \tilde{n}(r)C(\tilde{n}(r))\lambda^3(\tilde{n}(r))\left(I_2^a + \left(1 + \frac{1}{C(\tilde{n}(r))}\right)\lambda(\tilde{n}(r))I_2^b\right),$$

$$(2.79)$$

where I_1^a, I_1^b, I_2^a and I_2^b are constants depending on the model chosen:

$$I_1^a = 4\pi F_1^a(0) = 4\pi\int_0^\infty uf^a(u)\,du, \quad I_1^b = 4\pi F_1^b(0) = 4\pi\int_0^\infty uf^b(u)\,du,$$

$$(2.80)$$

$$I_2^a = 4\pi F_2^a(0) = 4\pi\int_0^\infty u^2 f^a(u)\,du, \quad I_2^b = 4\pi F_2^b(0) = 4\pi\int_0^\infty u^2 f^b(u)\,du.$$

$$(2.81)$$

See appendix A for details on calculating these values in general. We must then solve equations 2.78 and 2.79 simultaneously to obtain values for C and λ at each point. Equation 2.79 can be rearranged to get C in terms of λ:

$$C(\tilde{n}(r)) = -\frac{1 + \tilde{n}(r)\lambda^4(\tilde{n}(r))I_2^b}{\tilde{n}(r)\lambda^3(\tilde{n}(r))(I_2^a + \lambda(\tilde{n}(r))I_2^b)},$$

$$(2.82)$$

which we then substitute back into equation 2.78 to obtain a quartic polynomial in λ:

$$a_4\lambda^4(\tilde{n}(r)) + a_2\lambda^2(\tilde{n}(r)) + a_1\lambda(\tilde{n}(r)) + a_0 = 0,$$

$$(2.83)$$

where the coefficients are given by:

$$a_4 = \tilde{n}(\boldsymbol{r})(I_1^a I_2^b - I_1^b I_2^a), \tag{2.84}$$

$$a_2 = 2\varepsilon_{\text{XC}}^{\text{LDA}}(\tilde{n}(\boldsymbol{r}))I_2^b, \tag{2.85}$$

$$a_1 = 2\varepsilon_{\text{XC}}^{\text{LDA}}(\tilde{n}(\boldsymbol{r}))I_2^a + I_1^b, \tag{2.86}$$

$$a_0 = I_1^a. \tag{2.87}$$

There are many methods available to obtain the roots of equation 2.83. We choose to construct a companion matrix:

$$\begin{pmatrix} 0 & 0 & 0 & -a_0/a_4 \\ 1 & 0 & 0 & -a_1/a_4 \\ 0 & 1 & 0 & -a_2/a_4 \\ 0 & 0 & 1 & 0 \end{pmatrix}, \tag{2.88}$$

the eigenvalues of which give us the possible values for λ. A standard linear algebra library such as LAPACK can be used to calculate these values efficiently. The roots of λ are values that, for a fixed value of κ, that satisfy the mathematical constraints of the model. Physically, λ controls the range of the model pair-correlation function, so a real, positive root must be chosen. This is also in order to keep C negative and therefore physical. A positive value of C would give an on-top value for the model pair-correlation function greater than 1, which is, of course, impossible for a probability. On the occasions that there are multiple real positive values for λ, we select the smallest one by elimination of values that give an unphysically large range for the model pair-correlation function.

Exchange-Correlation Potential

As before, the exchange-correlation potential can be written as a sum of three terms. The first of them is simply the exchange-correlation energy density, $v_1(\boldsymbol{r}) = \varepsilon_{\text{xc}}^{\text{CWDA}}(\boldsymbol{r})$. The second term is obtained in the same way as the original WDA (equation 2.45) and the Fourier coefficients can be written as:

$$\bar{v}_2(\boldsymbol{G}) = \frac{2\pi}{\Omega} \int n(\boldsymbol{r}')C(\tilde{n}(\boldsymbol{r}'))\lambda^2(\tilde{n}(\boldsymbol{r}'))e^{-i\boldsymbol{G}\cdot\boldsymbol{r}'}H_1(q), \tag{2.89}$$

where we gave $H_1(q)$ in equation 2.71. The third term can be obtained in analogy with equation 2.47, where $H_2(q)$ was given in equation 2.75:

$$\bar{v}_3(\boldsymbol{G}) = -\frac{2\pi}{\Omega} \int n(\boldsymbol{r}')\frac{h_1(\boldsymbol{r}')}{h_2(\boldsymbol{r}')}C(\tilde{n}(\boldsymbol{r}'))\lambda^3(\tilde{n}(\boldsymbol{r}'))e^{-i\boldsymbol{G}\cdot\boldsymbol{r}'}H_2(q)d\boldsymbol{r}'. \tag{2.90}$$

The functions h_1 and h_2 are more complicated in this case through our explicit λ dependance in the model pair-correlation function, as given in equation 2.69. The derivative of the model pair-correlation function with respect to the weighted density therefore requires an extra term compared to equation 2.48:

$$\frac{\partial G^{\text{CWDA}}[u,\tilde{n}(\boldsymbol{r})]}{\partial \tilde{n}(\boldsymbol{r})} = \frac{\partial G^{\text{CWDA}}[u,\tilde{n}(\boldsymbol{r})]}{\partial C(\tilde{n}(\boldsymbol{r}))}\frac{\partial C(\tilde{n}(\boldsymbol{r}))}{\partial \tilde{n}(\boldsymbol{r})} + \frac{\partial G^{\text{CWDA}}[u,\tilde{n}(\boldsymbol{r})]}{\partial \lambda(\tilde{n}(\boldsymbol{r}))}\frac{\partial \lambda(\tilde{n}(\boldsymbol{r}))}{\partial \tilde{n}(\boldsymbol{r})}$$

$$- \frac{u}{\lambda(\tilde{n}(\boldsymbol{r}))}\frac{\partial G^{\text{WDA}}[u,\tilde{n}(\boldsymbol{r})]}{\partial u}\frac{\partial \lambda(\tilde{n}(\boldsymbol{r}))}{\partial \tilde{n}(\boldsymbol{r})}. \tag{2.91}$$

We then put this back into equation 2.20 for h_1 and recast the integrals in reciprocal space:

$$h_1(\boldsymbol{r}) = 4\pi\lambda(\tilde{n}(\boldsymbol{r})) \sum_{\boldsymbol{G}} \bar{n}(\boldsymbol{G})e^{i\boldsymbol{G}\cdot\boldsymbol{r}}\left[\lambda(\tilde{n}(\boldsymbol{r}))\frac{\partial C(\tilde{n}(\boldsymbol{r}))}{\partial \tilde{n}(\boldsymbol{r})}\left(F_1^a(q) + \lambda(\tilde{n}(\boldsymbol{r}))F_1^b(q)\right)\right.$$

$$+ \left.(C(\tilde{n}(\boldsymbol{r})) + 1)\lambda(\tilde{n}(\boldsymbol{r}))\frac{\partial \lambda(\tilde{n}(\boldsymbol{r}))}{\tilde{n}(\boldsymbol{r})}F_1^b(q) - C(\tilde{n}(\boldsymbol{r}))\frac{\partial \lambda(\tilde{n}(\boldsymbol{r}))}{\partial \tilde{n}(\boldsymbol{r})}H_3(q)\right], \tag{2.92}$$

where we defined $F_1^a(q)$ and $F_1^b(q)$ previously in equations 2.72 and 2.73, respectively. The function $H_3(q)$ is given by:

$$H_3(q) = F_3^a(q) + \left(1 + \frac{1}{C(\tilde{n}(r))}\right) \lambda(\tilde{n}(r)) F_3^b(q), \tag{2.93}$$

where $F_3^a(q)$ and $F_3^b(q)$ are related to spherical Fourier transforms of the derivatives of $f^a(u)$ and $f^b(u)$:

$$F_3^a(q) = \frac{1}{q} \int_0^\infty u \frac{df^a(u)}{du} \sin(qu) \, du, \tag{2.94}$$

$$F_3^b(q) = \frac{1}{q} \int_0^\infty u \frac{df^b(u)}{du} \sin(qu) \, du. \tag{2.95}$$

To keep the implementation efficient, we can rewrite equation 2.92 as:

$$h_1(r) = \frac{2\varepsilon_{\mathrm{XC}}^{\mathrm{CWDA}}(r)}{C(\tilde{n}(r))} \frac{\partial C(\tilde{n}(r))}{\partial \tilde{n}(r)} + 4\pi \sum_G \bar{n}(G) e^{iG \cdot r}$$

$$\times \left[(C(\tilde{n}(r)) + 1) \lambda^2(\tilde{n}(r)) \frac{\partial \lambda(\tilde{n}(r))}{\partial \tilde{n}(r)} F_1^b(q) - \right.$$

$$\left. \frac{\lambda^3(\tilde{n}(r))}{C(\tilde{n}(r))} \frac{\partial C(\tilde{n}(r))}{\partial \tilde{n}(r)} F_1^b(q) - C(\tilde{n}(r)) \lambda(\tilde{n}(r)) \frac{\partial \lambda(\tilde{n}(r))}{\partial \tilde{n}(r)} H_3(q) \right]. \tag{2.96}$$

This means we do not have to store $F_1^a(q)$ or interpolate for its value separately. We treat h_2 similarly, substituting equation 2.91 back into equation 2.21 and writing the integrals in reciprocal space:

$$h_2(r) = 4\pi \lambda^2(\tilde{n}(r)) \sum_G \bar{n}(G) e^{iG \cdot r} \left[\lambda(\tilde{n}(r)) \frac{\partial C(\tilde{n}(r))}{\partial \tilde{n}(r)} \left(F_2^a(q) + \lambda(\tilde{n}(r)) F_2^b(q) \right) \right.$$

$$\left. + (C(\tilde{n}(r)) + 1) \lambda(\tilde{n}(r)) \frac{\partial \lambda(\tilde{n}(r))}{\tilde{n}(r)} F_2^b(q) - C(\tilde{n}(r)) \frac{\partial \lambda(\tilde{n}(r))}{\partial \tilde{n}(r)} H_4(q) \right]. \tag{2.97}$$

We gave $F_2^a(q)$ and $F_2^b(q)$ previously in equations 2.76 and 2.77, and $H_4(q)$ is given by:

$$H_4(q) = F_4^a(q) + \left(1 + \frac{1}{C(\tilde{n}(\boldsymbol{r}))}\right) \lambda(\tilde{n}(\boldsymbol{r})) F_4^b(q). \tag{2.98}$$

The spherical Fourier transforms of the derivatives of the model functions are given by $F_4^a(q)$ and $F_4^b(q)$:

$$F_4^a(q) = \frac{1}{q} \int_0^\infty u^2 \frac{df^a(u)}{du} \sin(qu) \, du, \tag{2.99}$$

$$F_4^b(q) = \frac{1}{q} \int_0^\infty u^2 \frac{df^b(u)}{du} \sin(qu) \, du. \tag{2.100}$$

As with h_1 we rewrite h_2 in equation 2.97 to reduce the storage requirements in our implementation:

$$
\begin{aligned}
h_2(\boldsymbol{r}) \;=\; & \frac{-1}{C(\tilde{n}(\boldsymbol{r}))} \frac{\partial C(\tilde{n}(\boldsymbol{r}))}{\partial \tilde{n}(\boldsymbol{r})} + 4\pi \sum_{\boldsymbol{G}} \tilde{n}(\boldsymbol{G}) e^{i\boldsymbol{G}\cdot\boldsymbol{r}} \\[2mm]
& \times \left[(C(\tilde{n}(\boldsymbol{r})) + 1)\lambda^3(\tilde{n}(\boldsymbol{r})) \frac{\partial \lambda(\tilde{n}(\boldsymbol{r}))}{\partial \tilde{n}(\boldsymbol{r})} F_2^b(q) - \right. \\[2mm]
& \left. \frac{\lambda^4(\tilde{n}(\boldsymbol{r}))}{C(\tilde{n}(\boldsymbol{r}))} \frac{\partial C(\tilde{n}(\boldsymbol{r}))}{\partial \tilde{n}(\boldsymbol{r})} F_2^b(q) - C(\tilde{n}(\boldsymbol{r}))\lambda^2(\tilde{n}(\boldsymbol{r})) \frac{\partial \lambda(\tilde{n}(\boldsymbol{r}))}{\partial \tilde{n}(\boldsymbol{r})} H_4(q) \right].
\end{aligned}
\tag{2.101}
$$

The derivatives of the scalar fields can be obtained from equations 2.82 and 2.83. Implicit differentiation of equation 2.83 gives us:

$$\frac{\partial \lambda(\tilde{n}(\boldsymbol{r}))}{\partial \tilde{n}(\boldsymbol{r})} = -\frac{(a_4/\tilde{n}(\boldsymbol{r}))\lambda^4(\tilde{n}(\boldsymbol{r})) + 2\lambda(\tilde{n}(\boldsymbol{r}))(I_2^a + \lambda(\tilde{n}(\boldsymbol{r}))I_2^b)(\partial \varepsilon_{xc}^{LDA}(\tilde{n}(\boldsymbol{r}))/\partial \tilde{n}(\boldsymbol{r}))}{4a_4\lambda^3(\tilde{n}(\boldsymbol{r})) + 2a_2\lambda(\tilde{n}(\boldsymbol{r})) + a_1},$$

$$(2.102)$$

where the derivative of the LDA exchange-correlation energy density is:

$$\frac{\partial \varepsilon_{\text{XC}}^{\text{LDA}}(\tilde{n}(\boldsymbol{r}))}{\partial \tilde{n}(\boldsymbol{r})} = \frac{v_{\text{XC}}^{\text{LDA}}(\tilde{n}(\boldsymbol{r})) - \varepsilon_{\text{XC}}^{\text{LDA}}(\tilde{n}(\boldsymbol{r}))}{\tilde{n}(\boldsymbol{r})}, \qquad (2.103)$$

as can be shown from equation 2.57. The derivative of C comes from equation 2.82 and using the sum rule:

$$\frac{\partial C(\tilde{n}(\boldsymbol{r}))}{\partial \tilde{n}(\boldsymbol{r})} = \frac{1}{\tilde{n}^2(\boldsymbol{r})\lambda^3(\tilde{n}(\boldsymbol{r}))(I_2^a + \lambda(\tilde{n}(\boldsymbol{r}))I_2^b)} + \frac{\partial C(\tilde{n}(\boldsymbol{r}))}{\partial \lambda(\tilde{n}(\boldsymbol{r}))}\frac{\partial \lambda(\tilde{n}(\boldsymbol{r}))}{\partial \tilde{n}(\boldsymbol{r})}, \qquad (2.104)$$

where the derivative of C with respect to λ is:

$$\frac{\partial C(\tilde{n}(\boldsymbol{r}))}{\partial \lambda(\tilde{n}(\boldsymbol{r}))} = \frac{3I_2^a + 4\lambda(\tilde{n}(\boldsymbol{r}))I_2^b - I_2^a I_2^b \tilde{n}(\boldsymbol{r})\lambda^4(\tilde{n}(\boldsymbol{r}))}{\tilde{n}(\boldsymbol{r})\lambda^4(\tilde{n}(\boldsymbol{r}))(I_2^a + \lambda(\tilde{n}(\boldsymbol{r}))I_2^b)^2}. \qquad (2.105)$$

To be used in self-consistent calculations on realistic systems we must test the exchange-correlation energy and potential in our implementation for consistency. We can do this by comparing the numerical forces on atoms with analytic forces obtained through the Hellmann-Feynman theorem [60]. Our test calculation placed a hydrogen (H_2) molecule in a cell of dimensions $4 \times 2 \times 2$ Å^3 with a bond length of 0.7 Å oriented along the long axis of the cell. A small shift in the bond length of 0.001 Å in both directions gave us numerical forces that match analytic values to fractions of a percent. This is comparable to the same test applied on the original WDA implementation. We now discuss the selection of the κ parameter and later apply the cusp modified WDA to obtain bulk properties of silicon.

2.4.2 Testing and Determining κ

To use our new model function incorporating the Kimball cusp condition we must determine a value for κ for each specific function $f(u)$ chosen. To do this, we will apply our model pair-correlation function in the homogeneous limit and select κ to constrain the on-top value as close to physical limits as possible. Here we will use a simple Gaussian and fourth order Gaussian $f^a(u) = e^{-u^2}$ and e^{-u^4} and therefore have corresponding $f^b(u) = ue^{-u^2/\kappa^2}$ and ue^{-u^4/κ^4}, respectively. In Table 2.2 we show the on-top values of the model pair correlation function for the model functions of Gaussian and fourth order Gaussian type along with their Kimball cusp condition corrected counterparts. For the Gaussian based model, the best value for our parameter is $\kappa = 0.88$ and for the fourth order Gaussian based model the value is $\kappa = 0.95$. Both values were chosen in an attempt to keep the on-top value of the model function within the range $0 \leq g_{\mathrm{xc}}^{\mathrm{CWDA}}(r, r) \leq 0.5$. The above values of κ provide the best on-top values at both the high and low density limits simultaneously. Other values of κ could be chosen that improve the low or high density limits individually, but this would be to the detriment of the respective opposite limits. Table 2.2 shows that in both cases, the modified models improve the on-top values over the originals.

In Figure 2.3 we show the model pair-correlation functions for the simple Gaussian based model and the cusp corrected counterpart in the homogeneous electron gas at a number of densities. As can be seen, the modifications have an effect only on the short range, leaving the long range untouched. At low ($r_s \gtrsim 8$, where $r_s = (3/4\pi n)^{1/3}$) densities, the on-top value goes negative and therefore unphysical. Because we enforce the cusp condition the gradient at zero separation must also be negative, producing a turning point that is also non-physical.

For the fourth order Gaussian based model, the on-top value does not go negative in this density range. In Figure 2.4 we show a graphical comparison of the old model with the Kimball cusp condition satisfying model. Here, the long range part of the function is more greatly affected. This is because the value of $\kappa = 0.95$ is sufficiently close to unity to have an effect beyond the short range part of the pair-correlation function.
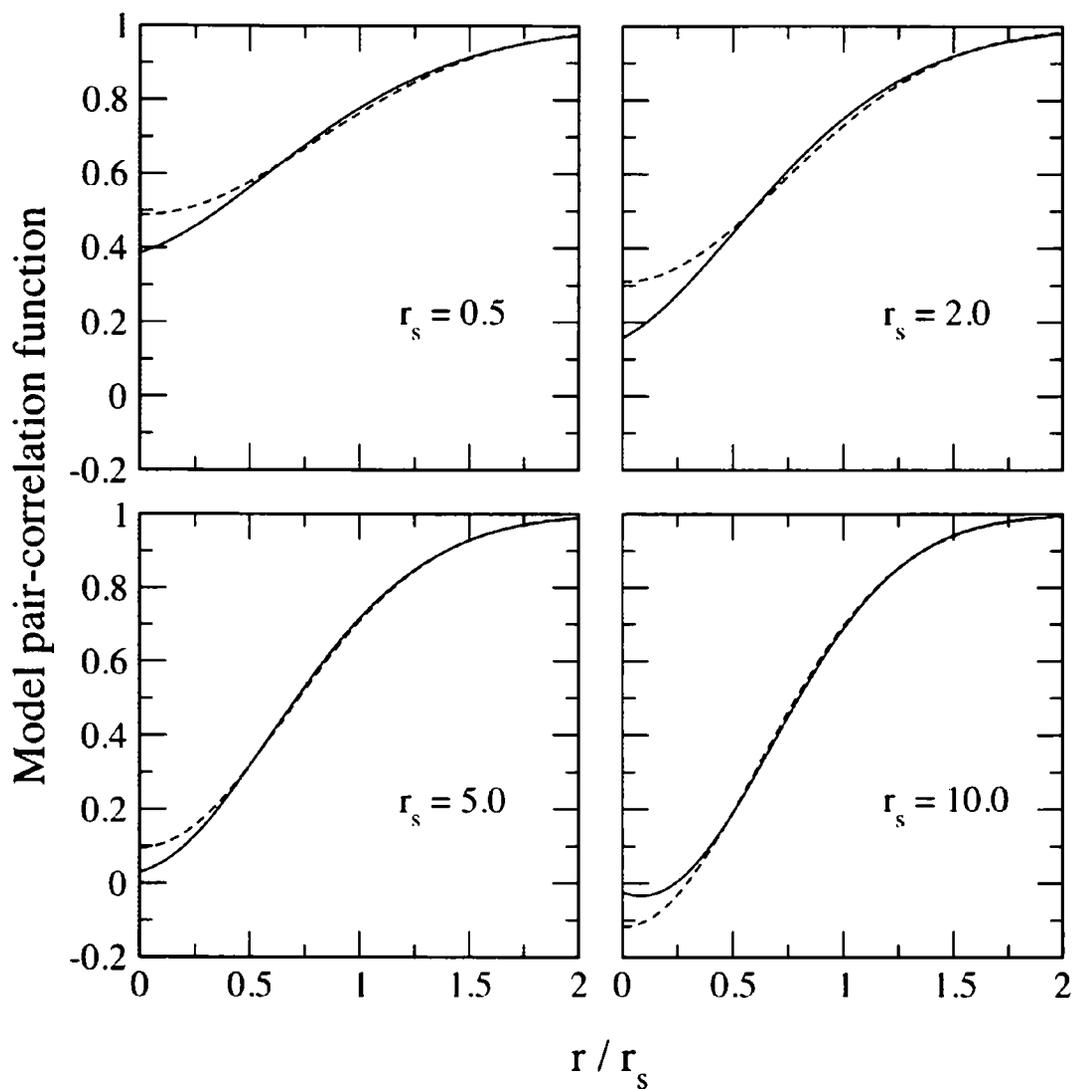
Figure 2.3: Model pair-correlation functions in the homogeneous electron gas at a number of densities for the Gaussian based model both with (solid line) and without (dashed line) the cusp condition enforced.
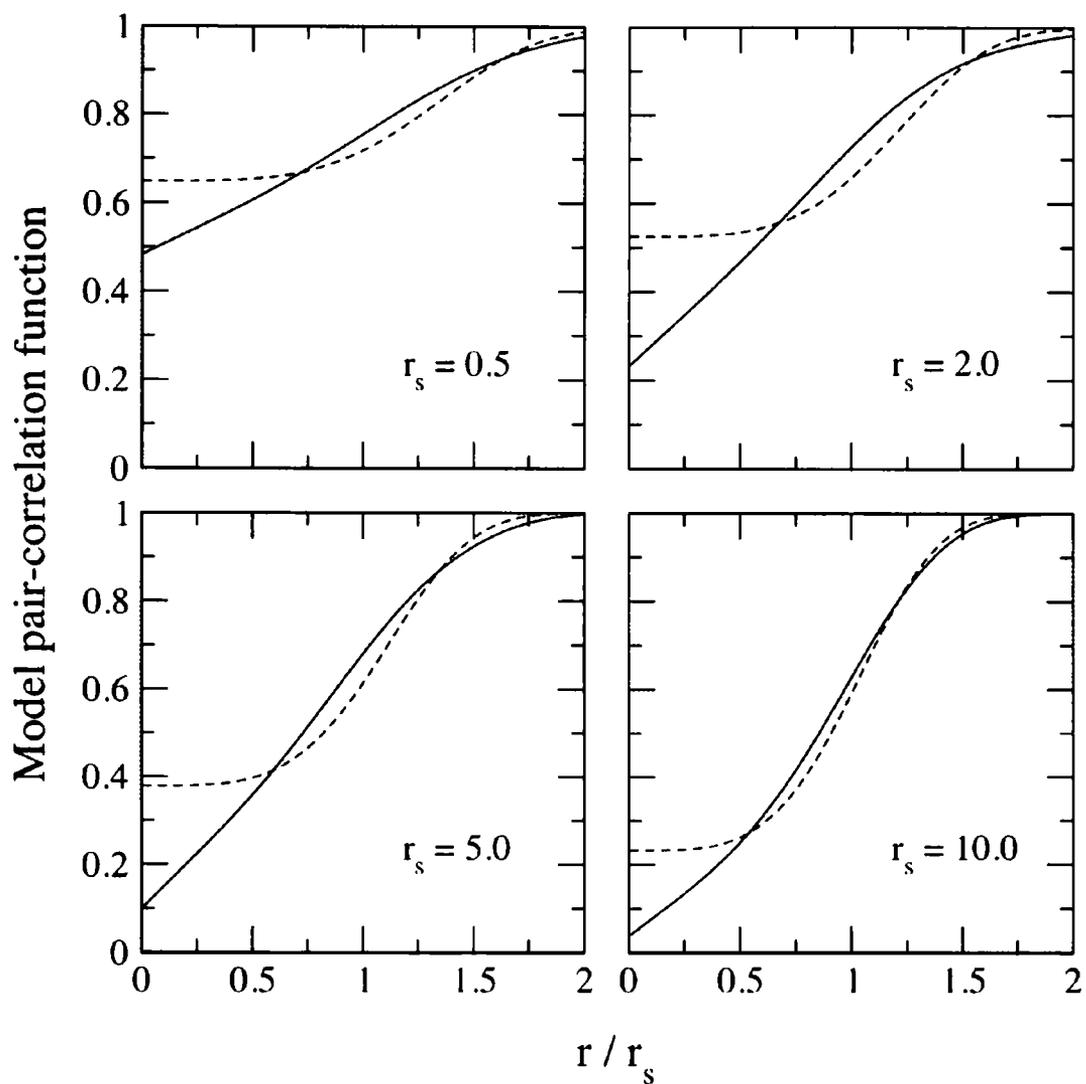
Figure 2.4: Model pair-correlation functions in the homogeneous electron gas at a number of densities for the fourth order Gaussian based model both with (solid line) and without (dashed line) the cusp condition enforced.

Table 2.2: On-top values of the model pair-correlation functions for the Gaussian, fourth order Gaussian and their Kimball cusp condition modified counterparts.

r_s	e^{-u^2}	e^{-u^2} (cusp)	e^{-u^4}	e^{-u^4} (cusp)
0.1	0.564	0.535	0.701	0.655
0.2	0.541	0.488	0.685	0.601
0.4	0.504	0.415	0.660	0.517
0.6	0.473	0.360	0.638	0.453
0.8	0.445	0.315	0.619	0.401
1.0	0.419	0.277	0.601	0.360
2.0	0.309	0.158	0.526	0.232
4.0	0.155	0.056	0.420	0.126
6.0	0.044	0.012	0.343	0.080
8.0	−0.045	−0.010	0.283	0.054
10.0	−0.118	−0.024	0.232	0.038

2.4.3 Application of CWDA to Silicon

Here we apply our Gaussian and fourth order Gaussian based Kimball cusp corrected model pair-correlation functions to bulk silicon. This is the first application of the WDA including the cusp condition to a condensed matter system, for a model pair-correlation function that is not a parameterisation of that in the homogeneous electron gas. Calculations have been done in the WDA with Perdew and Wang's [61] parameterisation for the uniform electron gas in, for example, reference [62]. We compare with the original WDA models, LDA and PBE GGA. Our simulation cell is for the primitive diamond structure, containing two Si atoms, as shown in Figure 2.5. In our calculations we use LDA ultrasoft pseudopotentials, even for the PBE GGA where consistent pseudopotentials are available, as we are interested in comparing the performance of each model for exchange-correlation. A plane wave kinetic energy cutoff of 400 eV was used. Sampling of the Brillouin zone was done using $6 \times 6 \times 6$ Monkhorst-Pack grid of k-points. These criteria converge differences in the total energy to better than 1 meV per atom. For each approximation we calculate
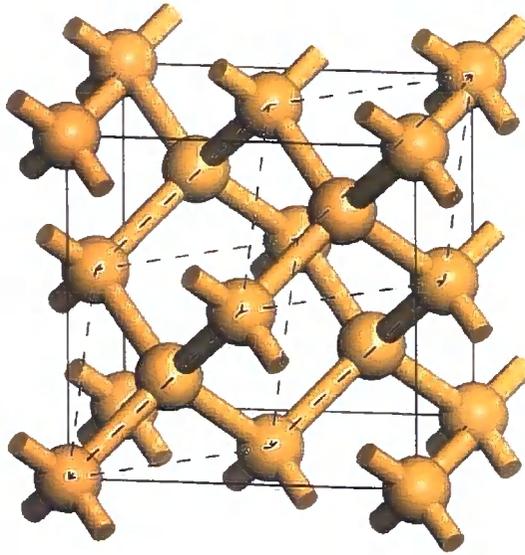
Figure 2.5: The diamond structure of silicon with the primitive cell (dashed lines) overlaid on the face centred cubic cell (solid lines).

the total energy of the system at a number of values for the face centred cubic lattice parameter. The resulting energy-volume curves are fitted to the Murnaghan equation of state to obtain the equilibrium lattice parameter, a_0, and the Bulk modulus, B_0. We also calculate the Kohn-Sham band structure at the equilibrium lattice parameter and at the experimental lattice parameter.

In Table 2.3 we give, for a number of models, the equilibrium lattice parameter, bulk modulus and the indirect band gap at both the equilibrium and experimental lattice parameters. The original Gaussian model already gave a very good estimate for the equilibrium lattice parameter. This is likely because of the good agreement for the exchange-correlation hole between the simple Gaussian WDA and quantum Monte-Carlo data [57]. Our modified function satisfying the cusp condition does shift the estimate of the equilibrium lattice parameter and bulk modulus slightly away from experiment, but only by 0.01 Å and 2 GPa, respectively. It does, however, improve the value for the indirect band gap by 0.1 eV, but still underestimates experiment by a factor of two. For the fourth order Gaussian based model, the cusp condition modification also increases the value of a_0, decreases B_0, and increases the band gap.

Table 2.3: As given by a number of models for exchange-correlation – the equilibrium lattice parameter, a_0, bulk modulus, B_0, and indirect band gap, E_g, for the Kohn-Sham band structure at both the equilibrium and experimental lattice parameter, for silicon.

Model	a_0(Å)	B_0(GPa)	E_g(eV)	E_g(eV, exp. lattice)
e^{-u^2}	5.438	87.5	0.553	0.547
e^{-u^2} (cusp)	5.449	85.7	0.643	0.627
e^{-u^4}	5.402	94.3	0.306	0.333
e^{-u^4} (cusp)	5.433	88.8	0.540	0.539
LDA	5.375	96.6	0.439	0.490
PBE	5.374	92.9	0.624	0.678
Exp.	5.431	98.8	1.17	1.17

It is not clear from this small study if modifying our model pair-correlation functions to satisfy the Kimball cusp condition in this way will provide improvements generally. It does appear that this brings predicted physical properties for Gaussian and fourth order Gaussian models closer together, suggesting that satisfying constraints on the pair-correlation function could provide a systematic method for producing a definitive model for use in the WDA.

2.5 Summary

In this chapter we have given an overview of some of the available approximations for the exchange-correlation energy functional. For the fully non-local WDA we gave the derivation required to implement it efficiently in the context of a plane wave description of the wavefunction and electron density. Four classes of model pair-correlation function were investigated and applied to bulk Cu. It was found that, with the exception of the fourth order Gaussian models, one could select a function that reproduces the experimental lattice parameter and bulk modulus. We conclude that it is not possible to select an appropriate model function for any one system

a priori. In an attempt to rectify this we implemented a new form of model pair-correlation function that satisfies the Kimball cusp condition. For the two models investigated, we found that the on-top value of the pair-correlation function were improved over the previous WDA models. Application of these new models to bulk silicon provided slightly improved indirect band gaps over their original forms, but still differ from experiment by a factor of approximately two. The bulk modulus became slightly worse compared to the original models as did the equilibrium lattice parameter in the modified Gaussian model. The modified fourth order Gaussian function gave an excellent prediction for the equilibrium lattice parameter.

The approach of improving model pair-correlation functions for the WDA by satisfying further physical constraints is promising. Other available routes include satisfying constraints on the spin resolved pair-correlation function or treating exchange and correlation separately. A spin resolved WDA is derived in Chapter 4. Perdew and Wang showed that the Kimball cusp condition is modified for the coupling-constant averaged pair-correlation function [61] that we are attempting to model. Therefore our Kimball cusp satisfying model needs further refinement. Modifications required to implement this are given in Chapter 5 for the WSDA and Chapter 6 for the CWDA discussed in this chapter. Applications of the models including the modified cusp condition are made in Chapter 6.

Chapter 3

WDA Applied to Surfaces

In the previous chapter we introduced the WDA as a method of describing non-local exchange-correlation effects. The considerable increase in computational effort required over semi-local approximations makes it important to concentrate on appropriate applications. Of course, over time this will become less of an issue with the ever increasing efficiency of computer processors and increasing size of parallel computing facilities.

The physical behaviour of interactions at surfaces is intrinsically non-local. For example, the process of a molecule undergoing dissociative adsorption on a surface does not occur at the surface itself, but starts at some distance above the surface [63, 64, 65, 66]. The LDA and various GGAs can only describe such a situation to a limited extent due to their semi-local nature. A measure of whether non-local effects are important can come from studying the behaviour of the exchange-correlation hole.

In this chapter we will show the exchange-correlation hole as calculated with the WDA for metal surfaces, both model and realistic, for there is a wide range of theoretical and experimental data available [64, 67]. The importance of finite cell effects, particularly when using non-local approximations will be discussed. We will then present results obtained from applying the WDA to molecular dissociation of H_2 on the Cu(100) surface.

3.1   Finite Cell Effects on Bulk Systems

In section 2.3.1 we investigated some physical properties of Cu using the WDA with a selection of model pair-correlation functions. In this case we used the primitive cell, doubled along one direction so that we had two atoms per cell and were therefore able to treat the system as spin unpolarised. However, we did not investigate finite cell effects. Finite cell effects are not normally expected when using periodic boundary conditions. However, in a non-local approximation it is possible for the exchange-correlation hole to be extended in some situations. We expect finite cell effects to be important for surfaces but not so significant for bulk properties. This is because the exchange-correlation hole in the bulk is effectively confined by the surrounding electron density. A quantitative study of finite cell effects will be useful in verifying this.

As we expect the effects on the total energy per atom to be small, we will use a kinetic energy cutoff of 1050 eV. This gives us total energy per atom converged to better than 1.0 meV. For the same level of convergence, we choose a Monkhorst-Pack grid of k-points sampling the Brillouin zone with a spacing of 0.044 $Å^{-1}$ (equivalent to a grid of $12 \times 12 \times 12$ k-points in the primitive cell). The same convergence tests were performed using both the LDA and WDA and, as expected, the results were comparable. Throughout this chapter we will use the simple Gaussian model pair-correlation function as this was found to give favourable comparisons with quantum Monte Carlo data in bulk Si [57].

For each calculation within LDA and WDA, we use the equilibrium lattice parameter as calculated in Chapter 2 and shown in Table 2.1. We use cells containing 2, 4, 8 and 16 atoms, corresponding to 2, 4, 8 and 16 of the primitive cells shown in Figure 2.2. We find that the total energy per atom, for each approximation, in all cases is unchanged to less than 1.0 meV. This is to be expected for the WDA in a system such as Cu where there are reasonably high electron densities that confine the exchange-correlation hole. In systems with extended regions of low density, we can expect delocalisation of the exchange-correlation hole and it is in situations such as these that one must be careful to use an appropriately sized super cell. We will now investigate the exchange-correlation hole for metal surfaces.

3.2   Exchange-Correlation Holes in Metal Surfaces

The exchange-correlation hole is essentially the way in which a region of electron density would respond to the presence of another electron placed at any point in space [5]. Consider a test electron placed in otherwise free space in proximity to a surface; the exchange-correlation hole in this case will be within the surface, illustrating the effect the test electron has on the surface electron density. The more diffuse the exchange-correlation hole is, the more pronounced the non-local effect. The correct long range behaviour of the exchange-correlation potential is $-1/r$. In the LDA and GGAs this long range behaviour is an exponential decay [68]. The WDA gives $-1/2r$ in the asymptotic limit [68], the factor of 2 arises from the failure of the WDA model pair-correlation function to be symmetric under exchange of particle positions.

In our implementation, once the weighted density is determined, the exchange-correlation hole, $n_{xc}^{WDA}(r, r')$, at chosen position(s), r, can be calculated at little further expense. We will now apply the WDA to calculate exchange-correlation holes in a near-infinite barrier model jellium surface and the Cu(100) surface.

3.2.1   Jellium Surface

Jellium is the prototype model for metals, simply being a homogeneous electron gas with a uniform positively charged background. As the exact many-electron wave function for jellium can be solved computationally [22], it is a valuable tool for testing the behaviour of density functionals. This is particularly true for functionals in which transferability between many systems is desired. Here, we use a jellium surface in the near-infinite barrier model. This is where a step potential is used, of a height such that the density is zero, to numerical accuracy ($\sim 10^{15}$), beyond the discontinuity in potential. We note that, in real systems, the density often decays exponentially [69] into the vacuum. We stress that this model surface is used an an extreme to illustrate the non-local behaviour of the exchange-correlation hole. By showing that our implementation of the WDA can cater for such extreme and sudden changes in electron density, we can be confident that it can be safely applied

to any realistic surface simulation.

In our model jellium system [70], we used a tetragonal cell with one lattice vector six times the length of the others. We ensured that the cell used was sufficiently large to fully describe the exchange-correlation hole and prevent any periodic boundary effects. This, balanced with use of a high electron density in the jellium slab, confines the exchange-correlation hole so that its width is no larger than the smallest cell dimensions. The jellium slab was thick enough for density oscillations to be negligible in the central region of the slab – fluctuations within 0.5 Å of the centre of the slab are no more than 1% of the central value. We used an electron density equivalent to $r_s = 0.86$ Å, averaged over the slab, which results from the combination of the number of electrons in the cell and the size of the cell chosen such that the calculation does not require excessive computational resources. In order to resolve the exchanege-correlation hole with high quality, we used a real space grid equivalent to a kinetic energy cutoff of 800 eV, which converges the total energy of this system to 1.0 meV.

In Figure 3.1, we show constant density isosurface plots of the exchange-correlation hole for a test electron at various distances z from the surface. At all times the hole is confined within the jellium surface, as required. This is in contrast to the LDA hole that is always spherical and centred on the test electron. For large z the hole remains close to the surface, and while being relatively deep, is confined by the higher local density at the surface. This is due to Friedel oscillations [71], which are oscillations in the electronic wavefunction caused by an impurity, in this case the termination of our surface. As the test electron is moved towards the surface, the hole penetrates deeper into the jellium, becoming more diffuse in the region of uniform density, eventually forming a sphere centered on the test electron once sufficiently within the slab. This compares well with the work of García-González *et al.* [72]

By construction, the exchange-correlation hole in the LDA is spherical and centered on a test electron [73]. This is adequate for systems of nearly uniform electron density, but breaks down at surfaces where the density varies rapidly [69]. In fact, within the LDA, there is the unphysical result that the exchange-correlation hole is
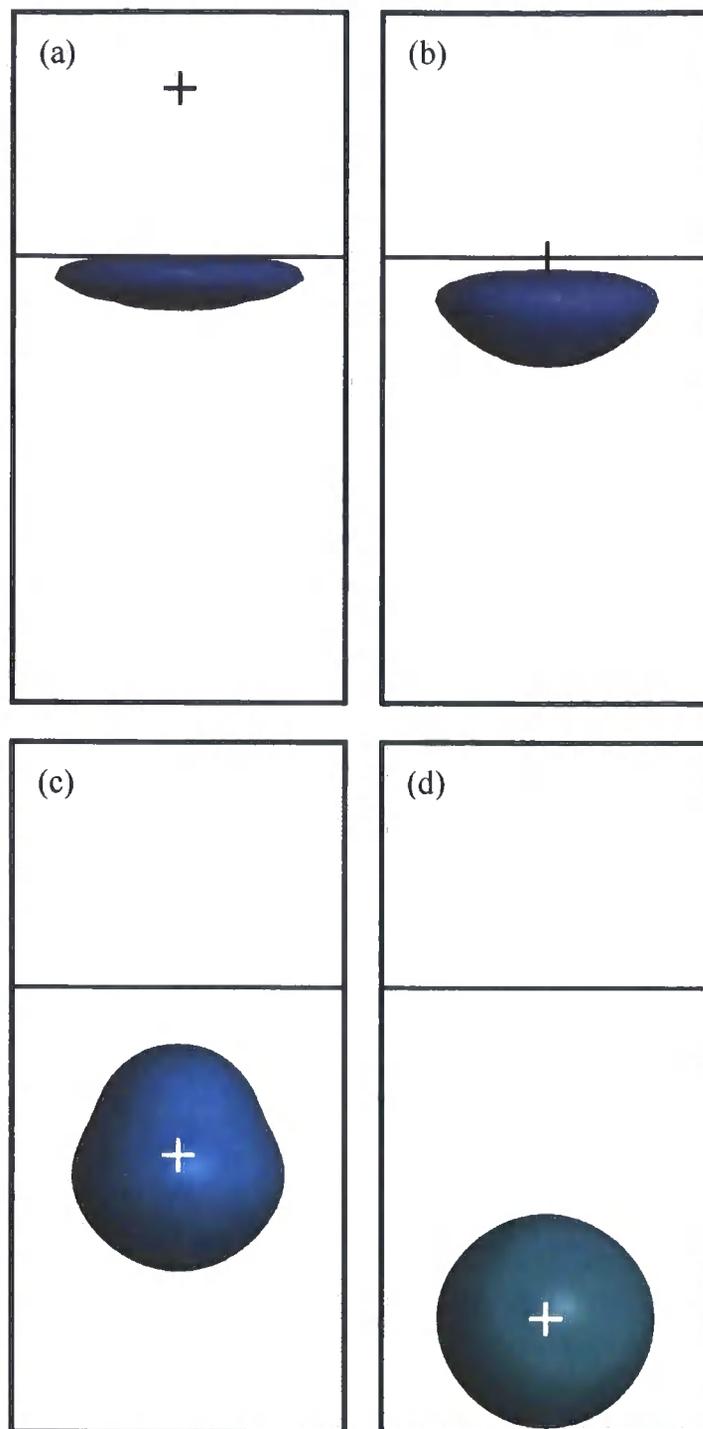
Figure 3.1: Isosurface plots of the exchange-correlation hole in the infinite barrier model jellium surface are shown. For ease of comparison, the value at the isosurface is kept constant between plots. The horizontal line shows the termination of the jellium surface, with vacuum in the top section of the cell. The cross represents the position of the test electron, (a) $z = 2$ Å above the surface, (b) $z = 0$ Å, at the surface and (c) $z = -2$ Å and (d) $z = -4$ Å within the jellium.

undefined in the vacuum region, in spite of being in proximity of an electron density. Gunnarsson and Lundqvist also state that to a local approximation, the exchange-correlation energy is insensitive to the details of the hole. The exchange-correlation potential, however, is not guaranteed to have this insensitivity. In the WDA, the shape of the exchange-correlation hole is implicitly used when calculating the potential. Our findings for the jellium surface demonstrates that the exchange-correlation hole calculated in the WDA is qualitatively closer to that from quantum Monte Carlo calculations of reference [69] while retaining the successful description given by the LDA in the uniform limit.

3.2.2 Cu(100) Surface

Next we turn to a more realistic model in the form of the Cu(100) surface. Here, we used a slab that is five atomic layers thick, comparable with other studies on the Cu(100) system, [64] while keeping the atoms fixed at the experimental value for the bulk Cu structure. Note that including the relaxation of the surface layers would shift the atoms a small amount towards the slab centre and this would have only a small effect on the exchange-correlation hole. Particularly, the separation of the test charge and exchange-correlation hole centre would remain mostly unchanged. Again, a supercell large enough to describe the holes in the region of interest without any periodic boundary effects was used; we found that a unit cell of $5.11 \times 5.11 \times 21.69$ Å^3 containing 14.46 Å of vacuum was sufficient. Convergence tests for the total energy were performed on this cell using the LDA (as the form of the exchange-correlation functional would not significantly change these), finding that an 800 eV planewave cutoff energy and a $10 \times 10 \times 1$ Monkhorst-Pack grid of k-points was adequate. An ultrasoft pseudopotential was used, which was generated using the LDA. We then used the electron density found using the LDA as a starting point for minimising the total energy with the WDA, rather than starting with a randomised wave function. This was done to significantly reduce the total computational time required.

The surface energy for Cu(100) was calculated using both the LDA and WDA. In the LDA, we obtained a value of 2.2 J/m^2, which is somewhat higher than the experimental value [74] of 1.77 J/m^2. This is to be expected as relaxation of the
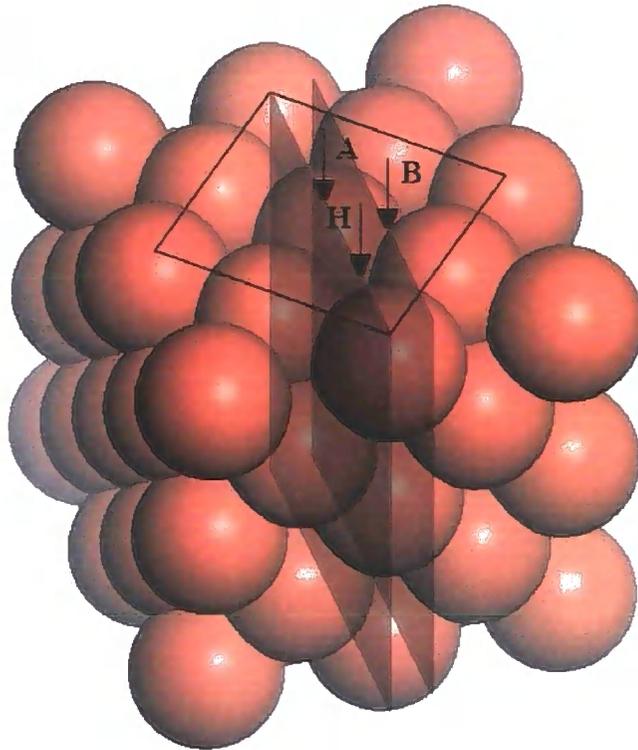
Figure 3.2: Schematic of the Cu(100) surface and marked points of symmetry; A, H and B are referred to as the atom, hollow and bridge-sites, respectively. The box marks the edges of the supercell used and the vertical planes show the orientation of the slices taken for the contour plots in Figures 3.3, 3.4 and 3.5.

surface layers is not included. Using the WDA, we obtained a value of 1.13 J/m^2, which is low, but can be explained by the underbinding for bulk Cu found when using the simple Gaussian form of the model pair-correlation function, as we established in section 2.3.1. The discrepancies for both approximations could also be accounted for by the fact that we are using the experimental lattice, rather than the equilibrium structure given by each level of approximation.

We have calculated the exchange-correlation holes at various distances z from the surface above three points of symmetry, A, B and H, on the surface as shown in Figure 3.2. In each case, the test electron is positioned at a number of points, those at $z = 2.89$ Å, $z = 1.81$ Å, $z = 0.72$ Å above and $z = -0.14$ Å below the surface. Here we define the surface to be the the plane intersecting the Cu centres
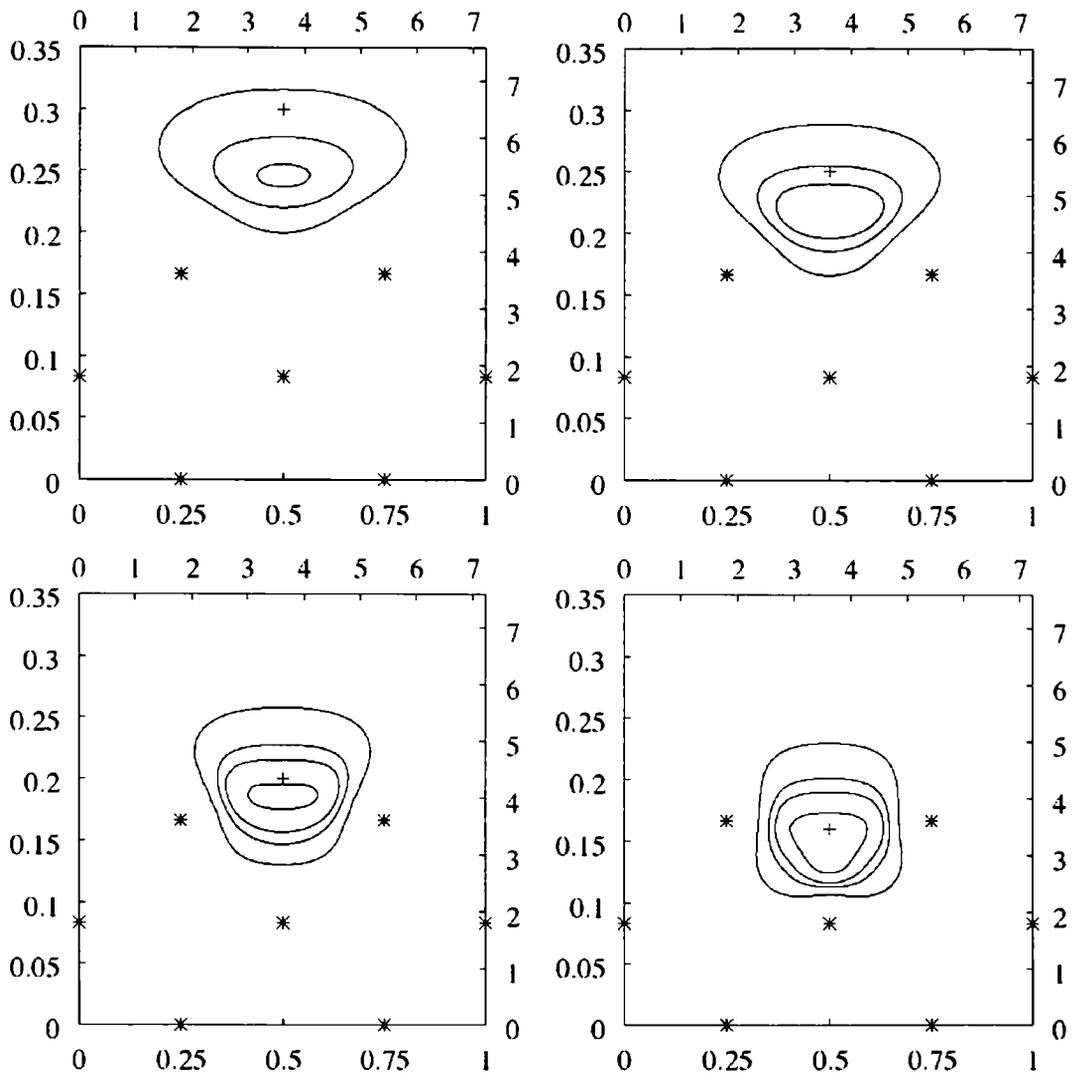
Figure 3.3: Contour plots of the exchange-correlation hole at various points along the vertical line through the hollow site, H. The cross represents the position of the test electron and the stars the positions of the Cu atoms. The left and bottom axes are in fractional units of the slice taken bounded by the cell, and the right and top axes units are in Å. See main text for more details.
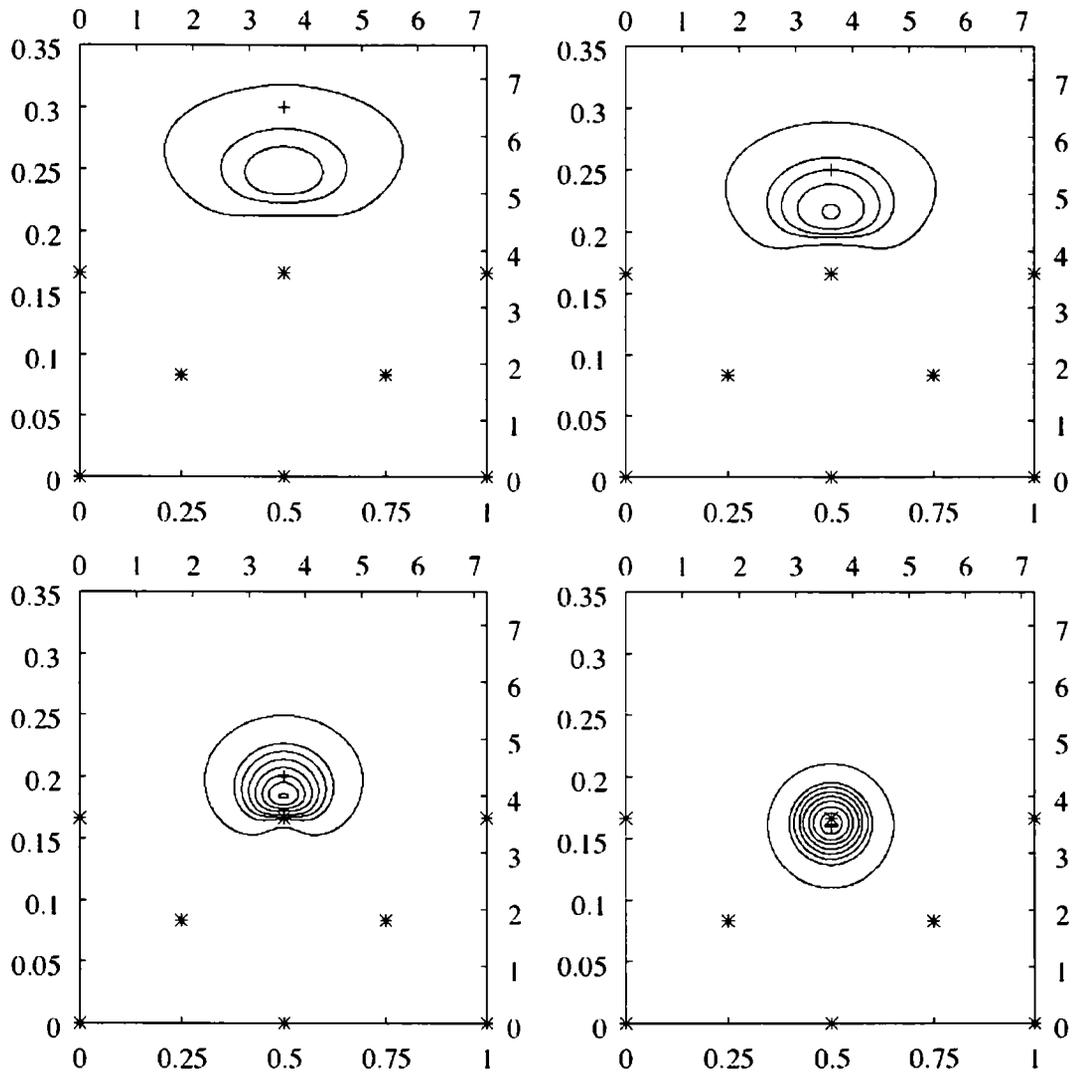
Figure 3.4: As for Figure 3.3 but for the line through the atom site, A. Note that the contours here are spaced exactly as in Fig. 3.3 to allow a direct comparison.
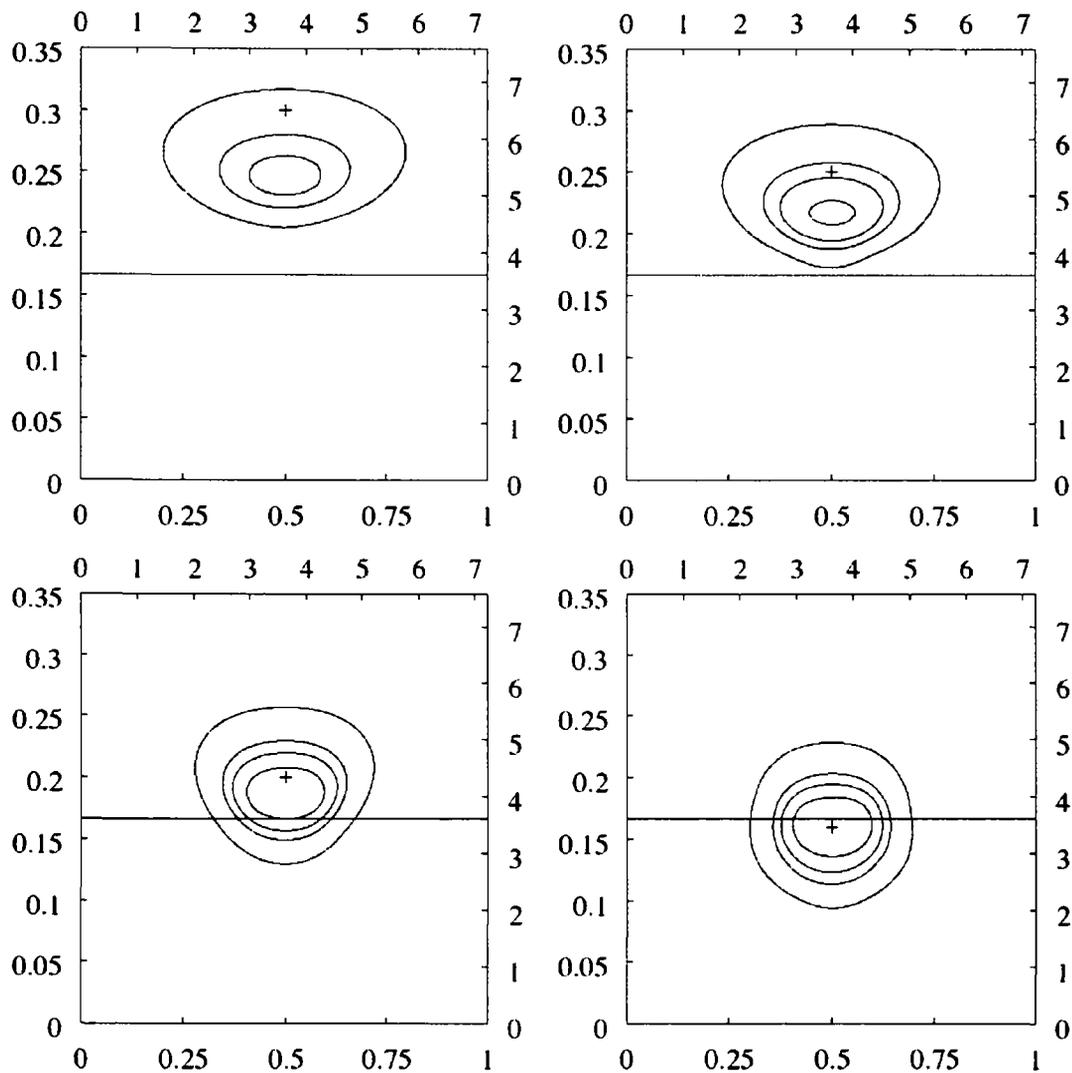
Figure 3.5: As for Figure 3.3 but for the bridge site, B. As there are no atom centres in this plane, the line shows the position of the top layer of atoms.
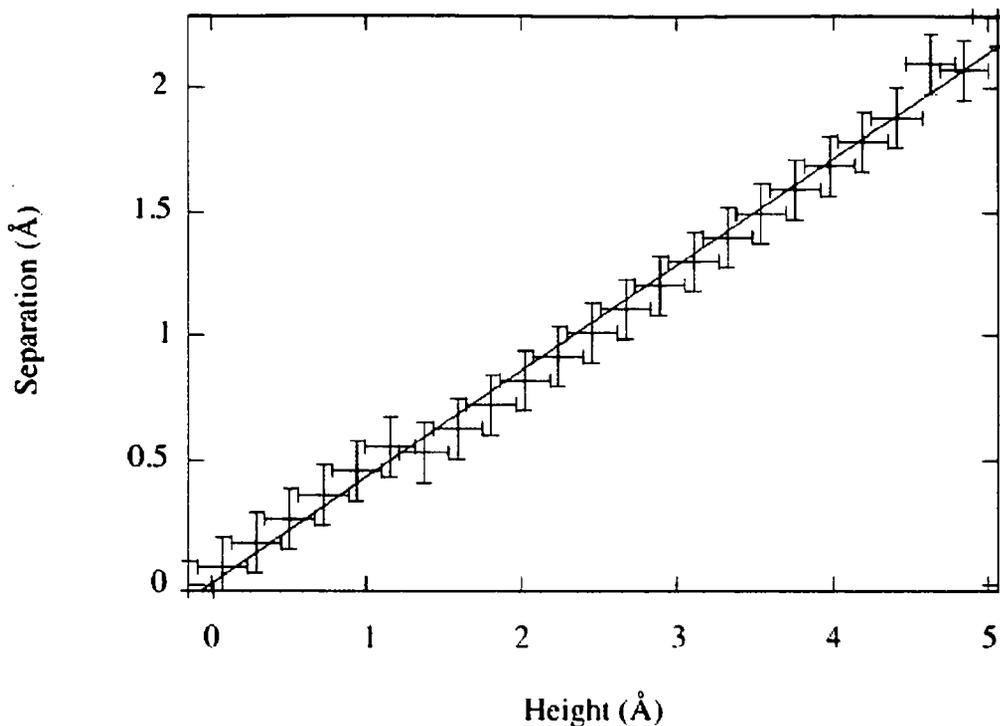
Figure 3.6: Plot showing the linear relationship between test charge to hole centre separation and the height of the test charge above the surface. Error bars are due to the precision of the sampling in the plane. Shown here for the atom site, those for the hollow and bridge site are identical within sampling accuracy.

of the uppermost layer. For each of the points of symmetry, we show the exchange-correlation hole of the test electron in Figures 3.3–3.5. The equivalent figures for the LDA would simply have a sphere centred on the test electron. Each pair of contour lines has a spacing double that of the previous pair, illustrating the sharp increase in the depth of the exchange-correlation hole as the test electron is moved into the surface and regions of higher electron density.

We find that the non-local effects are evident when looking at the distance between the test electron and the deepest point of the exchange-correlation hole. In each of the cases this distance takes values approximately 1.20, 0.72, 0.36, and 0.02 Å at the previously mentioned positions, respectively. It is found that there is a linear relationship between the separation and the height of the test electron above the surface, as shown in Figure 3.6. In the context of density functional calcu-

lations with surfaces, for example, molecular adsorption and epitaxial growth, this demonstrates that there could be significant errors in using semi-local functionals.

3.3 H_2 Dissociation on Cu(100)

A number of theoretical studies of Cu surfaces agree that the reaction path for a H_2 molecule starts within approximately 2.5 Å of the surface [64, 65, 66, 75]. The exchange-correlation holes calculated using the WDA shown in the previous section demonstrate that there is a significant non-local effect in this region. Often used in such studies is a potential energy surface, essentially a multidimensional analysis of the total energy of the system while varying parameters such as the height of the molecule above the surface, bond length of the molecule and orientation of the molecule with respect to the surface. This potential energy surface can then be used to determine the classical reaction path and energy barriers. Critical features such as minima and saddle points can be very sensitive to the level of approximation used for exchange-correlation.

In the case of a diatomic molecule, the potential energy surface is six dimensional. For an approximation as computationally expensive as the WDA, particularly where large simulation cells are involved, it is currently unfeasible to determine the full potential energy surface. Instead we will determine a two dimensional potential energy surface for the height of the molecule above the surface and the separation of the hydrogen atoms in the molecule. Based on the work of White and Bird, who used the LDA, we will orient the molecule parallel to the surface, with the bond centered above the bridge site (see Figure 3.2) and the bond aligned along neighbouring hole sites.

For our calculations, we used a slab of Cu five layers thick in a cell of dimensions $5.11 \times 5.11 \times 21.69$ Å^3, which contains 14.46 Å of vacuum to avoid interaction between either sides of the slab and has a total of twenty Cu atoms. To converge our total energy to better than 1 meV a plane wave cutoff energy of 1200 eV was used and k-point sampling of the Brillouin zone was done using a Monkhorst-Pack grid of points $8 \times 8 \times 1$. Ultrasoft pseudopotentials were used that were generated using

the LDA.

Figure 3.7 shows the two dimensional potential energy surface generated using the WDA. We calculated the total energy at 35 points and used a cubic interpolation scheme that we then contoured. The contour lines are spaced at 0.05 eV intervals. For each point we did an initial calculation with the LDA then used the electron density found here as the starting point for our self consistent WDA calculation. This reduces the number of self consistent cycles required so that there are fewer calculations of the weighted density, greatly reducing the overall calculation time. The WDA calculations each took 7–10 days running on 128 opteron processors with a clock speed of 2 GHz.

Qualitatively, large differences can readily be seen between our potential energy surface and those done previously with the LDA [64] and GGA [65]. In those cases, the potential energy surface has a single saddle point at a height and bond length of 1.04 Å and 1.28 Å, respectively for the LDA and 1.09 Å and 1.40 Å, respectively for the PW91 GGA. Our calculations using the WDA, however, have two saddle points and a local minimum. The potential energy surface for our LDA calculation is shown in Figure 3.8. This differs also from previous studies, having a single saddle point and local minimum. This could be an indication that the previous studies used supercells that were of an inadequate size. White and Bird's LDA calculations used a cell 2.55×2.55 Å^2 in cross section while their GGA calculations used a cell 3.61×3.61 Å^2 in cross section. The larger cross section in our simulations should be enough to eliminate periodic boundary effects. This was expected for the WDA given the exchange-correlation holes calculated in the previous section but not immediately so for the LDA. It should be noted that preliminary calculations we performed with the smaller 3.61×3.61 Å^2 cross section were comparable to those found in the above references, with the WDA also returning a potential energy surface with a single saddle point.

The final adsorbed positions for the hydrogen atoms is found to be 0.352 Å above the surface. This is in comparison with White and Bird's LDA value of 0.43 Å and our own LDA value of 0.349 Å. The differences between our LDA calculation and White and Bird's calculation can be most likely be attributed to their use of norm
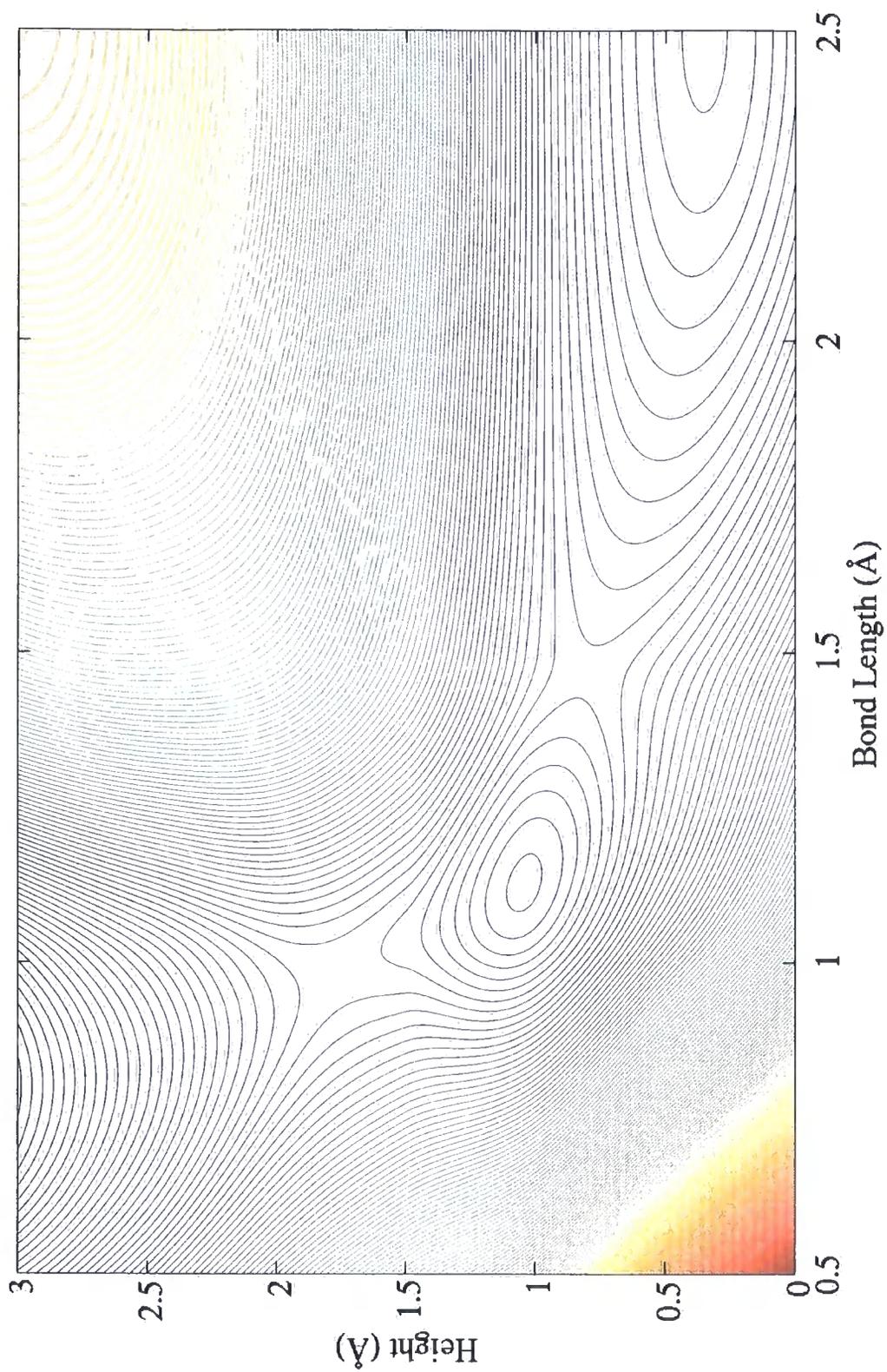
Figure 3.7: Potential energy surface for H_2 on Cu(100), generated using the WDA.
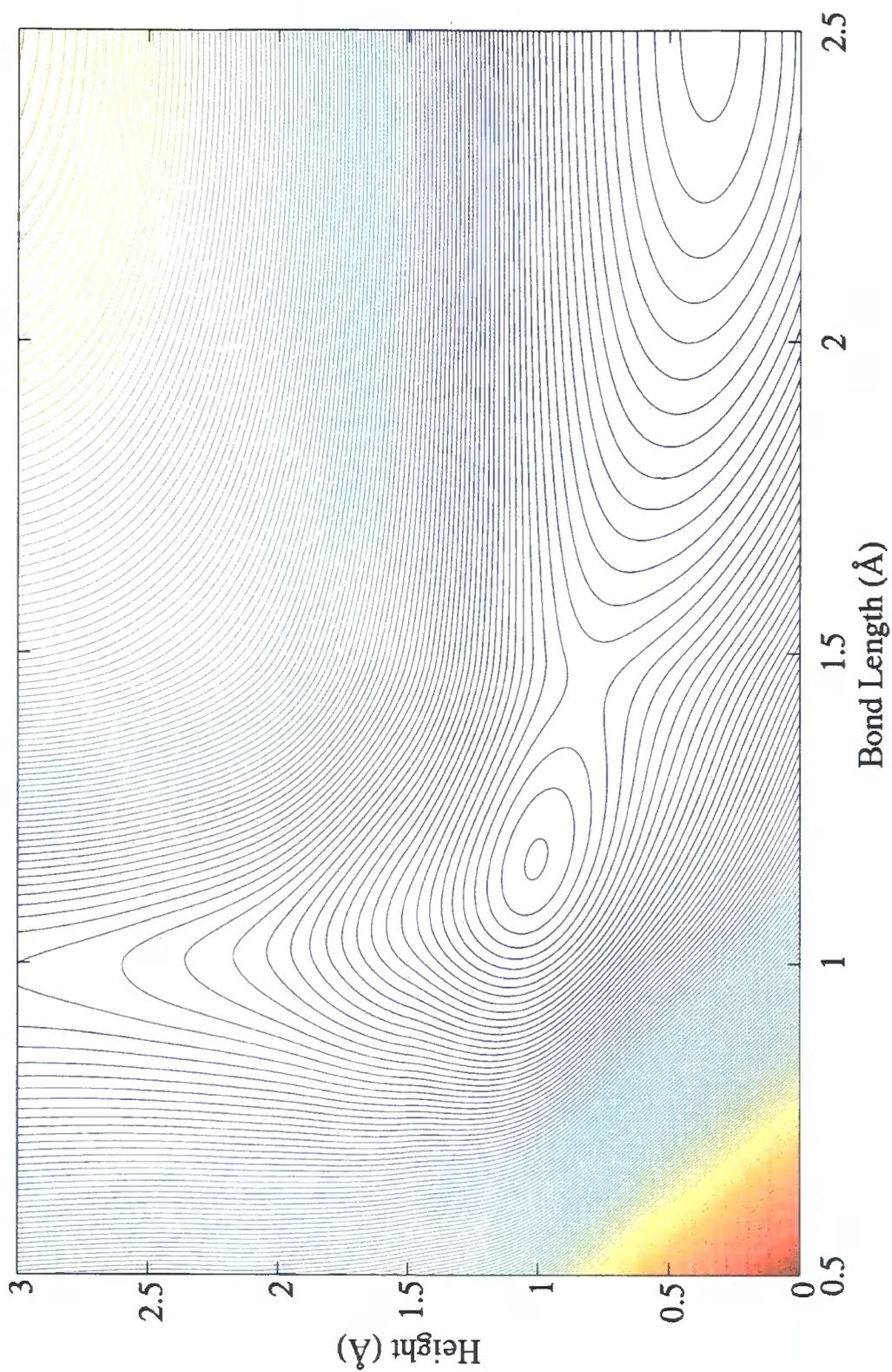
Figure 3.8: Potential energy surface for H_2 on Cu(100), generated using the LDA.

conserving pseudopotentials as opposed to the ultrasoft pseudopotentials used in our calculations. A combination of the larger supercell used, the higher kinetic energy cutoff and k-point sampling used in our calculations may also contribute. In both cases the hydrogen atoms sit above the hole sites in this final state. Our LDA calculation gives a local minimum at 1.01 Å above the surface with a bond length of 1.17 Å and a saddle point at a height of 0.82 Å and a bond length of 1.44 Å. The calculations performed using the Gaussian based WDA has a local minimum at 1.04 Å above the surface and a bond length of 1.13 Å. The two saddle points in this case are at heights and bond lengths of 1.77 Å and 0.99 Å, and 0.80 Å and 1.47 Å, respectively.

The classical reaction path can be determined by following the "valley" formed by the potential energy surface. We can then take the energy values along this path to observe the variations in the energy along the reaction path, which allows us to determine the height of energy barriers. In Figures 3.9 and 3.10 we show the energy relative to the final adsorbed state along the classical reaction path for the LDA and WDA, respectively. The minima in these graphs correspond to the minima in our two dimensional potential energy surface, while the maxima correspond to the saddle points.

Our results using the LDA suggest that the process has no barrier to adsorption. This is at odds with experiment showing definitively that the process is activated and dissociative [76]. From our data, there is a small barrier of 0.143 eV to escape the local minimum. White and Bird [64] reported a barrier height of 0.30 eV, compared to a value of 0.5–0.7 eV inferred from experiment. White *et al.* later report a barrier of 0.06 eV using the LDA and 0.99 eV with a GGA [65]. Using the WDA, our results show that the process is activated, as it should be. The barrier height is higher than expected at approximately 1.2 eV. A second barrier, after a local minimum, is 0.277 eV in height.

Calculations of dissociative adsorption of H_2 on Cu(100) using the WDA provide significant differences over previous work using semi-local approximations for exchange-correlation. Some of these differences may be accounted for by the use of a larger cross section in our simulation cell as significant changes to the poten-
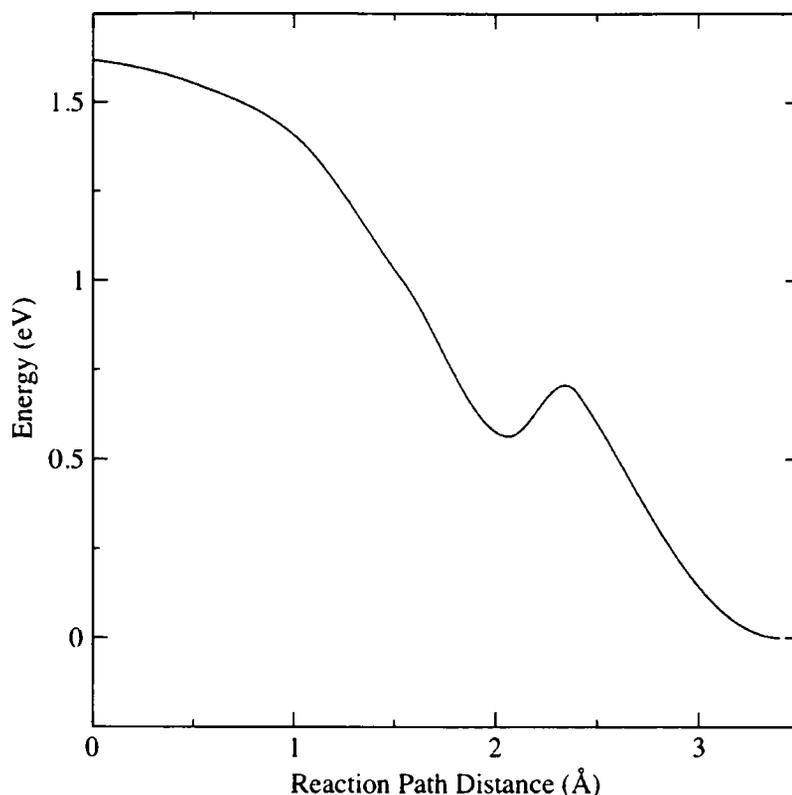
Figure 3.9: Relative energy along the reaction path calculated using the LDA. We set our zero energy to be the final adsorbed state.

tial energy surface calculated with the LDA were also seen. The incorrect image potential given by the WDA in this form could also be a factor. Our relatively coarse sampling of the two dimensional potential energy surface may have a small effect. However, a sample size of 35 points was adequate in previous studies. Calculations with higher resolution sampling could be useful, particularly around the saddle points and local minima. We have not investigated the effect of using different model pair-correlation functions within the WDA. As was shown in section 2.3.1, we can obtain results closer to experiment by selecting particular functional forms. There is, however, no way of choosing a model pair-correlation function in advance, and little would be gained from repeating our calculations with each of the many models available. Throughout the remainder of this thesis we discuss a number of different avenues for improving the WDA, including the possibility of a model pair-correlation function based purely on physical constraints.
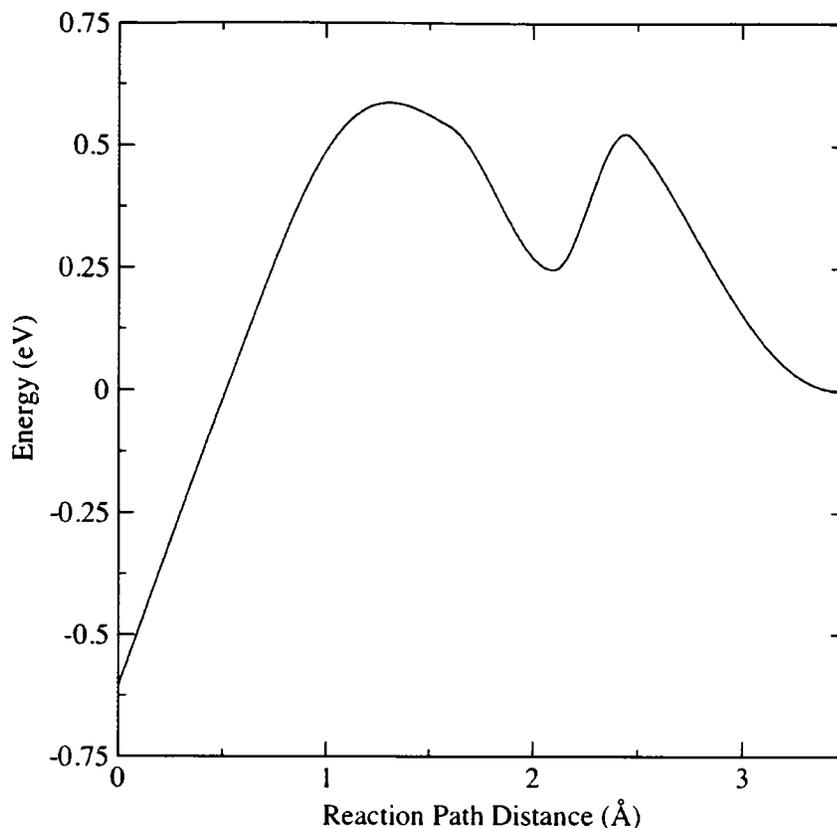
Figure 3.10: Relative energy along the reaction path calculated using the WDA. We set our zero energy to be the final adsorbed state.

3.4 Summary

In this chapter we have applied the WDA to metal surfaces. We have demonstrated that, as expected, finite cell errors are negligible for calculations of this type for bulk solids. However, in the case of surface modeling, finite cell effects are evident. This is emphasised by the spatial extent of the exchange-correlation hole as calculated using the WDA. Calculations of part of the potential energy surface for H_2 dissociating on the Cu(100) surface show that finite cell errors may be present for work previously done using semi-local approximations. When applying the WDA to this system, significant differences were found to semi-local studies. Limitations on our ability to choose an appropriate model pair-correlation function cast doubt on the benefit of performing such large scale, computationally expensive, calculations with the WDA. A non-local approximation for exchange-correlation does appear to be required for

accurate density functional simulations of surfaces. We suggest that the models for the exchange-correlation hole in the WDA can be refined by including more physical constraints such as the Kimball cusp condition (see section 2.4) and constraints on the spin resolved pair-correlation function (chapter 4). Once a non-empirical model pair-correlation can be used in the WDA, it will be of interest to return to these surface calculations.

Chapter 4

Weighted Spin Density Approximation

Previous attempts have been made at constructing and implementing a spin polarised extension to the WDA [77, 78]. Although referred to as a weighted spin density approximation (WSDA), these implementations used a WDA treatment of exchange only. Such a method is relatively easy to implement as the form for the pair-correlation function for exchange in the homogeneous electron gas is known [79]. For correlation effects, the LSDA correlation energy was used, so non-local correlation cannot be described. While these showed improvements over LDA on its own, they are not true non-local approximations. Gunnarsson and Jones [55] suggested that spin polarisation can be included by replacing the LDA energy density with the LSDA energy density. Although simple, this method of including spin polarisation can not reproduce the correct pair-correlation function in the partial or fully polarised uniform limit because the model pair-correlation functions used do not have any dependance on the spin polarisation. In this chapter we will construct a framework for a fully non-local WSDA and show an efficient implementation that can be run in parallel within the CASTEP code. Note that we do not intend to make thorough tests of model pair-correlation functions here, merely to demonstrate our method.

4.1   Spin Resolved Pair-Correlation Function

The basis for all approximations of the weighted density type is the pair-correlation function. For a spin polarised extension the pair-correlation function needs to be spin resolved. From Becke [80], the pair probability density, i.e. the probability of finding one electron at r given that there is another at r', can be written to include spin orientation as:

$$P(r, r') = \sum_{\sigma, \sigma'} P^{\sigma\sigma'}(r, r') = P^{\uparrow\uparrow}(r, r') + P^{\uparrow\downarrow}(r, r') + P^{\downarrow\uparrow}(r, r') + P^{\downarrow\downarrow}(r, r'), \quad (4.1)$$

where σ and σ' represent the spin orientation for the electron at r and r', respectively. It is worth noting here that as the pair probability density is identical, as it should be, when interchanging r and r', therefore the two probabilities for antiparallel spins are identical.

The spin resolved (coupling-constant averaged) exchange-correlation hole and pair-correlation function is related to the pair probability density by:

$$P^{\sigma\sigma'}(r, r') = n_\sigma(r) n_{xc}^{\sigma\sigma'}(r, r') + n_\sigma(r) n_{\sigma'}(r') = n_\sigma(r) n_{\sigma'}(r') g_{xc}^{\sigma\sigma'}(r, r'), \quad (4.2)$$

where we have $n_\sigma(r)$ the electron density with spin σ, we introduce the spin resolved exchange-correlation hole $n_{xc}^{\sigma\sigma'}(r, r')$, and also the spin resolved pair-correlation function $g_{xc}^{\sigma\sigma'}(r, r')$. The spin resolved exchange-correlation hole and pair-correlation function are related to each other by:

$$n_{xc}^{\sigma\sigma'}(r, r') = n_{\sigma'}(r') \left[g_{xc}^{\sigma\sigma'}(r, r') - 1 \right]. \quad (4.3)$$

Using the relation of the full pair probability density to the full pair-correlation function from equation 2.8 and equations 4.1 and 4.2 we obtain a spin resolved

pair-correlation function:

$$g_{xc}(\boldsymbol{r}, \boldsymbol{r}') = \sum_{\sigma,\sigma'} \frac{n_\sigma(\boldsymbol{r})n_{\sigma'}(\boldsymbol{r}')}{n(\boldsymbol{r})n(\boldsymbol{r}')} g_{xc}^{\sigma\sigma'}(\boldsymbol{r}, \boldsymbol{r}'), \tag{4.4}$$

and a spin resolved exchange correlation hole:

$$n_{xc}(\boldsymbol{r}, \boldsymbol{r}') = \frac{1}{n(\boldsymbol{r})} \sum_{\sigma,\sigma'} n_\sigma(\boldsymbol{r}) n_{xc}^{\sigma\sigma'}(\boldsymbol{r}, \boldsymbol{r}'), \tag{4.5}$$

which are exact relations. Equation 4.4 is equivalent to the spin resolved pair-correlation function given elsewhere (for example, in reference [81]), expressed in terms of spin polarisation, $\zeta = (n_\uparrow(\boldsymbol{r}) - n_\downarrow(\boldsymbol{r}))/n(\boldsymbol{r})$:

$$g_{xc}(\boldsymbol{r}, \boldsymbol{r}') = \left(\frac{1+\zeta}{2}\right)^2 g_{xc}^{\uparrow\uparrow}(\boldsymbol{r}, \boldsymbol{r}') + \left(\frac{1-\zeta}{2}\right)^2 g_{xc}^{\downarrow\downarrow}(\boldsymbol{r}, \boldsymbol{r}') + \left(\frac{1-\zeta^2}{2}\right) g_{xc}^{\uparrow\downarrow}(\boldsymbol{r}, \boldsymbol{r}'), \tag{4.6}$$

where $g_{xc}^{\uparrow\downarrow}(\boldsymbol{r}, \boldsymbol{r}') = g_{xc}^{\downarrow\uparrow}(\boldsymbol{r}, \boldsymbol{r}')$. It should be noted that the parts for antiparallel spin pairs do not experience Pauli exclusion as they have different spin indices. Strictly, one should say that the contribution from antiparallel spin pairs is purely from correlation effects.

Here we shall list some of the exact constraints on the exchange-correlation hole and the pair-correlation function. The spin resolved exchange-correlation hole obeys a sum rule, summarised as:

$$\int n_{xc}^{\sigma\sigma'}(\boldsymbol{r}, \boldsymbol{r}') d\boldsymbol{r}' = -\delta_{\sigma,\sigma'}, \tag{4.7}$$

where we use the Kronecker delta. The spin resolved pair-correlation function must also satisfy a number of properties in all cases, not just the homogeneous limit [82]:

(i) Each part of the pair-correlation function must be positive at all times, i.e.

$$g_{xc}^{\sigma\sigma'}(\boldsymbol{r}, \boldsymbol{r}') \geq 0. \tag{4.8}$$

(ii) When $r = r'$, we have for parallel spins, from the Pauli exclusion principle,

$$g_{\text{xc}}^{\uparrow\uparrow}(r, r) = g_{\text{xc}}^{\downarrow\downarrow}(r, r) = 0, \tag{4.9}$$

and for antiparallel spins, we have,

$$g_{\text{xc}}^{\uparrow\downarrow}(r, r) \geq 0. \tag{4.10}$$

(iii) As r tends towards r' the derivatives of the pair-correlation function with respect to the separation have the following relations for parallel spins,

$$\frac{\partial}{\partial |r - r'|} g_{\text{xc}}^{\sigma\sigma}(r, r') \bigg|_{r \to r'} = 0, \tag{4.11}$$

$$\frac{\partial^2}{\partial |r - r'|^2} g_{\text{xc}}^{\sigma\sigma}(r, r') \bigg|_{r \to r'} = \frac{2}{3} \frac{\partial^3}{\partial |r - r'|^3} g_{\text{xc}}^{\sigma\sigma}(r, r') \bigg|_{r \to r'}. \tag{4.12}$$

For antiparallel spins we have,

$$\frac{\partial}{\partial |r - r'|} g_{\text{xc}}^{\sigma\sigma'}(r, r') \bigg|_{r \to r'} = g_{\text{xc}}^{\sigma\sigma'}(r, r') \bigg|_{r \to r'}. \tag{4.13}$$

These constraints are a result of Fermions interacting in a pairwise Coulomb interaction in three dimensions [82].

Other constraints are known for exchange and correlation separately, as well as relations to the exchange and correlation energy densities and potentials. The choice

of model pair-correlation function will be discussed later. However, a good choice of model pair-correlation function should satisfy the above properties.

Strictly speaking, we are considering the coupling-constant averaged pair-correlation function, which is the integral of the pair-correlation function over the coupling constant for the Coulomb force from the noninteracting case to the fully interacting case. This leads to a set of modified cusp conditions [61] that should be taken into account. For now, we will follow the work of Rushton [59] and construct a model that does not include the modified cusp conditions. We will discuss the inclusion of the modified cusp condition in the next chapter.

4.2 Exchange-Correlation Energy and Potential

In analogy with the existing, non-polarised WDA, we will use $G^{\sigma\sigma'}$ to represent our model pair-correlation function:

$$G^{\sigma\sigma'}[\boldsymbol{r}, \boldsymbol{r}'; \tilde{n}_\uparrow(\boldsymbol{r}), \tilde{n}_\downarrow(\boldsymbol{r})] = g_{\mathrm{xc}}^{\sigma\sigma'}(\boldsymbol{r}, \boldsymbol{r}') - 1, \tag{4.14}$$

where $\tilde{n}_\uparrow(\boldsymbol{r})$ and $\tilde{n}_\downarrow(\boldsymbol{r})$ are the weighted spin density parameters. We can then write the exchange-correlation energy using the spin resolved model pair-correlation function:

$$
\begin{aligned}
E_{\mathrm{xc}}^{\mathrm{WSDA}}[n_\uparrow, n_\downarrow; \tilde{n}_\uparrow, \tilde{n}_\downarrow] &= \frac{1}{2} \int n_\uparrow(\boldsymbol{r}) d\boldsymbol{r} \int n_\uparrow(\boldsymbol{r}') \frac{G^{\uparrow\uparrow}[\boldsymbol{r}, \boldsymbol{r}'; \tilde{n}_\uparrow(\boldsymbol{r})]}{|\boldsymbol{r} - \boldsymbol{r}'|} d\boldsymbol{r}' \\
&+ \frac{1}{2} \int n_\downarrow(\boldsymbol{r}) d\boldsymbol{r} \int n_\downarrow(\boldsymbol{r}') \frac{G^{\downarrow\downarrow}[\boldsymbol{r}, \boldsymbol{r}'; \tilde{n}_\downarrow(\boldsymbol{r})]}{|\boldsymbol{r} - \boldsymbol{r}'|} d\boldsymbol{r}' \\
&+ \frac{1}{2} \int n_\uparrow(\boldsymbol{r}) d\boldsymbol{r} \int n_\downarrow(\boldsymbol{r}') \frac{G^{\uparrow\downarrow}[\boldsymbol{r}, \boldsymbol{r}'; \tilde{n}_\uparrow(\boldsymbol{r}), \tilde{n}_\downarrow(\boldsymbol{r})]}{|\boldsymbol{r} - \boldsymbol{r}'|} d\boldsymbol{r}' \\
&+ \frac{1}{2} \int n_\downarrow(\boldsymbol{r}) d\boldsymbol{r} \int n_\uparrow(\boldsymbol{r}') \frac{G^{\uparrow\downarrow}[\boldsymbol{r}, \boldsymbol{r}'; \tilde{n}_\uparrow(\boldsymbol{r}), \tilde{n}_\downarrow(\boldsymbol{r})]}{|\boldsymbol{r} - \boldsymbol{r}'|} d\boldsymbol{r}'.
\end{aligned}
\tag{4.15}
$$

We will refer to each of the four parts such that:

$$E_{xc}^{WSDA}[n_\uparrow, n_\downarrow; \tilde{n}_\uparrow, \tilde{n}_\downarrow] = \quad E_{xc}^{\uparrow\uparrow}[n_\uparrow; \tilde{n}_\uparrow] + E_{xc}^{\downarrow\downarrow}[n_\downarrow; \tilde{n}_\downarrow]$$

$$+ \quad E_{xc}^{\uparrow\downarrow}[n_\uparrow, n_\downarrow; \tilde{n}_\uparrow, \tilde{n}_\downarrow] + E_{xc}^{\downarrow\uparrow}[n_\uparrow, n_\downarrow; \tilde{n}_\uparrow, \tilde{n}_\downarrow]. \qquad (4.16)$$

We can also spin resolve the exchange-correlation energy density:

$$\varepsilon_{xc}(r) = \sum_{\sigma,\sigma'} \frac{n_\sigma(r)}{n(r)} \frac{1}{2} \int \frac{n_{xc}^{\sigma\sigma'}(r,r')}{|r-r'|} dr' = \sum_{\sigma,\sigma'} \frac{n_\sigma(r)}{n(r)} \varepsilon_{xc}^{\sigma\sigma'}(r). \qquad (4.17)$$

The potential, including spin, is determined from the functional derivative of the exchange-correlation energy with respect to the electron density of a given spin orientation:

$$v_{xc}^\sigma(r) = \frac{\delta E_{xc}[n(r)]}{\delta n_\sigma(r)}. \qquad (4.18)$$

For parallel spins, the potential can be split into three terms, as with the non-polarised WDA. For antiparallel spins, we get four terms, giving the spin resolved potential a total of seven terms:

$$v_{xc}^\sigma(r) = v_1^\sigma(r) + v_2^\sigma(r) + v_3^\sigma(r) + v_4^\sigma(r) + v_5^\sigma(r) + v_6^\sigma(r) + v_7^\sigma(r), \qquad (4.19)$$

where σ can be up ($\uparrow$) or down ($\downarrow$). The first three terms in the up ($\uparrow$) case come only from $E_{xc}^{\uparrow\uparrow}$, there are no contributions from $E_{xc}^{\downarrow\downarrow}$:

$$v_1^\uparrow = \frac{1}{2} \int n_\uparrow(r') \frac{G^{\uparrow\uparrow}[r, r'; \tilde{n}_\uparrow(r)]}{|r - r'|} dr', \tag{4.20}$$

$$v_2^\uparrow = \frac{1}{2} \int n_\uparrow(r') \frac{G^{\uparrow\uparrow}[r, r'; \tilde{n}_\uparrow(r')]}{|r - r'|} dr', \tag{4.21}$$

$$v_3^\uparrow = \frac{1}{2} \int n_\uparrow(r') dr' \int \frac{n_\uparrow(r'')}{|r' - r''|} \frac{\delta G^{\uparrow\uparrow}[r', r''; \tilde{n}_\uparrow(r')]}{\delta n_\uparrow(r)} dr''. \tag{4.22}$$

Terms four through seven are two from $E_{\mathrm{xc}}^{\uparrow\downarrow}$:

$$v_4^\uparrow(r) = \frac{1}{2} \int \frac{n_\downarrow(r') G^{\uparrow\downarrow}[r, r'; \tilde{n}_\uparrow(r), \tilde{n}_\downarrow(r)]}{|r - r'|} dr', \tag{4.23}$$

$$v_5^\uparrow(r) = \frac{1}{2} \int n_\uparrow(r') dr' \int \frac{n_\downarrow(r'')}{|r' - r''|} \frac{\delta G^{\uparrow\downarrow}[r', r''; \tilde{n}_\uparrow(r'), \tilde{n}_\downarrow(r')]}{\delta n_\uparrow(r)} dr'', \tag{4.24}$$

and two from $E_{\mathrm{xc}}^{\downarrow\uparrow}$:

$$v_6^\uparrow(r) = \frac{1}{2} \int \frac{n_\downarrow(r') G^{\uparrow\downarrow}[r, r'; \tilde{n}_\uparrow(r'), \tilde{n}_\downarrow(r')]}{|r - r'|} dr', \tag{4.25}$$

$$v_7^\uparrow(r) = \frac{1}{2} \int n_\downarrow(r') dr' \int \frac{n_\uparrow(r'')}{|r' - r''|} \frac{\delta G^{\uparrow\downarrow}[r', r''; \tilde{n}_\uparrow(r'), \tilde{n}_\downarrow(r')]}{\delta n_\uparrow(r)} dr''. \tag{4.26}$$

The relations for $v_{\mathrm{xc}}^\downarrow$ are exactly the same except for all references to up ($\uparrow$) being replaced with down ($\downarrow$) and vice versa.

Our model pair-correlation functions have no explicit dependance on the electron density, only through the weighted up/down spin density parameters. Therefore, using the chain rule, we write:

$$\frac{\delta G^{\uparrow\uparrow}[r', r''; \tilde{n}_\uparrow(r')]}{\delta n_\uparrow(r)} = \frac{\partial G^{\uparrow\uparrow}[r', r''; \tilde{n}_\uparrow(r')]}{\partial \tilde{n}_\uparrow(r')} \times \frac{\delta \tilde{n}_\uparrow(r')}{\delta n_\uparrow(r)}, \tag{4.27}$$

with similar relations for the antiparallel model pair-correlation functions and derivatives with respect to the down ($\downarrow$) density. The functional derivative of the weighted up spin density with respect to the electron up spin density can be obtained by taking the functional derivative of the sum rule $\int n_\uparrow(r'')G^{\uparrow\uparrow}[r',r'';\tilde{n}_\uparrow(r')]dr'' = -1$:

$$\frac{\delta\tilde{n}_\uparrow(r')}{\delta n_\uparrow(r)} = \frac{-G^{\uparrow\uparrow}[r,r';\tilde{n}_\uparrow(r)]}{\int n_\uparrow(r'')\partial G^{\uparrow\uparrow}[r',r'';\tilde{n}_\uparrow(r')]/\partial\tilde{n}_\uparrow(r')dr''}. \tag{4.28}$$

We can then rearrange the third potential term to be:

$$v_3^\uparrow(r) = -\frac{1}{2}\int n(r')\frac{h_1^\uparrow(r')}{h_2^\uparrow(r')}G^{\uparrow\uparrow}[r,r';\tilde{n}_\uparrow(r)]dr', \tag{4.29}$$

where the h terms are given by:

$$h_1^\uparrow(r) = \int \frac{n_\uparrow(r')}{|r-r'|}\frac{\partial G^{\uparrow\uparrow}[r,r';\tilde{n}_\uparrow(r)]}{\partial\tilde{n}_\uparrow(r)}dr', \tag{4.30}$$

$$h_2^\uparrow(r) = \int n_\uparrow(r')\frac{\partial G^{\uparrow\uparrow}[r,r';\tilde{n}_\uparrow(r)]}{\partial\tilde{n}_\uparrow(r)}dr'. \tag{4.31}$$

Similarly, we can rearrange the fifth and seventh terms to be:

$$v_5^\uparrow(r) = -\frac{1}{2}\int n_\uparrow(r')\frac{h_1^{\uparrow\downarrow}(r')}{h_2^\uparrow(r')}G^{\uparrow\uparrow}[r,r';\tilde{n}_\uparrow(r)]dr', \tag{4.32}$$

$$v_7^\uparrow(r) = -\frac{1}{2}\int n_\downarrow(r')\frac{h_1^{\uparrow\uparrow}(r')}{h_2^\uparrow(r')}G^{\uparrow\uparrow}[r,r';\tilde{n}_\uparrow(r)]dr', \tag{4.33}$$

where $h_2^\uparrow$ is as above in equation 4.31 and:

$$h_1^{\uparrow\downarrow}(r) = \int \frac{n_\downarrow(r')}{|r - r'|} \frac{\partial G^{\uparrow\downarrow}[r, r'; \tilde{n}_\uparrow(r), \tilde{n}_\downarrow(r)]}{\partial \tilde{n}_\uparrow(r)} dr', \tag{4.34}$$

$$h_1^{\uparrow\uparrow}(r) = \int \frac{n_\uparrow(r')}{|r - r'|} \frac{\partial G^{\uparrow\downarrow}[r, r'; \tilde{n}_\uparrow(r), \tilde{n}_\downarrow(r)]}{\partial \tilde{n}_\uparrow(r)} dr'. \tag{4.35}$$

Once again, equations 4.27 through 4.35 can have all up ($\uparrow$) and down ($\downarrow$) references interchanged to give the relations required for $v_{xc}^\downarrow$. Note that the rewritten forms of the fifth and seventh terms in equations 4.32 and 4.33 contain the model pair-correlation function for like spins. This is because the weighted density, in our implementation, is determined from satisfying the sum rule for like spin pairs and therefore that sum rule must be used in calculating the functional derivative of the weighted density with respect to the electron density in all cases.

4.3 Implementation

As with the WDA, we use the sum rule to determine the weighted density and fit our model pair-correlation function such that the known exact energy in the homogeneous limit is obtained. The differences come in when obtaining the spin resolved weighted density. Our approach will be to determine the weighted up/down density from the sum rule for the parallel spin parts of the exchange-correlation hole. This will be done in the same way as the WDA, as discussed in Chapter 2, generating a logarithmic lookup table for each of the up and down weighted densities, followed by a search through the table for a value that (nearly) fulfills the sum rule at each point in space. We then interpolate to find value that satisfies the sum rule to computational accuracy. These weighted spin density parameters will then be used in the model pair-correlation function for antiparallel spins, which will be fitted to return the LSDA energy in the homogeneous limit.

The equations for the exchange-correlation energy and potential in the previous section are in the form of convolutions. These can be evaluated with relative ease in reciprocal space, rather than performing expensive real space integrals. We will derive explicit forms for the integrals in reciprocal space below.

4.3.1 Parallel Spins

First, we should choose a model pair-correlation function. A functional form that satisfies the cusp conditions in equations 4.9, 4.11 and 4.12 can be chosen in analogy to the cusp condition satisfying model derived in Chapter 2. Given the starting point of a Gaussian model pair-correlation function, a second term can be introduced to alter the short range behaviour of the function:

$$G^{\sigma\sigma}[\boldsymbol{r}, \boldsymbol{r}'; \tilde{n}_\sigma(\boldsymbol{r})] = -e^{-\left(\frac{|\boldsymbol{r}-\boldsymbol{r}'|}{\lambda(\tilde{n}_\sigma(\boldsymbol{r}))}\right)^2} + \frac{|\boldsymbol{r}-\boldsymbol{r}'|^3}{2\lambda^2(\tilde{n}_\sigma(\boldsymbol{r}))} e^{-\left(\frac{|\boldsymbol{r}-\boldsymbol{r}'|}{\kappa(\tilde{n}_\sigma(\boldsymbol{r}))\lambda(\tilde{n}_\sigma(\boldsymbol{r}))}\right)^2}, \qquad (4.36)$$

where λ and κ are determined from the sum rule and the spin resolved LSDA energy in the homogeneous limit. However, if this were followed through, a 15th order polynomial in λ would have to be solved. The coefficients of this are badly conditioned to the point that numerical solutions are not feasible. For now we will relax the constraint of equation 4.12 while retaining those of equations 4.9 and 4.11 so that a more simple model functional can be used:

$$G^{\sigma\sigma}[\boldsymbol{r}, \boldsymbol{r}'; \tilde{n}_\sigma(\boldsymbol{r})] = -e^{-\left(\frac{|\boldsymbol{r}-\boldsymbol{r}'|}{\lambda(\tilde{n}_\sigma(\boldsymbol{r}))}\right)^2} = -e^{-u^2}, \qquad (4.37)$$

where $u = |\boldsymbol{r} - \boldsymbol{r}'|/\lambda$ and we will refer to the model pair-correlation function as a simple product of the form $Cf(u)$, with $C = -1$ and $f(u) = e^{-u^2}$. Here, we will determine λ to satisfy the sum rule in the homogeneous limit and enforce the LSDA energy in the homogeneous limit by using the energy due to antiparallel spin pairs to make up the difference. This is not a unique method of calculating a value for λ – one could also use the known spin resolved exchange-correlation energy in the uniform limit, but this would no longer give the correct sum rule in this limit. The use of this functional form is only intended as a first, proof of concept, test. Referring to a general $f(u)$ allows us to use different model functions while using the same framework. We will discuss refinements to the model later.

In real space, the exchange-correlation energy density for parallel spins, following

from equation 4.17, is:

$$\varepsilon_{\mathrm{xc}}^{\sigma\sigma}(\boldsymbol{r}) = \frac{1}{2} \int n_\sigma(\boldsymbol{r}') \frac{G^{\sigma\sigma}[|\boldsymbol{r} - \boldsymbol{r}'|; \tilde{n}_\sigma(\boldsymbol{r})]}{|\boldsymbol{r} - \boldsymbol{r}'|} d\boldsymbol{r}'. \tag{4.38}$$

We can write this in an easily calculable form by inspection of equation 2.31:

$$\varepsilon_{\mathrm{xc}}^{\sigma\sigma}(\boldsymbol{r}) = 2\pi C \lambda^2 (\tilde{n}_\sigma(\boldsymbol{r})) \sum_{\boldsymbol{G}} \bar{n}_\sigma(\boldsymbol{G}) e^{i\boldsymbol{G}\cdot\boldsymbol{r}} F_1(q), \tag{4.39}$$

where $\boldsymbol{G}$ are the reciprocal lattice vectors, $\bar{n}_\sigma(\boldsymbol{G})$ is the Fourier transform of the electron density with spin σ, and we have the spherical Fourier transform of the model pair-correlation function over the pair separation:

$$F_1(q) = \frac{1}{q} \int_0^\infty f(u) \sin(qu) du, \tag{4.40}$$

and $q = |\boldsymbol{G}| \lambda(\tilde{n}_\sigma(\boldsymbol{r}))$.

The sum rule, from equation 4.7 is:

$$-1 = \int n_\sigma(\boldsymbol{r}') G^{\sigma\sigma}[|\boldsymbol{r} - \boldsymbol{r}'|; \tilde{n}_\sigma(\boldsymbol{r})] d\boldsymbol{r}'. \tag{4.41}$$

This can easily be rewritten from inspection of the sum rule in our original WDA formulation, equation 2.36, giving:

$$-1 = 4\pi C \lambda^3 (\tilde{n}_\sigma(\boldsymbol{r})) \sum_{\boldsymbol{G}} \bar{n}_\sigma(\boldsymbol{G}) e^{i\boldsymbol{G}\cdot\boldsymbol{r}} F_2(q), \tag{4.42}$$

where we have $F_2(q)$, the spherical Fourier transform of the model pair-correlation function defined as:

$$F_2(q) = \frac{1}{q} \int_0^\infty u f(u) \sin(qu) du. \tag{4.43}$$

The parameter λ can be determined by taking equation 4.42 in the homogeneous limit, setting $\bar{n}$ to $\tilde{n}$, giving:

$$-1 = 4\pi C \left(\lambda^3(\tilde{n}_\sigma(\mathbf{r})) \right) \tilde{n}_\sigma(\mathbf{r}) F_2(0), \tag{4.44}$$

where the weighted density becomes the electron density and $q \to 0$, so we have:

$$F_2(0) = \int_0^\infty u^2 f(u) du = \int_0^\infty u^2 e^{-u^2} du = \frac{\sqrt{\pi}}{4}, \tag{4.45}$$

for our choice of a Gaussian model pair-correlation function. We can then rearrange equation 4.44 for λ, remembering that $C = -1$, finally resulting in:

$$\lambda(\tilde{n}_\sigma(\mathbf{r})) = \left(\frac{1}{\pi\sqrt{\pi}\tilde{n}_\sigma(\mathbf{r})} \right)^{\frac{1}{3}}. \tag{4.46}$$

For later reference, we will also give the homogeneous exchange-correlation energy density due to parallel spin electrons when using the Gaussian model pair-correlation function. Taking equation 4.39 in the uniform limit:

$$\frac{n_\sigma(\mathbf{r})}{n(\mathbf{r})} \varepsilon_{\mathrm{xc}}^{\sigma\sigma}(\mathbf{r}) \bigg|_{unif} = 2\pi C \lambda^2(\tilde{n}_\sigma(\mathbf{r})) \frac{\tilde{n}_\sigma^2(\mathbf{r})}{\tilde{n}(\mathbf{r})} F_1(0) = -\frac{\tilde{n}_\sigma(\mathbf{r})^{\frac{4}{3}}}{\tilde{n}(\mathbf{r})}, \tag{4.47}$$

as the spherical Fourier transform of the model pair-correlation function over the separation, in the uniform limit is:

$$F_1(0) = \int_0^\infty u f(u) du = \int_0^\infty u e^{-u^2} du = \frac{1}{2}. \tag{4.48}$$

Our potential terms are rewritten in analogous fashion to the WDA. Once again, in the same way as the first potential term given in equation 2.13 in our original WDA formulation in Chapter 2, our first potential term reduces to the exchange-correlation energy for parallel spins:

$$v_1^\sigma(\mathbf{r}) = \varepsilon_{\mathrm{xc}}^{\sigma\sigma}(\mathbf{r}). \tag{4.49}$$

The second and third potential terms are to be calculated in reciprocal space and Fourier transformed back to real space. The Fourier components, $\bar{v}_2^\sigma(\mathbf{G})$ of $v_2^\sigma(\mathbf{r})$ are obtained using the convolution theorem on equation 4.21:

$$\bar{v}_2^\sigma(\mathbf{G}) = \frac{2\pi}{\Omega} \int n_\sigma(\mathbf{r}')\lambda^2(\tilde{n}_\sigma(\mathbf{r}'))e^{-i\mathbf{G}\cdot\mathbf{r}'}F_1(q)d\mathbf{r}', \tag{4.50}$$

where Ω is the cell volume. Similarly, the Fourier components, $\bar{v}_3^\sigma(\mathbf{G})$ of $v_3^\sigma(\mathbf{r})$ can be found using the convolution theorem on equation 4.29:

$$\bar{v}_3^\sigma(\mathbf{G}) = -\frac{2\pi}{\Omega} \int n_\sigma(\mathbf{r}')\frac{h_1^\sigma(\mathbf{r}')}{h_2^\sigma(\mathbf{r}')}\lambda^3(\tilde{n}_\sigma(\mathbf{r}'))e^{-i\mathbf{G}\cdot\mathbf{r}'}F_2(q)d\mathbf{r}'. \tag{4.51}$$

The h terms from equations 4.30 and 4.31 are also in the form of convolutions. First, we need to rewrite the derivative of the model pair-correlation function because there is no explicit dependance on the weighted density (or the λ parameter):

$$\frac{\partial G^{\sigma\sigma}[u,\tilde{n}_\sigma(\mathbf{r})]}{\partial\tilde{n}_\sigma(\mathbf{r})} = \frac{\partial u}{\partial\lambda(\tilde{n}_\sigma(\mathbf{r}))}\frac{\partial G^{\sigma\sigma}[u,\tilde{n}_\sigma(\mathbf{r})]}{\partial u}\frac{\partial\lambda(\tilde{n}_\sigma(\mathbf{r}))}{\partial\tilde{n}_\sigma(\mathbf{r})} \tag{4.52}$$

$$= -\frac{u}{\lambda(\tilde{n}_\sigma(\mathbf{r}))}C\frac{\partial f(u)}{\partial u}\frac{\partial\lambda(\tilde{n}_\sigma(\mathbf{r}))}{\partial\tilde{n}_\sigma(\mathbf{r})}. \tag{4.53}$$

We can then write the h functions as:

$$h_1^\sigma(r) = -\int \frac{n_\sigma(r')}{\lambda^2(\tilde{n}_\sigma(r))} C \frac{\partial f(u)}{\partial u} \frac{\partial \lambda(\tilde{n}_\sigma(r))}{\partial \tilde{n}_\sigma(r)} dr', \tag{4.54}$$

$$h_2^\sigma(r) = -\int \frac{n_\sigma(r')}{\lambda(\tilde{n}_\sigma(r))} C u \frac{\partial f(u)}{\partial u} \frac{\partial \lambda(\tilde{n}_\sigma(r))}{\partial \tilde{n}_\sigma(r)} dr'. \tag{4.55}$$

Using the convolution theorem we can write the above equations in an easily calculable form:

$$h_1^\sigma(r) = -4\pi C \lambda(\tilde{n}_\sigma(r)) \frac{\partial \lambda(\tilde{n}_\sigma(r))}{\partial \tilde{n}_\sigma(r)} \sum_G \bar{n}_\sigma(G) e^{iG\cdot r} F_3(q), \tag{4.56}$$

$$h_2^\sigma(r) = -4\pi C \lambda^2(\tilde{n}_\sigma(r)) \frac{\partial \lambda(\tilde{n}_\sigma(r))}{\partial \tilde{n}_\sigma(r)} \sum_G \bar{n}_\sigma(G) e^{iG\cdot r} F_4(q), \tag{4.57}$$

where we have functions that are related to spherical Fourier transforms of the derivative of the model pair-correlation function with respect to u:

$$F_3(q) = \frac{1}{q} \int_0^\infty u \frac{\partial f(u)}{\partial u} \sin(qu) du, \tag{4.58}$$

$$F_4(q) = \frac{1}{q} \int_0^\infty u^2 \frac{\partial f(u)}{\partial u} \sin(qu) du, \tag{4.59}$$

and we note that $F_3(0) = -1$ and $F_4(0) = -\frac{3}{4}\sqrt{\pi}$, when using our current model pair-correlation function $f(u) = e^{u^2}$. In our potential term, we require the ratio $h_1^\sigma(r)/h_2^\sigma(r)$. Much of equations 4.56 and 4.57 then cancel each other out so we can write:

$$\frac{h_1^\sigma(r)}{h_2^\sigma(r)} = \frac{\sum_G \bar{n}_\sigma(G) e^{iG\cdot r} F_3(q)}{\lambda(\tilde{n}_\sigma(r)) \sum_G \bar{n}_\sigma(G) e^{iG\cdot r} F_4(q)}. \tag{4.60}$$

The derivative of the λ parameter is required later in the calculations of the potential terms due to antiparallel spins:

$$\frac{\partial \lambda(\tilde{n}_\sigma(\boldsymbol{r}))}{\partial \tilde{n}_\sigma(\boldsymbol{r})} = -\frac{1}{3} \left(\frac{1}{\pi \sqrt{\pi} \tilde{n}_\sigma^4(\boldsymbol{r})} \right)^{\frac{1}{3}} \tag{4.61}$$

4.3.2 Antiparallel Spins

For the case of antiparallel spins, we will use a model pair-correlation function similar to our cusp condition modified WDA from Chapter 2, equation 2.69. To recap, the model function is set up to have two parts, where the second part modifies the short range behaviour of the function to satisfy the cusp condition. Namely, that the on-top value of the pair-correlation function is equal in value to its derivative with respect to pair separation, evaluated at zero separation, equation 4.13. The difference in this case is that the sum rule for antiparallel spins is zero. For this to be possible, our model pair correlation function must be greater than zero in some places so that the sum rule can be satisfied. A relatively simple way of doing this is to have a model function as follows:

$$\begin{aligned}
G^{\uparrow\downarrow}[\boldsymbol{r}, \boldsymbol{r}'; \tilde{n}_\uparrow, \tilde{n}_\downarrow] &= C(\tilde{n}_\uparrow, \tilde{n}_\downarrow) e^{-\left(\frac{|\boldsymbol{r}-\boldsymbol{r}'|}{\lambda(\tilde{n}_\uparrow, \tilde{n}_\downarrow)} \right)^2} \\
&+ (C(\tilde{n}_\uparrow, \tilde{n}_\downarrow) + 1) \left(|\boldsymbol{r} - \boldsymbol{r}'| + \frac{|\boldsymbol{r} - \boldsymbol{r}'|^2}{\lambda(\tilde{n}_\uparrow, \tilde{n}_\downarrow)} \right) e^{-\left(\frac{|\boldsymbol{r}-\boldsymbol{r}'|}{\kappa\lambda(\tilde{n}_\uparrow, \tilde{n}_\downarrow)} \right)^2},
\end{aligned} \tag{4.62}$$

where we omit the explicit $\boldsymbol{r}$ dependance of the weighted density. The parameters C and λ now depend on both the weighted up and down spin densities. The constant κ is chosen to fit the on top value to the known homogeneous value at a range of electron densities, such as references [83, 84, 85, 86]. We will discuss in detail on-top

values in the homogeneous limit and the selection of κ in Chapter 5. If we substitute $u = |r - r'|/\lambda$ we can rewrite this model function as:

$$G^{\uparrow\downarrow}[u; \tilde{n}_\uparrow, \tilde{n}_\downarrow] = C(\tilde{n}_\uparrow, \tilde{n}_\downarrow)e^{-u^2} + (C(\tilde{n}_\uparrow, \tilde{n}_\downarrow) + 1)\lambda(\tilde{n}_\uparrow, \tilde{n}_\downarrow)(u + u^2)e^{-\frac{u^2}{\kappa^2}}. \quad (4.63)$$

To make the following framework more general, we can replace the u dependent parts with f functions:

$$G^{\uparrow\downarrow}[u; \tilde{n}_\uparrow, \tilde{n}_\downarrow] = C(\tilde{n}_\uparrow, \tilde{n}_\downarrow)f^a(u) + (C(\tilde{n}_\uparrow, \tilde{n}_\downarrow) + 1)\lambda(\tilde{n}_\uparrow, \tilde{n}_\downarrow)f^b(u), \quad (4.64)$$

where f^a and f^b can be replaced by appropriate functions.

Following from equation 4.17, the exchange-correlation energy in real space for antiparallel spins is:

$$\varepsilon_{xc}^{\uparrow\downarrow}(r) = \frac{1}{2}\int n_\downarrow(r')\frac{G^{\uparrow\downarrow}[|r - r'|; \tilde{n}_\uparrow(r), \tilde{n}_\downarrow(r)]}{|r - r'|}dr', \quad (4.65)$$

and we also have:

$$\varepsilon_{xc}^{\downarrow\uparrow}(r) = \frac{1}{2}\int n_\uparrow(r')\frac{G^{\uparrow\downarrow}[|r - r'|; \tilde{n}_\uparrow(r), \tilde{n}_\downarrow(r)]}{|r - r'|}dr', \quad (4.66)$$

where we use the same model pair-correlation function whether we are looking at up-down or down-up spin pairs. These integrals are once again in the form of convolutions, a fact that we can use to rewrite them in an easily calculable form, thus:

$$\varepsilon_{xc}^{\uparrow\downarrow}(r) = 2\pi C(\tilde{n}_\uparrow, \tilde{n}_\downarrow)\lambda^2(\tilde{n}_\uparrow, \tilde{n}_\downarrow)\sum_G \bar{n}_\downarrow(G)e^{iG\cdot r}H_1^{\uparrow\downarrow}(q), \quad (4.67)$$

$$\varepsilon_{xc}^{\downarrow\uparrow}(r) = 2\pi C(\tilde{n}_\uparrow, \tilde{n}_\downarrow)\lambda^2(\tilde{n}_\uparrow, \tilde{n}_\downarrow)\sum_G \bar{n}_\uparrow(G)e^{iG\cdot r}H_1^{\uparrow\downarrow}(q), \quad (4.68)$$

where we introduce the term $H_1^{\uparrow\downarrow}$ to simplify the spherical Fourier transforms of our model functions. Here $q = |G|\lambda(\tilde{n}_\uparrow(r), \tilde{n}_\downarrow(r))$ and:

$$H_1^{\uparrow\downarrow}(q) = F_1^a(q) + \left(1 + \frac{1}{C(\tilde{n}_\uparrow, \tilde{n}_\downarrow)}\right) \lambda(\tilde{n}_\uparrow, \tilde{n}_\downarrow) F_1^b(q). \tag{4.69}$$

The F_1 functions are related to the spherical Fourier transforms thus:

$$F_1^a(q) = \frac{1}{q} \int_0^\infty f^a(u) \sin(qu)\, du, \tag{4.70}$$

$$F_1^b(q) = \frac{1}{q} \int_0^\infty f^b(u) \sin(qu)\, du. \tag{4.71}$$

The sum rules in this case, from equation 4.7 are:

$$0 = 4\pi C(\tilde{n}_\uparrow, \tilde{n}_\downarrow)\lambda^3(\tilde{n}_\uparrow, \tilde{n}_\downarrow) \sum_G \bar{n}_\uparrow(G) e^{iG \cdot r} H_2^{\uparrow\downarrow}(q), \tag{4.72}$$

$$0 = 4\pi C(\tilde{n}_\uparrow, \tilde{n}_\downarrow)\lambda^3(\tilde{n}_\uparrow, \tilde{n}_\downarrow) \sum_G \bar{n}_\downarrow(G) e^{iG \cdot r} H_2^{\uparrow\downarrow}(q), \tag{4.73}$$

where we introduce $H_2^{\uparrow\downarrow}$ (which is similar to $H_1^{\uparrow\downarrow}$):

$$H_2^{\uparrow\downarrow}(q) = F_2^a(q) + \left(1 + \frac{1}{C(\tilde{n}_\uparrow, \tilde{n}_\downarrow)}\right) \lambda(\tilde{n}_\uparrow, \tilde{n}_\downarrow) F_2^b(q). \tag{4.74}$$

We also have the F_2 functions that come from the spherical Fourier transform of the model pair-correlation function:

$$F_2^a(q) = \frac{1}{q} \int_0^\infty u f^a(u) \sin(qu)\, du, \tag{4.75}$$

$$F_2^b(q) = \frac{1}{q} \int_0^\infty u f^b(u) \sin(qu)\, du. \tag{4.76}$$

If we take the sum rules in the uniform limit, we get:

$$0 = C(\tilde{n}_\uparrow, \tilde{n}_\downarrow)\lambda^3(\tilde{n}_\uparrow, \tilde{n}_\downarrow)\tilde{n}_\uparrow \left[I_2^a + \left(1 + \frac{1}{C(\tilde{n}_\uparrow, \tilde{n}_\downarrow)} \right) \lambda(\tilde{n}_\uparrow, \tilde{n}_\downarrow)I_2^b \right], \qquad (4.77)$$

where $I_2^a = 4\pi F_2^a(0)$ and $I_2^b = 4\pi F_2^b(0)$. This leads to the same result for both sum rules, relating the C and λ parameters, thus:

$$C(\tilde{n}_\uparrow, \tilde{n}_\downarrow) = -\frac{\lambda(\tilde{n}_\uparrow, \tilde{n}_\downarrow)I_2^b}{I_2^a + \lambda(\tilde{n}_\uparrow, \tilde{n}_\downarrow)I_2^b}. \qquad (4.78)$$

To determine λ, we take the homogeneous limit of the exchange-correlation energy density due to antiparallel spin pairs from equation 4.17 and the uniform limit of equations 4.67 and 4.68:

$$\left(\frac{n_\uparrow(r)}{n(r)}\varepsilon_{xc}^{\uparrow\downarrow}(r) + \frac{n_\downarrow(r)}{n(r)}\varepsilon_{xc}^{\downarrow\uparrow}(r) \right)\bigg|_{unif} = C(\tilde{n}_\uparrow, \tilde{n}_\downarrow)\lambda^2(\tilde{n}_\uparrow, \tilde{n}_\downarrow)\left(\frac{\tilde{n}_\uparrow \tilde{n}_\downarrow}{\tilde{n}} \right)H_1^{\uparrow\downarrow}(0), \quad (4.79)$$

where $H_1^{\uparrow\downarrow}(0)$ can be written as:

$$H_1^{\uparrow\downarrow}(0) = I_1^a + \left(1 + \frac{1}{C(\tilde{n}_\uparrow, \tilde{n}_\downarrow)} \right) \lambda(\tilde{n}_\uparrow, \tilde{n}_\downarrow)I_1^b, \qquad (4.80)$$

and $I_1^a = 4\pi F_1^a(0)$ and $I_1^b = 4\pi F_1^b(0)$. We then equate the uniform limit of the WSDA exchange-correlation energy density to the LSDA energy density:

$$\varepsilon_{xc}^{LSDA}[\tilde{n}_\uparrow, \tilde{n}_\downarrow] = -\frac{\tilde{n}_\uparrow^{\frac{4}{3}} + \tilde{n}_\downarrow^{\frac{4}{3}}}{\tilde{n}} + C(\tilde{n}_\uparrow, \tilde{n}_\downarrow)\lambda^2(\tilde{n}_\uparrow, \tilde{n}_\downarrow)\left(\frac{\tilde{n}_\uparrow \tilde{n}_\downarrow}{\tilde{n}} \right)H_1^{\uparrow\downarrow}(0), \qquad (4.81)$$

where the exchange-correlation energy density due to parallel spins is used in the

case of using a Gaussian for the model pair correlation function, as given in equation 4.47. We can then substitute back in for C from equation 4.78 and rearrange to get a cubic polynomial in λ:

$$a_3\lambda^3(\tilde{n}_\uparrow, \tilde{n}_\downarrow) + a_1\lambda(\tilde{n}_\uparrow, \tilde{n}_\downarrow) + a_0 = 0, \tag{4.82}$$

where the coefficients are given by:

$$a_3 = \frac{\tilde{n}_\uparrow \tilde{n}_\downarrow}{\tilde{n}} \left(I_1^a I_2^b - I_1^b I_2^a \right), \tag{4.83}$$

$$a_1 = \left(\varepsilon_{\mathrm{xc}}^{\mathrm{LSDA}}[\tilde{n}_\uparrow, \tilde{n}_\downarrow] + \frac{\tilde{n}_\uparrow^{\frac{4}{3}} + \tilde{n}_\downarrow^{\frac{4}{3}}}{\tilde{n}} \right) I_2^b, \tag{4.84}$$

$$a_0 = \left(\varepsilon_{\mathrm{xc}}^{\mathrm{LSDA}}[\tilde{n}_\uparrow, \tilde{n}_\downarrow] + \frac{\tilde{n}_\uparrow^{\frac{4}{3}} + \tilde{n}_\downarrow^{\frac{4}{3}}}{\tilde{n}} \right) I_2^a. \tag{4.85}$$

The roots of this equation can be found numerically using an appropriate method such as finding the eigenvalues of a companion matrix as described in section 2.4.1. Positive real roots of λ should be chosen as it controls the range of the model pair-correlation function and also in order to keep C in the allowed range for the on-top value of the pair-correlation function.

The fourth potential term is simply related to the exchange-correlation energy density for antiparallel spin pairs, in analogy with equation 2.13, where $v_4^\uparrow(r) = \varepsilon_{\mathrm{xc}}^{\uparrow\downarrow}(r)$ and $v_4^\downarrow(r) = \varepsilon_{\mathrm{xc}}^{\downarrow\uparrow}(r)$. The Fourier components of the sixth potential term come from using the convolution theorem on equation 4.25:

$$\bar{v}_6^\uparrow(G) = \frac{2\pi}{\Omega} \int n_\downarrow(r')C(\tilde{n}_\uparrow(r'), \tilde{n}_\downarrow(r'))\lambda^2(\tilde{n}_\uparrow(r'), \tilde{n}_\downarrow(r'))e^{-iG\cdot r'}H_1^{\uparrow\downarrow}(q)dr', \tag{4.86}$$

$$\bar{v}_6^\downarrow(G) = \frac{2\pi}{\Omega} \int n_\uparrow(r')C(\tilde{n}_\uparrow(r'), \tilde{n}_\downarrow(r'))\lambda^2(\tilde{n}_\uparrow(r'), \tilde{n}_\downarrow(r'))e^{-iG\cdot r'}H_1^{\uparrow\downarrow}(q)dr'. \tag{4.87}$$

The Fourier coefficients of the fifth and seventh potential terms are determined by applying the convolution theorem to equations 4.32 and 4.33, giving:

$$\bar{v}_5^\uparrow(G) = -\frac{2\pi}{\Omega} \int n_\uparrow(r') \frac{h_1^{\uparrow\downarrow}(r')}{h_2^\uparrow(r')} C\lambda^3(\tilde{n}_\uparrow(r'))e^{-iG\cdot r'} F_2(q_\uparrow)dr', \tag{4.88}$$

$$\bar{v}_5^\downarrow(G) = -\frac{2\pi}{\Omega} \int n_\downarrow(r') \frac{h_1^{\downarrow\uparrow}(r')}{h_2^\downarrow(r')} C\lambda^3(\tilde{n}_\downarrow(r'))e^{-iG\cdot r'} F_2(q_\downarrow)dr', \tag{4.89}$$

$$\bar{v}_7^\uparrow(G) = -\frac{2\pi}{\Omega} \int n_\downarrow(r') \frac{h_1^{\uparrow\uparrow}(r')}{h_2^\uparrow(r')} C\lambda^3(\tilde{n}_\uparrow(r'))e^{-iG\cdot r'} F_2(q_\uparrow)dr', \tag{4.90}$$

$$\bar{v}_7^\downarrow(G) = -\frac{2\pi}{\Omega} \int n_\uparrow(r') \frac{h_1^{\downarrow\downarrow}(r')}{h_2^\downarrow(r')} C\lambda^3(\tilde{n}_\downarrow(r'))e^{-iG\cdot r'} F_2(q_\downarrow)dr'. \tag{4.91}$$

Note that C and λ in the four above equations are those used in the parallel spins calculation and $F_2(q_\sigma)$ is the spherical Fourier transform of the the model pair-correlation function for parallel spin pairs σ, where $q_\sigma = |G|\lambda(\tilde{n}_\sigma(r))$ indicates that we are using λ from the parallel spins calculation. The h_2^σ functions are given in equation 4.57.

The h_1 functions from equations 4.34 and 4.35 are also in the form of convolutions. Again, we must use the chain rule to rewrite the derivative of the model pair-correlation function with respect to the weighted density:

$$\frac{\partial G^{\uparrow\downarrow}[u, \tilde{n}_\uparrow, \tilde{n}_\downarrow]}{\partial \tilde{n}_\uparrow(r)} = \frac{\partial G^{\uparrow\downarrow}[u, \tilde{n}_\uparrow, \tilde{n}_\downarrow]}{\partial C(\tilde{n}_\uparrow(r), \tilde{n}_\downarrow(r))} \frac{\partial C(\tilde{n}_\uparrow(r), \tilde{n}_\downarrow(r))}{\partial \tilde{n}_\uparrow(r)}$$

$$+ \frac{\partial G^{\uparrow\downarrow}[u, \tilde{n}_\uparrow, \tilde{n}_\downarrow]}{\partial \lambda(\tilde{n}_\uparrow(r), \tilde{n}_\downarrow(r))} \frac{\partial \lambda(\tilde{n}_\uparrow(r), \tilde{n}_\downarrow(r))}{\partial \tilde{n}_\uparrow(r)} + \frac{\partial G^{\uparrow\downarrow}[u, \tilde{n}_\uparrow, \tilde{n}_\downarrow]}{\partial u} \frac{\partial u}{\partial \tilde{n}_\uparrow(r)}. \tag{4.92}$$

Using this and the convolution theorem, we can then write $h_1^{\uparrow\downarrow}$ as:

$$h_1^{\uparrow\downarrow}(\boldsymbol{r}) \;=\; 4\pi\lambda(\tilde{n}_\uparrow,\tilde{n}_\downarrow)\sum_{\boldsymbol{G}} \bar{n}_\downarrow(\boldsymbol{G})e^{i\boldsymbol{G}\cdot\boldsymbol{r}} \times$$

$$\left[\lambda(\tilde{n}_\uparrow,\tilde{n}_\downarrow)\frac{\partial C(\tilde{n}_\uparrow,\tilde{n}_\downarrow)}{\partial\tilde{n}_\uparrow}\left(F_1^a(q) + \lambda(\tilde{n}_\uparrow,\tilde{n}_\downarrow)F_1^b(q)\right)\right.$$

$$\left. +\; (C(\tilde{n}_\uparrow,\tilde{n}_\downarrow) + 1)\lambda(\tilde{n}_\uparrow,\tilde{n}_\downarrow)\frac{\partial\lambda(\tilde{n}_\uparrow,\tilde{n}_\downarrow)}{\partial\tilde{n}_\uparrow}F_1^b(q) - C(\tilde{n}_\uparrow,\tilde{n}_\downarrow)\frac{\partial\lambda(\tilde{n}_\uparrow,\tilde{n}_\downarrow)}{\partial\tilde{n}_\uparrow}H_3(q)\right],$$

$$(4.93)$$

where we introduce $H_3^{\uparrow\downarrow}$, which is similar to our previous $H^{\uparrow\downarrow}$ functions (equations 4.69 and 4.74):

$$H_3^{\uparrow\downarrow}(q) = F_3^a(q) + \left(1 + \frac{1}{C(\tilde{n}_\uparrow,\tilde{n}_\downarrow)}\right)\lambda(\tilde{n}_\uparrow,\tilde{n}_\downarrow)F_3^b(q). \qquad (4.94)$$

We also have functions related to the spherical Fourier transform of the derivative of the model pair-correlation function with respect to u:

$$F_3^a(q) \;=\; \frac{1}{q}\int_0^\infty u\frac{df^a(u)}{du}\sin(qu)\,du, \qquad (4.95)$$

$$F_3^b(q) \;=\; \frac{1}{q}\int_0^\infty u\frac{df^b(u)}{du}\sin(qu)\,du. \qquad (4.96)$$

Upon inspection of equation 4.93, we can rewrite it to use the already known exchange-correlation energy density for antiparallel spins, from equation 4.67:

$$
\begin{aligned}
h_1^{\uparrow\downarrow}(\boldsymbol{r}) \;=\;& \frac{2\varepsilon_{\text{xc}}^{\uparrow\downarrow}(\boldsymbol{r})}{C(\tilde{n}_\uparrow(\boldsymbol{r}),\tilde{n}_\downarrow(\boldsymbol{r}))}\,\frac{\partial C(\tilde{n}_\uparrow(\boldsymbol{r}),\tilde{n}_\downarrow(\boldsymbol{r}))}{\partial\tilde{n}_\uparrow(\boldsymbol{r})} + 4\pi\sum_{\boldsymbol{G}}\bar{n}_\downarrow(\boldsymbol{G})e^{i\boldsymbol{G}\cdot\boldsymbol{r}} \\[2mm]
&\times\; \Bigg[(C(\tilde{n}_\uparrow(\boldsymbol{r}),\tilde{n}_\downarrow(\boldsymbol{r}))+1)\lambda^2(\tilde{n}_\uparrow(\boldsymbol{r}),\tilde{n}_\downarrow(\boldsymbol{r}))\frac{\partial\lambda(\tilde{n}_\uparrow(\boldsymbol{r}),\tilde{n}_\downarrow(\boldsymbol{r}))}{\partial\tilde{n}_\uparrow(\boldsymbol{r})}F_1^b(q) \\[2mm]
&\quad -\frac{\lambda^3(\tilde{n}_\uparrow(\boldsymbol{r}),\tilde{n}_\downarrow(\boldsymbol{r}))}{C(\tilde{n}_\uparrow(\boldsymbol{r}),\tilde{n}_\downarrow(\boldsymbol{r}))}\frac{\partial C(\tilde{n}_\uparrow(\boldsymbol{r}),\tilde{n}_\downarrow(\boldsymbol{r}))}{\partial\tilde{n}_\uparrow(\boldsymbol{r})}F_1^b(q) \\[2mm]
&\quad -C(\tilde{n}_\uparrow(\boldsymbol{r}),\tilde{n}_\downarrow(\boldsymbol{r}))\lambda(\tilde{n}_\uparrow(\boldsymbol{r}),\tilde{n}_\downarrow(\boldsymbol{r}))\frac{\partial\lambda(\tilde{n}_\uparrow(\boldsymbol{r}),\tilde{n}_\downarrow(\boldsymbol{r}))}{\partial\tilde{n}_\uparrow(\boldsymbol{r})}H_3^{\uparrow\downarrow}(q)\Bigg]. \quad (4.97)
\end{aligned}
$$

The first two terms in the square brackets cancel each other out if we take into account the relationship between C, λ and their derivatives, which we will give later. We can therefore simplify $h_1^{\uparrow\downarrow}$ to be:

$$
\begin{aligned}
h_1^{\uparrow\downarrow}(\boldsymbol{r}) \;=\;& \frac{2\varepsilon_{\text{xc}}^{\uparrow\downarrow}(\boldsymbol{r})}{C(\tilde{n}_\uparrow(\boldsymbol{r}),\tilde{n}_\downarrow(\boldsymbol{r}))}\,\frac{\partial C(\tilde{n}_\uparrow(\boldsymbol{r}),\tilde{n}_\downarrow(\boldsymbol{r}))}{\partial\tilde{n}_\uparrow(\boldsymbol{r})} + 4\pi\sum_{\boldsymbol{G}}\bar{n}_\downarrow(\boldsymbol{G})e^{i\boldsymbol{G}\cdot\boldsymbol{r}} \\[2mm]
&\times\; \Bigg[-C(\tilde{n}_\uparrow(\boldsymbol{r}),\tilde{n}_\downarrow(\boldsymbol{r}))\lambda(\tilde{n}_\uparrow(\boldsymbol{r}),\tilde{n}_\downarrow(\boldsymbol{r}))\frac{\partial\lambda(\tilde{n}_\uparrow(\boldsymbol{r}),\tilde{n}_\downarrow(\boldsymbol{r}))}{\partial\tilde{n}_\uparrow(\boldsymbol{r})}H_3^{\uparrow\downarrow}(q)\Bigg]. \quad (4.98)
\end{aligned}
$$

In the same way, we can construct $h_1^{\uparrow\uparrow}$ in a similar simplified form, thus:

$$
\begin{aligned}
h_1^{\uparrow\uparrow}(\boldsymbol{r}) \;=\;& \frac{2\varepsilon_{\text{xc}}^{\downarrow\uparrow}(\boldsymbol{r})}{C(\tilde{n}_\uparrow(\boldsymbol{r}),\tilde{n}_\downarrow(\boldsymbol{r}))}\,\frac{\partial C(\tilde{n}_\uparrow(\boldsymbol{r}),\tilde{n}_\downarrow(\boldsymbol{r}))}{\partial\tilde{n}_\uparrow(\boldsymbol{r})} + 4\pi\sum_{\boldsymbol{G}}\bar{n}_\uparrow(\boldsymbol{G})e^{i\boldsymbol{G}\cdot\boldsymbol{r}} \\[2mm]
&\times\; \Bigg[-C(\tilde{n}_\uparrow(\boldsymbol{r}),\tilde{n}_\downarrow(\boldsymbol{r}))\lambda(\tilde{n}_\uparrow(\boldsymbol{r}),\tilde{n}_\downarrow(\boldsymbol{r}))\frac{\partial\lambda(\tilde{n}_\uparrow(\boldsymbol{r}),\tilde{n}_\downarrow(\boldsymbol{r}))}{\partial\tilde{n}_\uparrow(\boldsymbol{r})}H_3^{\uparrow\downarrow}(q)\Bigg]. \quad (4.99)
\end{aligned}
$$

The counterparts for the potential for the down spin electrons, $h_1^{\downarrow\uparrow}$ and $h_1^{\downarrow\downarrow}$ are obtained from the above two equations by interchanging the up and down spin indices on the exchange-correlation energy density, the Fourier coefficients of the electron density and the weighted spin density in the partial derivatives.

The derivatives of the C parameter can be easily determined from equation 4.78:

$$\frac{\partial C(\tilde{n}_\uparrow, \tilde{n}_\downarrow)}{\partial \tilde{n}_\uparrow} = \frac{C(\tilde{n}_\uparrow, \tilde{n}_\downarrow)}{\lambda(\tilde{n}_\uparrow, \tilde{n}_\downarrow)} \left(C(\tilde{n}_\uparrow, \tilde{n}_\downarrow) + 1 \right) \frac{\partial \lambda(\tilde{n}_\uparrow, \tilde{n}_\downarrow)}{\partial \tilde{n}_\uparrow}, \tag{4.100}$$

where the derivative with respect to the weighted down density is a trivial inspection of the above. For the λ parameter we perform implicit differentiation on equation 4.82 to get:

$$\frac{\partial \lambda(\tilde{n}_\uparrow, \tilde{n}_\downarrow)}{\partial \tilde{n}_\uparrow} = -\frac{\frac{\partial a_3}{\partial \tilde{n}_\uparrow} \lambda^3(\tilde{n}_\uparrow, \tilde{n}_\downarrow) \frac{\partial a_1}{\partial \tilde{n}_\uparrow} \lambda(\tilde{n}_\uparrow, \tilde{n}_\downarrow) + \frac{\partial a_0}{\partial \tilde{n}_\uparrow}}{3 a_3 \lambda^2(\tilde{n}_\uparrow, \tilde{n}_\downarrow) + a_1}. \tag{4.101}$$

The derivatives of the coefficients come from equations 4.83–4.85:

$$\frac{\partial a_3}{\partial \tilde{n}_\uparrow} = \left(\frac{\tilde{n}_\downarrow}{\tilde{n}} - \frac{\tilde{n}_\uparrow \tilde{n}_\downarrow}{\tilde{n}^2} \right) \left(I_1^a I_2^b - I_1^b I_2^a \right), \tag{4.102}$$

$$\frac{\partial a_0}{\partial \tilde{n}_\uparrow} = \left(\frac{v_\uparrow^{\text{LSDA}}[\tilde{n}_\uparrow, \tilde{n}_\downarrow] - \varepsilon_{\text{XC}}^{\text{LSDA}}[\tilde{n}_\uparrow, \tilde{n}_\downarrow] + \frac{4}{3} \tilde{n}_\uparrow^{\frac{1}{3}}}{\tilde{n}} - \frac{\tilde{n}_\uparrow^{\frac{4}{3}} + \tilde{n}_\downarrow^{\frac{4}{3}}}{\tilde{n}^2} \right) I_2^a, \tag{4.103}$$

$$\frac{\partial a_1}{\partial \tilde{n}_\uparrow} = \frac{\partial a_0}{\partial \tilde{n}_\uparrow} \frac{I_2^b}{I_2^a}. \tag{4.104}$$

For derivatives with respect to the weighted down density, a simple exchange of up and down indices is required.

Implementation in Spin Unpolarised Case

The implementation of the WSDA performs a calculation of the weighted up and down densities, effectively doubling the calculation time over the original WDA. For spin degenerate cases, where we would like to apply our spin-resolved model pair-correlation function, this is not required and simplifications can be made. A quick and easy way to do this is to perform the calculation for, say, parallel up spin pairs, determine the weighted up density, and contributions to the exchange-correlation

energy and potential. We can then duplicate this information for the parallel down spin pair contributions. Rather than create a simplified implementation for the antiparallel spin contributions we perform the calculation using the duplicated data. While this may not be the most efficient implementation possible, the overhead is negligible as the most expensive step of the calculation is determining the weighted density from the parallel spin contributions.

4.4 Testing

To test our implementation in CASTEP we initially applied our code to the homogeneous electron gas at a number of electron densities. For both the exchange-correlation energy and potential the results, within numerical accuracy, match those for the LDA. Tests were also applied for a fixed density with varying degrees of spin polarisation. Again, values for the exchange-correlation energy and potential agreed with the LSDA to good numerical accuracy. The values for the weighted spin densities were also found to match the actual homogeneous values used, as expected.

A more stringent test for inhomogeneous systems is to compare numerical and analytic values for interatomic forces using the Hellmann-Feynman theorem [60]. This demonstrates that the exchange-correlation energy is consistent with the potential. We did this by placing a hydrogen (H_2) molecule with a bond length of 0.7 Å in a cell of dimensions $4 \times 2 \times 2$ Å^3 with the molecule aligned along the long axis. A calculation was then performed using a well converged value of the kinetic energy cutoff to obtain a value for the analytic force. Total energy calculations were then repeated for displacement of one of the nuclei by 0.001 Å in each direction. A finite difference calculation of the derivative of the energy with respect to the displacement can then be performed to obtain a numerical value for the force and compared to the analytic value. Our values matched to within less than one hundredth of a percent, comparable, if not better than, the consistency obtained using the LDA. Satisfactory tests were also performed using an H_2^- ion in order to check the spin polarised consistency, which were, again, comparable to the same test using the LSDA.

4.5 Discussion of Functional Forms

In a Chapter 2 we discussed use of some of the simple functional forms that can be used in the WDA. It was apparent that we could pick a model function to give us the best results for a particular system, but with no guarantee that this would work for other systems, i.e. transferability. There would appear to be no systematic way of picking a model pair-correlation function appropriate for each task. This "pick and choose" methodology is counter to the idea of *ab initio* calculations. We prefer to take the non-empirical approach of fitting to known physical constraints, rather than to sets of empirical data.

Currently our constraints on the model functions have been to simply ensure that the sum rule for the exchange-correlation hole is satisfied and that the L(S)DA energy is returned in the homogeneous limit. In Chapter 2 we added the constraint of the Kimball cusp condition to some of our existing model functions. This made little change in predicted quantities using the simple Gaussian model applied to silicon, but did improve over the simple fourth order Gaussian model. We suggest that it is not enough to fit the on-top values of the pair-correlation function in the homogeneous limit along with the exchange-correlation energy, instead the entire model pair-correlation function should be exact in the homogeneous limit. However, by exact, we mean a fit to high quality quantum Monte-Carlo data and known short and long range limits.

High quality parameterisations of the coupling-constant averaged pair-correlation function are available [81] that also satisfy the Kimball cusp conditions. These parameterisations cover both the spin unpolarised and polarised cases, but to this date spin resolution of the pair-correlation function is only available in the unpolarised case. Until these become available, we can base our model pair-correlation function on the spin unpolarised parameterisations, while noting that these models will likely perform poorly in calculations with partial spin polarisation. Our code is written in a general fashion such that when spin resolved data in the spin polarised electron gas becomes available, it will be straightforward to implement a new functional with this form.

What is available to us is spin resolution of the correlation energy in the homoge-

neous electron gas [87] and hence spin resolution of the exchange-correlation energy in the uniform limit. We can then use the WSDA formalism to fit the spin resolved model-pair correlation function to return the spin resolved exchange-correlation energy in the homogeneous limit. We regard the ability of the WSDA framework to enforce more stringent constraint satisfaction to be an important feature in extending the accuracy of the WDA in general.

Another constraint available to us is the on top value of the spin resolved pair-correlation function. We can use this constraint to fit another *ab initio* parameter in our model pair-correlation functions, as this would effectively fit the value of the C parameter in our models. First principles models are available, such as that obtained through ladder theory and the solution of the Bethe-Goldstone equation [83, 86] and through the use of two-electron wavefunctions [84, 85]. There are also values extrapolated from quantum Monte-Carlo data [87].

We can also use this framework to enhance the model pair-correlation functions used in the unpolarised case of the WDA. Although the exchange-correlation energy is a functional of the total electron density only, the interactions between the electrons can still be broken down into those between parallel spin pairs and antiparallel spin pairs. We can then apply the constraints on the pair-correlation function to each individual component when constructing the full model functional.

4.6 Summary

A framework for a fully non-local spin polarised weighted spin density approximation has been proposed. An implementation suitable for periodic boundary conditions and a plane wave basis set is derived, such that the required integrals are evaluated in reciprocal space. The ability to model each spin resolved part of the pair-correlation function separately can allow us, in principle, to enforce more physical constraints on the model functional than was previously possible with the WDA. This approach also gives us insight into implementing novel functional forms for the spin unpolarised case and provides a roadmap to systematic improvement of model pair-correlation functions by constraint fitting. In the next chapter we will investigate a simple

functional form in comparison to the best spin resolved pair-correlation functions that are currently available, which are parameterisations of high quality quantum Monte-Carlo data. We will also investigate the importance of the modified cusp condition and make comparisons with a model pair-correlation function constructed from first principles.

Chapter 5

Pair-correlation: the Uniform Electron Gas

In the last chapter we constructed a weighted spin density approximation (WSDA) and demonstrated a practical implementation. We will now investigate our novel model pair-correlation functionals in the homogeneous electron gas and compare these with parameterisations of quantum Monte-Carlo data and constructions of pair-correlation functions from first principles. However, we do not have parameterisations available for the spin resolved pair-correlation function in the polarised electron gas upon which to base our model functions. We expect that our simple model will require further refinement.

5.1 Model Pair-Correlation Functions in the Uniform Limit

In Chapter 4, we gave a suggested model functional in the WSDA. For parallel spin pairs a simple Gaussian can be chosen as it is simple to implement and is a good qualitative comparison to the pair-correlation function for parallel spins, such as that given in reference [87]. For antiparallel spin pairs a more complicated model function is required in order to satisfy the cusp conditions of equations 4.10 and

4.13, and the sum rule of equation 4.7:

$$G^{\uparrow\downarrow}[u; \tilde{n}_\uparrow, \tilde{n}_\downarrow] = C(\tilde{n}_\uparrow, \tilde{n}_\downarrow) f^a(u) + \left(C(\tilde{n}_\uparrow, \tilde{n}_\downarrow) + 1 \right) \lambda(\tilde{n}_\uparrow, \tilde{n}_\downarrow) f^b(u). \tag{5.1}$$

We suggested that $f^a(u)$ be a simple Gaussian and that $f^b(u)$ be a product of a polynomial and a Gaussian such that the zero sum rule for anti parallel spin pairs can be satisfied:

$$f^b(u) = (u + u^2) e^{-\frac{u^2}{\kappa^2}}, \tag{5.2}$$

where κ is a constant. In order to fix a value of κ we look at the on-top value of the antiparallel spin pair-correlation function in the homogeneous limit as the on-top value for parallel spin pairs is always zero, so only antiparallel pair contributions need be considered. The value we have determined for our parameter is $\kappa = 0.81$. The on-top value for the antiparallel spin pair-correlation function has been determined for all densities using an approximation to ladder theory [86] and is given by:

$$g^{\uparrow\downarrow}(r, r) = \left[\frac{45(45 + 24x + 4x^2)}{2025 + 3105x + 1512x^2 + 256x^3} \right]^2, \tag{5.3}$$

where $x = 2\alpha r_s / \pi$ with $\alpha = (4/9\pi)^{1/3}$.

In Figure 5.1, we compare the pair-correlation function in the unpolarised homogeneous electron gas to that provided by our model. At high density the model function for parallel spins compares favourably with the QMC parameterisation of Gori-Giorgi, Sacchetti and Bachelet (GSB) [87]. At low density the model function significantly underestimates the value at long range and overestimates in the mid to short range. For antiparallel spins the model function compares well only in a narrow range around $r_s = 4$. At densities higher than this, the function overestimates the mid range and underestimates the short range value. In the case of lower densities, the short and long range value is overestimated while the mid range underestimates.

Considering the simplicity of our model, the qualitative comparison to the GSB parameterisation is good and suggests that fitting physical constraints even to the simplest of models can greatly improve the model pair-correlation function.

5.1.1 On-top Values of the Pair-Correlation Function – A Comparison of Models

Ladder theory is not the only method of determining the on-top value of the pair-correlation function from first principles. Another approach is to construct the short-range pair-correlation function from two-electron wave functions following the Overhauser method [84]. This models two-particle correlations with a non-empirical screening of the Coulomb potential. The assumption is that the probability of finding three electrons within a radius of r_s is zero. This is similar to the assumption in ladder theory that two-body interactions dominate the short range. In calculating the on-top value, these assumptions should be close to exact.

A third method that can be used to model the pair-correlation function in the uniform electron gas by using a hypernetted-chain (HNC) expansion of the wave function and then minimising the correlation energy variationally [88]. Again, the approximation is made that three particle correlations are ignored for the short range limit. However, none of the above approaches agree with each other for r_s values greater than ~ 1 and no values are available for the HNC below $r_s = 1$. Neither the Overhauser or ladder theory models have what is believed to be the correct behaviour in the high density limit [85, 86] determined from first order perturbation theory [89, 90]. For values above $r_s \sim 1$ there is a large range in the predicted values from each of the models.

In Figure 5.2 we show a graphical comparison of the on-top value of the pair-correlation function from a number of models. We have plotted, against r_s, the on-top value multiplied by r_s, in order to illustrate the differences between the models at low electron densities. The dashed line is that given by ladder theory [86] and the dash-dotted line is from the extended Overhauser model given by Gori-Giorgi and Perdew [85]. We also include the extrapolations to the on-top value for the QMC data of Ortiz, Harris and Ballone (OHB) [91] given by Gori-Giorgi, Sacchetti
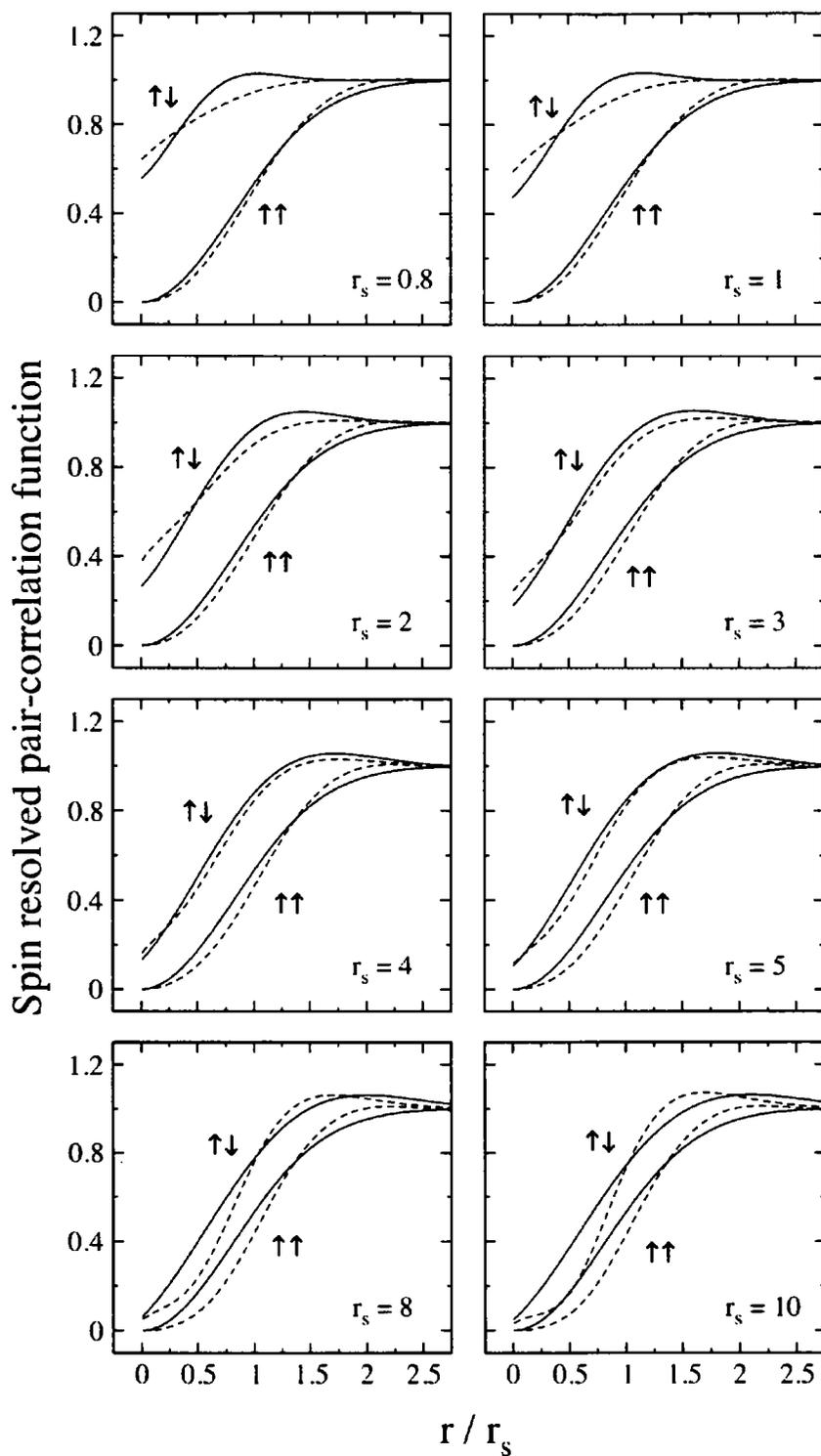
Figure 5.1: The spin resolved pair-correlation function for the homogeneous gas at a selection of r_s values. Solid lines are for our model functional, dashed lines for the GSB QMC parameterisation.
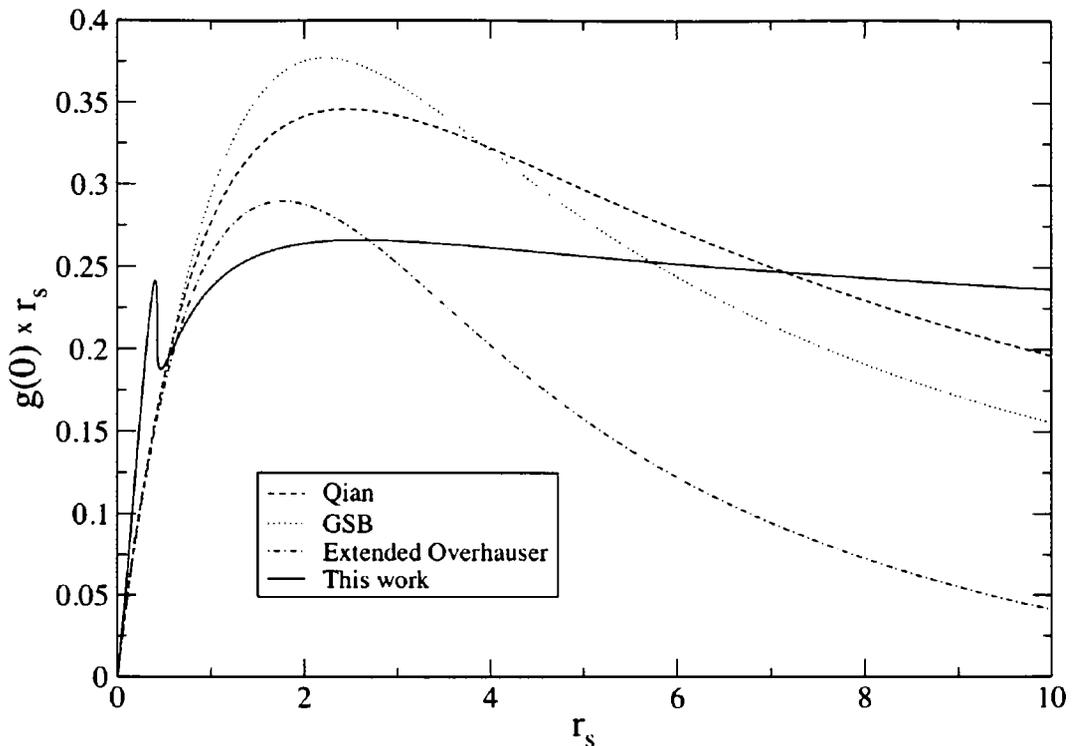
Figure 5.2: A comparison of on-top values of the pair-correlation function using a number of models. We plot the on-top value multiplied by r_s to emphasise the differences at low electron density (large r_s).

and Bachelet (GSB) [87], shown by the dotted line. With a solid line, we give, for comparison, the values given by our model WSDA fucntional form in equation 5.2 with $\kappa = 0.81$. Note that the unphysical feature below $r_s \approx 0.45$ is an artifact of the simple Gaussian model chosen for the parallel spins pair-correlation function. In this model the contribution to the exchange-correlation energy from parallel spin pairs approaches the total uniform (LDA) energy at $r_s = 0.426$ and then passes the LDA value, requiring a positive contribution to the energy from antiparallel spin pairs. This then causes our model to give an on-top value greater than the physical maximum of 0.5. The HNC values are, for the most part, too large to appear on the scale of our graph. This is because the method gives only a minimum upper bound on the correlation energy and the pair-correlation function from the calculated wave function is not guaranteed to be accurate.

Gori-Giorgi and Perdew argue that their extended Overhauser model is the best estimate currently available [85]. They point out that the high density limit of the on-top value for antiparallel spins in their model $(1 - 0.684r_s)$ is closer than that given by ladder theory $(1 - 0.663r_s)$, in comparison to the known exact limit of $1 - 0.7317r_s$. When comparing their model to the GSB extrapolation of QMC data they dismiss the discrepancies on the basis that the QMC data have large error bars at small particle separations. The relative closeness of Qian's solution using ladder theory to the QMC data could indicate that this opinion was overly optimistic. We conclude that there is still work to be done on determining reliable values for the on-top pair-correlation function, particularly at densities lower than $r_s = 1$. Our fit to ladder theory can still be justified as in the region of metallic electron density $(1 \lesssim r_s \lesssim 3)$, our model underestimates the on-top value of both ladder theory, the Overhauser model, and QMC data – the value of κ chosen maximises the on-top value. We note that our model is intended to be a trial of concept and expect further refinement to be necessary. Particularly once parameterisations are available for the spin resolved pair-correlation function in the polarised electron gas.

5.2   Modified Cusp Condition

Up to this point, we have been following the lead of Rushton [59] on constructing model pair-correlation functions incorporating the Kimball cusp condition. Perdew and Wang [61] point out that the coupling-constant averaged pair-correlation function, as used in calculating the exchange-correlation energy, in fact conforms to a modified cusp condition. This can be seen when applying the relationship between the pair-correlation function and its coupling-constant average to the cusp condition. We assume that the cusp condition for the coupling-constant averaged pair-correlation function (referred to here as $\bar{g}$) is modified as:

$$\frac{\partial}{\partial |r - r'|} \bar{g}^{\uparrow\downarrow}(r, r') \bigg|_{r \to r'} = H \bar{g}^{\uparrow\downarrow}(r, r') \bigg|_{r \to r'}, \tag{5.4}$$

where H is a function of the electron density parameter, r_s. Taking the known

relation between $g^{\uparrow\downarrow}$ and $\bar{g}^{\uparrow\downarrow}$:

$$\bar{g}^{\uparrow\downarrow}(\boldsymbol{r},\boldsymbol{r}) = \frac{1}{r_s}\int_0^{r_s} g^{\uparrow\downarrow}(\boldsymbol{r},\boldsymbol{r})dr_s', \tag{5.5}$$

we can show that H must satisfy the differential equation:

$$\frac{\bar{g}^{\uparrow\downarrow}(\boldsymbol{r},\boldsymbol{r})}{g^{\uparrow\downarrow}(\boldsymbol{r},\boldsymbol{r})}r_s\frac{\partial H}{\partial r_s} + \left(1 + \frac{\bar{g}^{\uparrow\downarrow}(\boldsymbol{r},\boldsymbol{r})}{g^{\uparrow\downarrow}(\boldsymbol{r},\boldsymbol{r})}\right)H = 1. \tag{5.6}$$

An approximate form for H is given by [61]:

$$H = \frac{1 + \gamma r_s}{2 + \delta r_s + \varepsilon r_s^2}, \tag{5.7}$$

where $\gamma = 0.3393$, $\delta = 0.9$, and $\varepsilon = 0.10161$. When substituting this into equation 5.6, the deviation of the left hand side from 1 is less than 0.1% for all r_s.

Clearly, this requires some alterations to our model pair-correlation function for antiparallel spins and the implementation of the WSDA. Equation 4.64 becomes:

$$G^{\uparrow\downarrow}[u; \tilde{n}_\uparrow, \tilde{n}_\downarrow] = C(\tilde{n}_\uparrow, \tilde{n}_\downarrow)f^a(u) + H(C(\tilde{n}_\uparrow, \tilde{n}_\downarrow) + 1)\lambda(\tilde{n}_\uparrow, \tilde{n}_\downarrow)f^b(u). \tag{5.8}$$

In the WSDA, H is a function of the weighted density and r_s, should be replaced with its "weighted" counterpart $\tilde{r}_s$. This change propagates through the implementation but requires few other alterations. The prefactor of the $F_x^b(q)$ functions, where $x = 1, 2, 3$, in equations 4.69, 4.74 and 4.94, becomes $H(1 + 1/C)\lambda$, where we neglect the explicit dependance on the weighted density for C and λ. The $C(\tilde{n}_\uparrow, \tilde{n}_\downarrow)$ parameter needs to be adjusted from equation 4.78:

$$C(\tilde{n}_\uparrow, \tilde{n}_\downarrow) = -\frac{H\lambda(\tilde{n}_\uparrow, \tilde{n}_\downarrow)I_2^b}{I_2^a + \lambda(\tilde{n}_\uparrow, \tilde{n}_\downarrow)I_2^b}. \tag{5.9}$$

We also need to modify the coefficients a_3 (equation 4.83) and a_1 (equation 4.84) in the cubic equation 4.82 used to determine $\lambda(\tilde{n}_\uparrow, \tilde{n}_\downarrow)$:

$$a_3 = H\frac{\tilde{n}_\uparrow \tilde{n}_\downarrow}{\tilde{n}} \left(I_1^a I_2^b - I_1^b I_2^a\right),$$

(5.10)

$$a_1 = H\left(\varepsilon_{\text{xc}}^{\text{LSDA}}[\tilde{n}_\uparrow, \tilde{n}_\downarrow] + \frac{\tilde{n}_\uparrow^{\frac{4}{3}} + \tilde{n}_\downarrow^{\frac{4}{3}}}{\tilde{n}}\right) I_2^b.$$

(5.11)

Because of cancellations due to the sum rule, the previous form of the potential terms remains unchanged. The remaining modifications are to the partial derivatives of $C(\tilde{n}_\uparrow, \tilde{n}_\downarrow)$, a_3 and a_1. Equation 4.100 becomes:

$$\frac{\partial C(\tilde{n}_\uparrow, \tilde{n}_\downarrow)}{\partial \tilde{n}_\uparrow} = \frac{C(\tilde{n}_\uparrow, \tilde{n}_\downarrow)}{\lambda(\tilde{n}_\uparrow, \tilde{n}_\downarrow)} \left(C(\tilde{n}_\uparrow, \tilde{n}_\downarrow) + 1\right) \frac{\partial \lambda(\tilde{n}_\uparrow, \tilde{n}_\downarrow)}{\partial \tilde{n}_\uparrow} + \frac{C(\tilde{n}_\uparrow, \tilde{n}_\downarrow)}{H} \left(C(\tilde{n}_\uparrow, \tilde{n}_\downarrow) + 1\right) \frac{\partial H}{\partial \tilde{n}_\uparrow},$$

(5.12)

and the derivatives of the a_3 and a_1 coefficients are:

$$\frac{\partial a_3}{\partial \tilde{n}_\uparrow} = \frac{\partial H}{\partial \tilde{n}_\uparrow}\frac{a_3}{H} + \frac{a_3}{\tilde{n}_\uparrow} - \frac{a_3}{\tilde{n}},$$

(5.13)

$$\frac{\partial a_1}{\partial \tilde{n}_\uparrow} = \frac{\partial H}{\partial \tilde{n}_\uparrow}\frac{a_1}{H} + H\frac{\partial a_0}{\partial \tilde{n}_\uparrow}\frac{I_2^b}{I_2^a},$$

(5.14)

where the partial derivative of a_0 is given in equation 4.103. As before, derivatives with respect to the weighted down density are obtained with a simple exchange of spin indices. The partial derivative of the modified cusp parameter H with respect to either weighted up or down density is:

$$\frac{\partial H}{\partial \tilde{n}_\sigma} = -\frac{4\pi}{9}\tilde{r}_s^4 \left(\frac{\gamma}{2 + \delta\tilde{r}_s + \varepsilon\tilde{r}_s^2} - \frac{(1 + \gamma\tilde{r}_s)(\delta + 2\varepsilon\tilde{r}_s)}{(2 + \delta\tilde{r}_s + \varepsilon\tilde{r}_s^2)^2}\right).$$

(5.15)

These modifications were implemented as an extension of our existing WSDA code within CASTEP and have been tested on the homogeneous electron gas and had the exchange-correlation energy and potential checked using the force theorem, using the same method and to similar accuracy as that described in section 4.4.

5.3 Comparisons of the Coupling-Constant Averaged Pair-Correlation Function

As before, we need to fit our model functional incorporating the modified cusp condition to be a best approximation of the coupling-constant averaged pair-correlation function in the homogeneous limit. Here we will choose the parameterisation of Gori-Giorgi and Perdew (GP) [81], which is determined using known exact limits and has good agreement with QMC data in the unpolarised gas without any fitting of free parameters. It is stable over all densities and extends to the partial and fully polarised electron gas. However, it should be kept in mind that the contribution of correlation in the fully polarised limit does not agree so well with QMC data. Spin resolution of the GP model is possible in principle but not trivial. At the time of writing, an analytic model of spin resolution is available only in the unpolarised limit [87], and in the case of the GP model, does not accurately agree with QMC data. Therefore we will use the full coupling-constant averaged pair-correlation function in our comparisons.

In fixing our κ parameter we found that the same value of 0.81 gave the best fit to the available on-top values. We obtained on-top values for the coupling-constant averaged pair-correlation function from ladder theory through numerical integration of equation 5.3. For comparison, we also used the values from the extended Overhauser model, which is used for the short range part of the GP model. Plots of these two models, along with our simple model, are shown in Figure 5.3. As would be expected from the comparisons in Figure 5.2, there are significant differences in the values given by ladder theory (dashed line) and the Overhauser model (dash-dotted line), although here they are not accentuated by multiplying the on-top value by r_s.
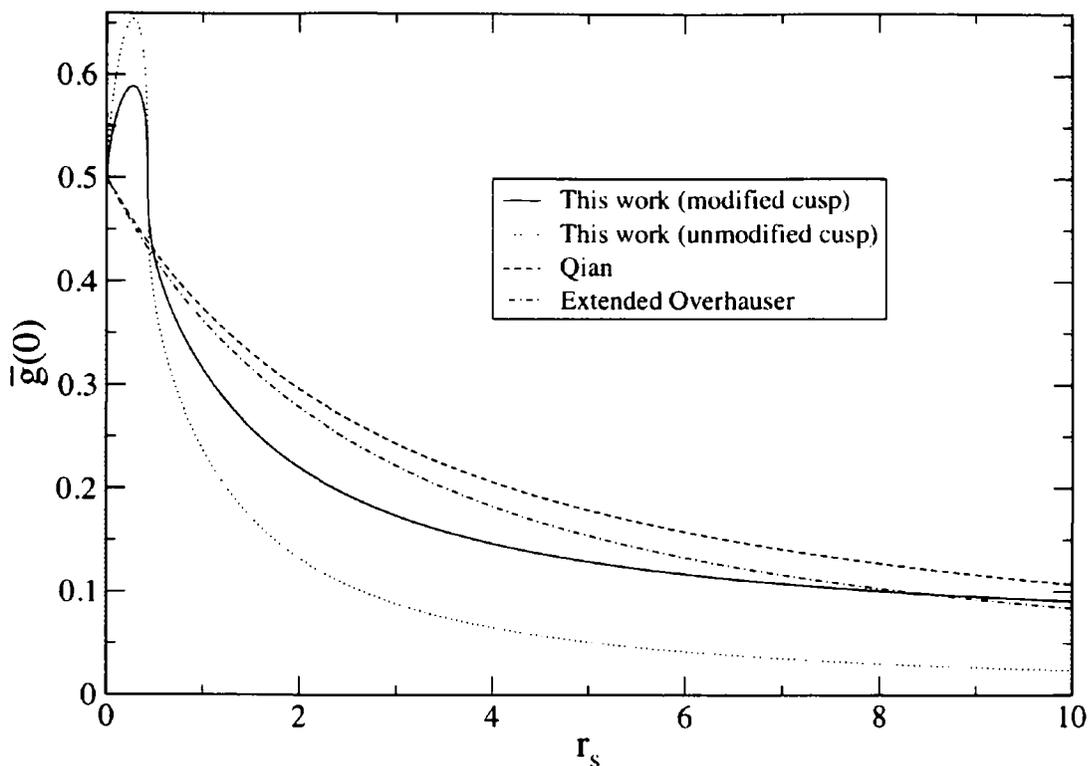
Figure 5.3: A comparison of on-top values of the coupling-constant averaged pair-correlation function using a selection of models.

The inclusion of the modified cusp condition in our model (solid line) greatly improves the on-top value for the coupling-constant averaged pair-correlation function over the use of the unmodified cusp condition (dotted line). Of course, our model with the modified cusp condition still suffers from the unphysical on-top values over 0.5 when going to densities higher than $r_s = 0.426$.

In Figure 5.4 we compare for the unpolarised electron gas, over a number of electron densities, the coupling-constant averaged pair-correlation function from the GP model (dashed line) to our models with (solid line) and without (dotted line) the modified cusp condition imposed. For our models, the inclusion of the modified cusp condition only alters the short range behaviour of the pair-correlation function. The long range part of the pair-correlation function compares well at metallic densities and is a reasonable approximation at other electron densities, albeit with a slight overestimation at separations greater than $r/r_s = 2$. In general there is a slight

undervaluing of of our models in the range $1 < r/r_s < 2$. Apart from at the lowest densities the short range part of our model functions is somewhat below that given by the GP model. For the short range, our model including the modified cusp condition is a consistent improvement over the initial model at all densities. This is to be expected from our investigation of the on-top values.

As the GP model also provides pair-correlation functions in the partial and fully polarised electron gas, we can compare our models over a range of polarisation values, $\zeta = (n_\uparrow - n_\downarrow)/n$. In Figure 5.5 we plot comparisons from $\zeta = 0.1 \rightarrow 1$ at a metallic electron density of $r_s = 2$. The long range part of the function compares excellently at all polarisations and only a slight underestimation in the range of particle separation $1 < r/r_s < 2$ that is more pronounced at high polarisations. As was found in the unpolarised case, our model including the modified cusp condition provides consistent improvements over our initial model in the short range. In the fully polarised limit the correct on-top value is returned for both of our models because there is no contribution to the pair-correlation function from antiparallel spin pairs.

5.4 Summary

We have compared the spin resolved pair-correlation function of our initial model WSDA functional with the GSB parameterisation of QMC data. This has shown that our model comes closest to QMC data at metallic densities. An investigation into the on-top values of the pair-correlation function provided by first principles models (ladder theory and the Overhauser approximation) and extrapolation of QMC data illustrates that there is still no consensus on the best approach. The importance of including a modified cusp condition when modeling the coupling-constant averaged pair-correlation function was established. Modifications to our initial approach were considered and implemented. Comparisons with a model constructed completely from first principles were made and it was demonstrated that inclusion of the modified cusp condition provided a systematic improvement over our initial model. This statement holds true over all densities and polarisations of the
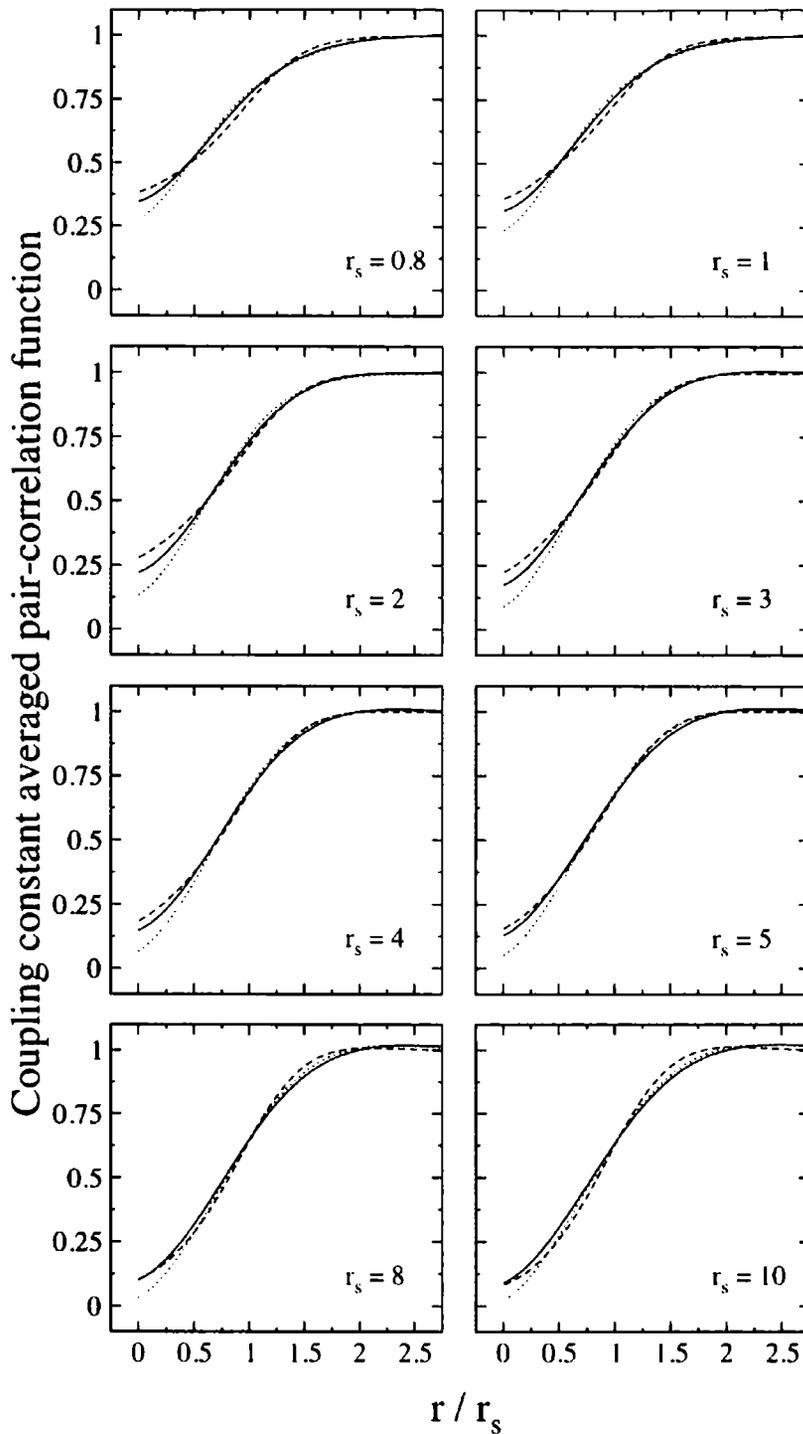
Figure 5.4: The coupling-constant averaged pair-correlation function for the unpolarised homogeneous gas at a selection of r_s values. Solid lines are for our model functional with the modified cusp condition, dotted lines are for our model without the modified cusp condition, and dashed lines for the GP model.
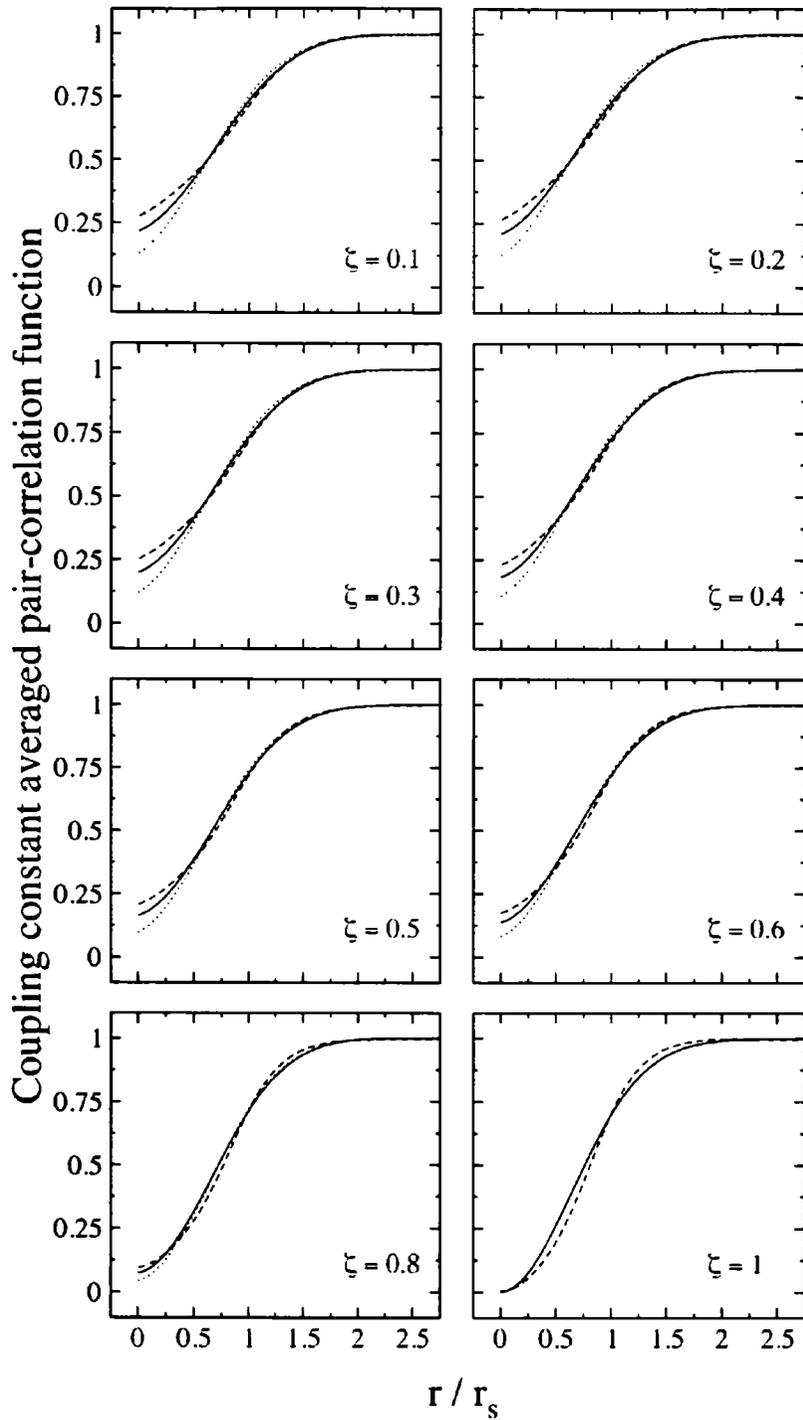
Figure 5.5: The coupling-constant averaged pair-correlation function for the partially and fully polarised homogeneous gas at $r_s = 2$ values. Solid lines are for our model functional with the modified cusp condition, dotted lines are for our model without the modified cusp condition, and dashed lines for the GP model.

uniform electron gas. In the next chapter we will apply our models to real, inhomogeneous systems. Calculations on unpolarised systems will be presented. This will include detailed studies of the electronic and bulk properties of silicon and germanium utilising our different models and an overview of a number of simple materials with the rock salt and zincblende structures. We will also present simulations of spin polarised systems, including iron and iron(II) oxide.

Chapter 6

Application of Novel WDA Model Functionals

In Chapter 4 we established a novel method of applying the WDA with spin resolution of the pair-correlation function. In Chapter 5 we adapted our simple spin polarised model to account for the correct modified cusp condition found for the coupling-constant averaged pair-correlation function. We have also previously demonstrated a model pair-correlation function in the unpolarised case that includes the Kimball cusp condition. In this chapter we will adapt the model from Chapter 2 to satisfy the modified cusp condition.

We now have a number of new WDA functionals for both the unpolarised and polarised cases. We will apply these new functional forms to spin unpolarised systems, including our spin resolved model. Our applications will concentrate on simple semiconductors. Applications to spin polarised systems will also be made for iron and iron(II) oxide.

6.1   Modified Cusp Condition – Unpolarised Case

In the last chapter we showed that the coupling-constant averaged pair-correlation function modeled in the WDA is subject to a modified cusp condition. This also applies in the unpolarised case we derived in Chapter 2. To recap, the modified cusp

condition is:

$$\frac{\partial}{\partial |r - r'|}\bar{g}(r, r')\bigg|_{r \to r'} = H\bar{g}(r, r')|_{r \to r'}, \tag{6.1}$$

where $\bar{g}$ is the coupling-constant averaged pair-correlation function and H is a parameter that depends on the electron density, n, via the parameter $r_s = (3/4\pi n)^{1/3}$. In the same way as was used for obtaining equation 5.6, it can be shown [61] that H must satisfy the differential equation:

$$\frac{\bar{g}(r, r)}{g(r, r)} r_s \frac{\partial H}{\partial r_s} + \left(1 + \frac{\bar{g}(r, r)}{g(r, r)}\right) H = 1, \tag{6.2}$$

where g is the pair-correlation function. An approximate form for H is given in equation 5.7.

The model pair-correlation function given in equation 2.69 , now becomes:

$$G^{\text{CWDA}}[u, \tilde{n}(r)] = C(\tilde{n}(r))f^a(u) + H(C(\tilde{n}(r)) + 1)\lambda(\tilde{n}(r))f^b(u). \tag{6.3}$$

This modification requires a small number of alterations from the previous implementation. The prefactor of the $F_x^b(q)$ functions, where $x = 1, 2, 3, 4$, in equations 2.71, 2.75, 2.93 and 2.98 becomes $H(1 + 1/C(\tilde{n}(r)))\lambda(\tilde{n}(r))$. Working from the homogeneous limit of the modified equations 2.70 and 2.74, the C parameter is now given by:

$$C(\tilde{n}(r)) = -\frac{1 + H\tilde{n}(r)\lambda^4(\tilde{n}(r))I_2^b}{\tilde{n}(r)\lambda^3(\tilde{n}(r))(I_2^a + H\lambda(\tilde{n}(r))I_2^b)}, \tag{6.4}$$

where the constants I_2^a and I_2^b remain as given in equation 2.81 and λ satisfies the quartic equation 2.83. The coefficients of this quartic are now:

$$a_4 = H\tilde{n}(r)(I_1^a I_2^b - I_1^b I_2^a), \tag{6.5}$$

$$a_2 = 2H\varepsilon_{\text{XC}}^{\text{LDA}}(\tilde{n}(r))I_2^b, \tag{6.6}$$

$$a_1 = 2\varepsilon_{\text{XC}}^{\text{LDA}}(\tilde{n}(r))I_2^a + HI_1^b, \tag{6.7}$$

$$a_0 = I_1^a, \tag{6.8}$$

where the coefficient $a_3 = 0$ and the constants I_1^a and I_1^b are unchanged from equation 2.80.

As the parameter H depends on the electron density, an extra term is required in the derivative of the model pair-correlation function:

$$\frac{\partial G^{\text{CWDA}}[u, \tilde{n}(r)]}{\partial \tilde{n}(r)} = \frac{\partial G^{\text{CWDA}}[u, \tilde{n}(r)]}{\partial C(\tilde{n}(r))}\frac{\partial C(\tilde{n}(r))}{\partial \tilde{n}(r)} + \frac{\partial G^{\text{CWDA}}[u, \tilde{n}(r)]}{\partial \lambda(\tilde{n}(r))}\frac{\partial \lambda(\tilde{n}(r))}{\partial \tilde{n}(r)}$$

$$- \frac{u}{\lambda(\tilde{n}(r))}\frac{\partial G^{\text{WDA}}[u, \tilde{n}(r)]}{\partial u}\frac{\partial \lambda(\tilde{n}(r))}{\partial \tilde{n}(r)} + \frac{\partial G^{\text{CWDA}}[u, \tilde{n}(r)]}{\partial H}\frac{\partial H}{\partial \tilde{n}(r)}. \tag{6.9}$$

The derivative of H is similar to equation 5.15:

$$\frac{\partial H}{\partial \tilde{n}} = -\frac{4\pi}{9}\tilde{r}_s^4\left(\frac{\gamma}{2 + \delta\tilde{r}_s + \varepsilon\tilde{r}_s^2} - \frac{(1 + \gamma\tilde{r}_s)(\delta + 2\varepsilon\tilde{r}_s)}{(2 + \delta\tilde{r}_s + \varepsilon\tilde{r}_s^2)^2}\right), \tag{6.10}$$

and we have $\gamma = 0.3393$, $\delta = 0.9$ and $\varepsilon = 0.10161$ from reference [61] and $\tilde{r}_s = (3/4\pi\tilde{n})^{1/3}$. We substitute equation 6.9 back into equations 2.20 and 2.21 and rewrite in reciprocal space to get:

$$
\begin{aligned}
h_1(\boldsymbol{r}) \;=\; & \frac{2\varepsilon_{\mathrm{xc}}^{\mathrm{CWDA}}(\boldsymbol{r})}{C(\tilde{n}(\boldsymbol{r}))}\frac{\partial C(\tilde{n}(\boldsymbol{r}))}{\partial \tilde{n}(\boldsymbol{r})} + 4\pi \sum_{\boldsymbol{G}} \tilde{n}(\boldsymbol{G}) e^{i\boldsymbol{G}\cdot\boldsymbol{r}} \\[2mm]
& \times \left[H(C(\tilde{n}(\boldsymbol{r})) + 1)\lambda^2(\tilde{n}(\boldsymbol{r}))\frac{\partial \lambda(\tilde{n}(\boldsymbol{r}))}{\partial \tilde{n}(\boldsymbol{r})} F_1^b(q) - \right. \\[2mm]
& \frac{H\lambda^3(\tilde{n}(\boldsymbol{r}))}{C(\tilde{n}(\boldsymbol{r}))}\frac{\partial C(\tilde{n}(\boldsymbol{r}))}{\partial \tilde{n}(\boldsymbol{r})} F_1^b(q) - C(\tilde{n}(\boldsymbol{r}))\lambda(\tilde{n}(\boldsymbol{r}))\frac{\partial \lambda(\tilde{n}(\boldsymbol{r}))}{\partial \tilde{n}(\boldsymbol{r})} H_3(q) + \\[2mm]
& \left. (C(\tilde{n}(\boldsymbol{r})) + 1)\lambda^3(\tilde{n}(\boldsymbol{r}))\frac{\partial H}{\partial \tilde{n}(\boldsymbol{r})} F_1^b(q) \right],
\end{aligned}
\tag{6.11}
$$

$$
\begin{aligned}
h_2(\boldsymbol{r}) \;=\; & \frac{-1}{C(\tilde{n}(\boldsymbol{r}))}\frac{\partial C(\tilde{n}(\boldsymbol{r}))}{\partial \tilde{n}(\boldsymbol{r})} + 4\pi \sum_{\boldsymbol{G}} \tilde{n}(\boldsymbol{G}) e^{i\boldsymbol{G}\cdot\boldsymbol{r}} \\[2mm]
& \times \left[H(C(\tilde{n}(\boldsymbol{r})) + 1)\lambda^3(\tilde{n}(\boldsymbol{r}))\frac{\partial \lambda(\tilde{n}(\boldsymbol{r}))}{\partial \tilde{n}(\boldsymbol{r})} F_2^b(q) - \right. \\[2mm]
& \frac{H\lambda^4(\tilde{n}(\boldsymbol{r}))}{C(\tilde{n}(\boldsymbol{r}))}\frac{\partial C(\tilde{n}(\boldsymbol{r}))}{\partial \tilde{n}(\boldsymbol{r})} F_2^b(q) - C(\tilde{n}(\boldsymbol{r}))\lambda^2(\tilde{n}(\boldsymbol{r}))\frac{\partial \lambda(\tilde{n}(\boldsymbol{r}))}{\partial \tilde{n}(\boldsymbol{r})} H_4(q) + \\[2mm]
& \left. (C(\tilde{n}(\boldsymbol{r})) + 1)\lambda^4(\tilde{n}(\boldsymbol{r}))\frac{\partial H}{\partial \tilde{n}(\boldsymbol{r})} F_2^b(q) \right].
\end{aligned}
\tag{6.12}
$$

The remaining modifications are to the derivatives of the scalar fields C and λ. From implicit differentiation of equation 2.83 we get:

$$
\frac{\partial \lambda(\tilde{n}(\boldsymbol{r}))}{\partial \tilde{n}(\boldsymbol{r})} = -\frac{\frac{\partial a_4}{\partial \tilde{n}(\boldsymbol{r})}\lambda^4(\tilde{n}(\boldsymbol{r})) + \frac{\partial a_2}{\partial \tilde{n}(\boldsymbol{r})}\lambda^2(\tilde{n}(\boldsymbol{r})) + \frac{\partial a_1}{\partial \tilde{n}(\boldsymbol{r})}}{4a_4\lambda^3(\tilde{n}(\boldsymbol{r})) + 2a_2\lambda(\tilde{n}(\boldsymbol{r})) + a_1},
\tag{6.13}
$$

where the derivatives of the coefficients are:

$$\frac{\partial a_4}{\partial \tilde{n}(r)} = \frac{a_4}{\tilde{n}(r)} + \frac{a_4}{H}\frac{\partial H}{\partial \tilde{n}(r)}, \tag{6.14}$$

$$\frac{\partial a_2}{\partial \tilde{n}(r)} = 2HI_2^b\frac{\partial \varepsilon_{XC}^{LDA}}{\partial \tilde{n}(r)} + \frac{a_2}{H}\frac{\partial H}{\partial \tilde{n}(r)}, \tag{6.15}$$

$$\frac{\partial a_1}{\partial \tilde{n}(r)} = 2I_2^a\frac{\partial \varepsilon_{XC}^{LDA}}{\partial \tilde{n}(r)} + I_1^b\frac{\partial H}{\partial \tilde{n}(r)}, \tag{6.16}$$

and the derivative of the LDA exchange-correlation energy density is given in equation 2.103. The derivative of the C parameter is:

$$\frac{\partial C(\tilde{n}(r))}{\partial \tilde{n}(r)} = \frac{1}{\tilde{n}^2(r)\lambda^3(\tilde{n}(r))(I_2^a + H\lambda(\tilde{n}(r))I_2^b)}$$

$$+ \frac{\partial C(\tilde{n}(r))}{\partial \lambda(\tilde{n}(r))}\frac{\partial \lambda(\tilde{n}(r))}{\partial \tilde{n}(r)} + \frac{\partial C(\tilde{n}(r))}{\partial H}\frac{\partial H}{\partial \tilde{n}(r)}, \tag{6.17}$$

where the derivative with respect to λ is:

$$\frac{\partial C(\tilde{n}(r))}{\partial \lambda(\tilde{n}(r))} = \frac{3I_2^a + 4H\lambda(\tilde{n}(r))I_2^b - \tilde{n}(r)HI_2^aI_2^b\lambda^4(\tilde{n}(r))}{\tilde{n}(r)\lambda^4(\tilde{n}(r))(I_2^a + H\lambda(\tilde{n}(r))I_2^b)^2}, \tag{6.18}$$

and the derivative with respect to H is:

$$\frac{\partial C(\tilde{n}(r))}{\partial H} = \frac{I_2^b - \tilde{n}(r)I_2^aI_2^b\lambda^3(\tilde{n}(r))}{\tilde{n}(r)\lambda^2(\tilde{n}(r))(I_2^a + H\lambda(\tilde{n}(r))I_2^b)}. \tag{6.19}$$

We have implemented these modifications and have run successful tests on the homogeneous electron gas and consistency of the exchange-correlation potential using numerical and analytically derived atomic forces. The method used is given at the end of section 2.4.1. Values for the analytic and numerical forces were found to be identical to fractions of a percent.

The parameter κ takes the same values of 0.88 and 0.95 (determined in Chapter 2) for the Gaussian and fourth order Gaussian based models, respectively. On-top values in the homogeneous limit fall between those given in Table 2.2.

6.2 Application to Semiconductors

Our spin polarised WDA (WSDA) provides a new class of a spin resolved model pair-correlation function that can also be applied to situations where spin polarisation is disregarded. Although these systems are spin degenerate, the spin resolution of the pair-correlation function allows more physical constraints to be satisfied over the original WDA or cusp modified WDA. This is because even when the system is spin degenerate, the physical interactions can be spin resolved, i.e. parallel spin pair interactions are subject to both exchange and correlation effects whereas antiparallel spin pair interactions are purely Coulomb correlation as there is no Pauli exclusion in this case. It is of interest to see this new model applied in these situations as well as those with spin polarisation.

6.2.1 Bulk Silicon

In section 2.4.3 we applied the WDA to silicon and made comparisons between the simple Gaussian and fourth order Gaussian models used in the original WDA, the corresponding cusp condition satisfying models and the LDA, PBE GGA and experiment. Here we will extend Table 2.3 to include the modified cusp condition, the simple spin resolved model suggested in Chapter 4 and the modified cusp condition for antiparallel spin pairs. The structure and simulation conditions are identical to those used in section 2.4.3.

Our extended results are given in Table 6.1. For the spin unpolarised models of the Gaussian and fourth order Gaussian forms, the modified cusp condition gives values between those given by the original WDA models and the initial model attempting to account for the Kimball cusp condition. The small differences between the original, cusp and modified cusp models suggest that the choice of WDA model is relatively insensitive to minor alterations of the on-top value of the model

Table 6.1: An extension of Table 2.3 for bulk properties of silicon. As given by a number of models for exchange-correlation – the equilibrium lattice parameter, a_0, bulk modulus, B_0, and indirect band gap, E_g, for the Kohn-Sham band structure at both the equilibrium and experimental lattice parameter.

Model	a_0(Å)	B_0(GPa)	E_g(eV)	E_g(eV, exp. lattice)
e^{-u^2}	5.438	87.5	0.553	0.547
e^{-u^2} (cusp)	5.449	85.7	0.643	0.627
e^{-u^2} (modified cusp)	5.444	86.4	0.601	0.590
e^{-u^4}	5.402	94.3	0.306	0.333
e^{-u^4} (cusp)	5.433	88.8	0.540	0.539
e^{-u^4} (modified cusp)	5.416	91.6	0.420	0.434
WSDA	5.597	58.1	1.135	0.994
WSDA (modified cusp)	5.607	57.7	1.115	0.964
LDA	5.375	96.6	0.439	0.490
PBE	5.374	92.9	0.624	0.678
Exp.	5.431	98.8	1.17	1.17

pair-correlation function.

The spin resolved models provide a completely novel approach for the model pair-correlation function, determining the weighted density purely from contributions from parallel spin pairs. As with our spin degenerate models, there is little difference in results between the initial attempt to satisfy the Kimball cusp condition and the correct modified cusp condition. This reinforces the suggestion that these physical properties are insensitive to minor alterations of the short range model pair-correlation function. The predicted lattice parameter is larger than experiment by approximately 3 percent, and the bulk modulus is disappointingly low. This could be a result of inadequacies in the spin resolution of the exchange-correlation energy, which we will discuss later. The indirect band gap, however, shows a significant increase over all the other models presented, giving a value within 5 percent of the experimental value, while still underestimating the experimental value slightly.

There is no reason that the Kohn-Sham band structure should equal the exact band structure, even if there were an exact exchange-correlation functional [5]. The improvements in predicted values from our WSDA model are, however, consistent with values given by other non-local functionals such as screened exchange–LDA [92].

6.2.2 Bulk Germanium

The success of Gaussian based model pair-correlation functions applied to silicon could be a result of the favourable comparison of the WDA exchange-correlation hole with that determined by quantum Monte Carlo [57]. It should be useful therefore, to repeat the application of our models to a similar structure with different physical properties. This can be found in the diamond structure of germanium, which can be seen in Figure 2.5, if Ge is substituted for Si. Our simulation cell was the primitive one, containing two Ge atoms. A plane wave cutoff energy of 300 eV and a Monkhorst-Pack grid of $4 \times 4 \times 4$ k-points was used to sample the Brillouin zone. This converges the total energy differences to less than 5 meV. We used ultrasoft pseudopotentials generated by the LDA in each of our calculations.

Table 6.2: As for Table 6.1, but for Germanium.

Model	$a_0(\text{Å})$	$B_0(\text{GPa})$	$E_g(\text{eV})$	$E_g(\text{eV, exp. lattice})$
e^{-u^2}	5.609	69.4	0.246	0.001
e^{-u^2} (cusp)	5.625	66.9	0.107	0.004
e^{-u^2} (modified cusp)	5.618	68.0	0.202	0.003
e^{-u^4}	5.558	77.7	0.492	0.000
e^{-u^4} (cusp)	5.603	70.4	0.275	0.000
e^{-u^4} (modified cusp)	5.578	74.2	0.404	0.000
WSDA	5.847	34.7	0.000	0.024
WSDA (modified cusp)	5.856	35.2	0.000	0.000
LDA	5.544	78.3	0.631	0.037
PBE	5.549	75.7	0.683	0.102
Exp.	5.657	76.8	0.74	0.74

In Table 6.2 we show the equilibrium lattice parameter, bulk modulus, band gap at equilibrium and the band gap at the experimental value of the lattice parameter. The lattice parameter and bulk modulus was calculated by the usual method of calculating the total energy at a number of lattice parameter values and fitting the resulting energy volume curve to the Murnaghan equation of state. The spin unpolarised models all underestimate the lattice parameter somewhat, with the fourth order Gaussian based models having a larger difference. Including the cusp condition reduces the underestimation to less than 1 percent for the Gaussian based model with the modified cusp condition. The bulk modulus is also underestimated except for the original fourth order Gaussian model that has a very slight overestimation. The models including the cusp condition give an increased underestimation over the original models while the models with the modified cusp condition alleviate this trend slightly. The direct band gaps at the experimental lattice parameter are negligible (for the Gaussian based models) or zero (for the fourth order Gaussian models). At the equilibrium lattice parameter, the band gaps underestimate experiment and the LDA and PBE GGA values, which themselves underestimate experiment. As was the trend with the bulk modulus, the original WDA models are closest to the experimental value, whereas the cusp condition satisfying models increase the underestimation. The modified cusp condition gives values between the original WDA and initial cusp condition models.

Our spin polarised models again show a relatively large overestimate in the values for the equilibrium lattice parameter, a difference of approximately 3 percent from experiment. Again, this could be a result of inadequacies in the spin resolution of the exchange-correlation energy, which we will discuss later. The calculated bulk modulus is proportionately even lower than those given for silicon, in comparison to experiment, giving values less than half of the experimental value. The band gap at the equilibrium lattice parameter is given as zero, as is the value for the modified cusp model at the experimental lattice parameter. Our initial WSDA model gives a very small direct gap with the experimental lattice parameter comparable, but smaller than that given by the LDA. We will discuss possible reasons for the failings of these models later.

6.2.3 Semiconductor Band Structures

Calculation of the Kohn-Sham band structure can provide useful insight into the behaviour of the "true" band structure even though the Kohn-Sham eigenvalues are not physically meaningful [5]. Band structures are a useful tool in deciding uses for any particular material as the electronic and optical properties can be inferred from them. We have previously calculated band gaps for silicon and germanium in the diamond structure but have not given a three dimensional band structure. This is done by calculating the Kohn-Sham eigenvalues at a number of k-points in the first Brillouin zone, following lines of symmetry, as shown in Figure 6.1
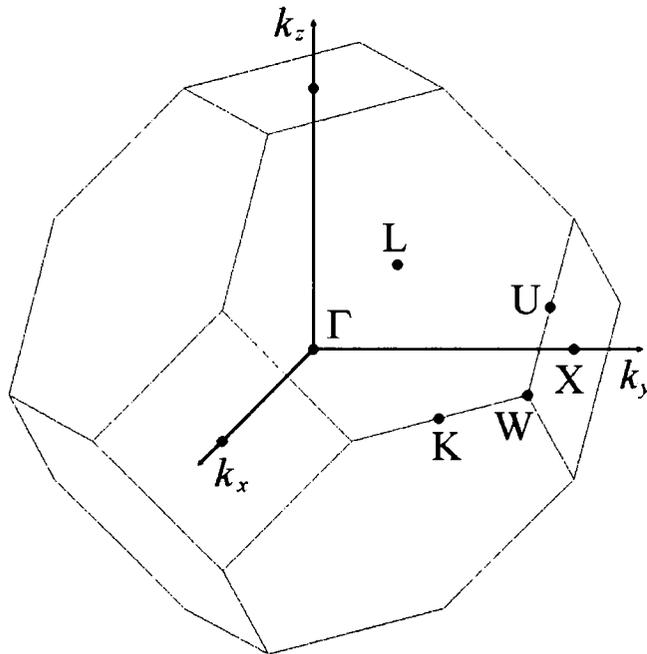
Figure 6.1: The first Brillouin zone of the face centered cubic lattice with points of symmetry shown. By convention, Greek characters are used for points within the Brillouin zone and Roman characters for points on the surface.

A full three dimensional band structure can be hard to present, so we will follow the conventional method of plotting the band structure along a one dimensional path that passes through points of symmetry, in this case, W $\rightarrow$ Γ $\rightarrow$ X $\rightarrow$ W $\rightarrow$ L $\rightarrow$ Γ. In Figure 6.2 we show a 2D representation of the above path through the 3D band structure of silicon, comparing LDA and our Gaussian based WDA

that satisfies the modified cusp condition. Likewise for Figure 6.3 except with the comparison here made between the LDA and the WSDA model that satisfies the modified cusp condition. Figures 6.4 and 6.5 show the equivalent band structures for germanium. In each case we have shifted the band structures such that zero is at the valence band maximum. In each case the equilibrium lattice parameter is used, as given in Tables 6.1 and 6.2.
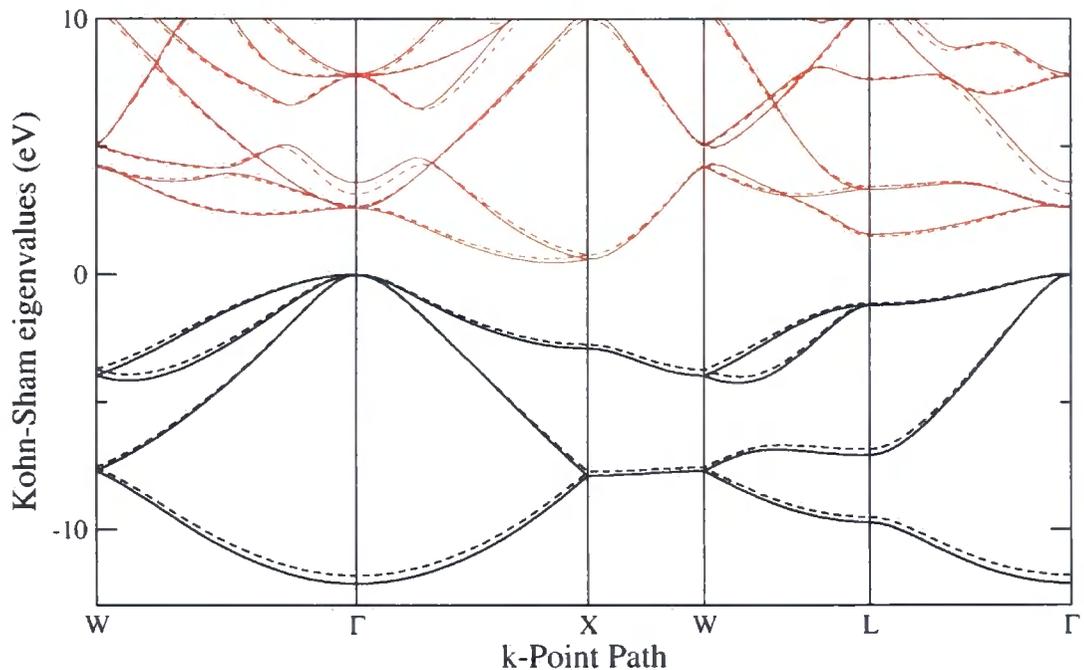
Figure 6.2: Kohn-Sham band structure for silicon using the LDA (dashed lines) and the Gaussian based modified cusp condition WDA. Black lines represent the valence bands, red line the conduction bands.

The modified cusp condition model in the spin unpolarised case only shows minor differences in comparison to the LDA for silicon. For the valence bands in Si it could be said that it consistently, if only slightly, lowers the bands in comparison to LDA. In the case of the WSDA, the differences from the LDA are substantial. The valence bands and lowest conduction bands are all raised, along with the increase in the indirect band gap that we reported earlier. It could be of interest to note that the direct band gap for the WSDA is slightly smaller than for the LDA, namely 2.15 eV compared to 2.57 eV, respectively. This is because of a crossing of bands predicted
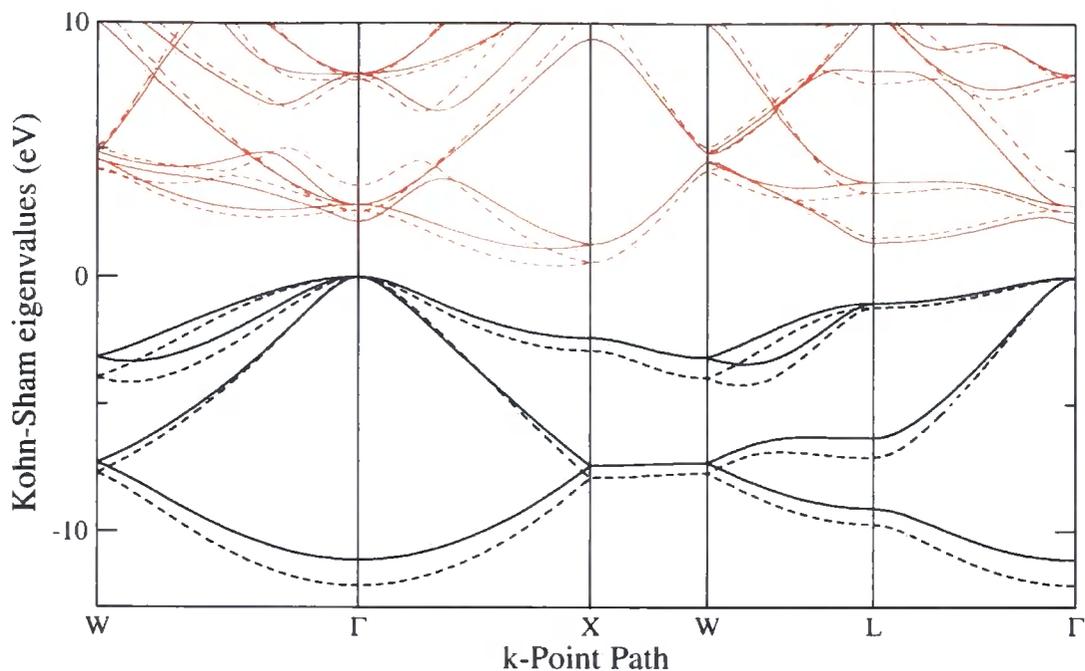
Figure 6.3: Kohn-Sham band structure for silicon using the LDA (dashed lines) and WSDA satisfying the modified cusp condition. Black lines represent the valence bands, red lines the conduction bands.

by our WSDA model that does not occur in the LDA or the modified cusp WDA.

In the case of germanium, the modified cusp WDA shows little difference over the LDA other than a reduction in the direct band gap by a factor of approximately three. With the WSDA, the changes in the band structure are substantial. Most notable is the complete closure of the band gap reported earlier. It has been noted elsewhere [92] that germanium band structures are particularly sensitive to the pseudopotential used. The ultrasoft pseudopotentials we used only treat the $4s$ and $4p$ electrons as valence. Treating the $3d$ electrons as valence also, could significantly change our band structures.

We now present band gaps for a large list of materials with zincblende and rock salt crystal structures. The zincblende lattice is closely related to the diamond structure shown in Figure 2.5, where alternating atoms are of a different element. The rock salt lattice is also face centered cubic, but the offset of the second atom is fractional coordinates of (0.5,0.5,0.5) in the primitive cell, rather than (0.25,0.25,0.25)
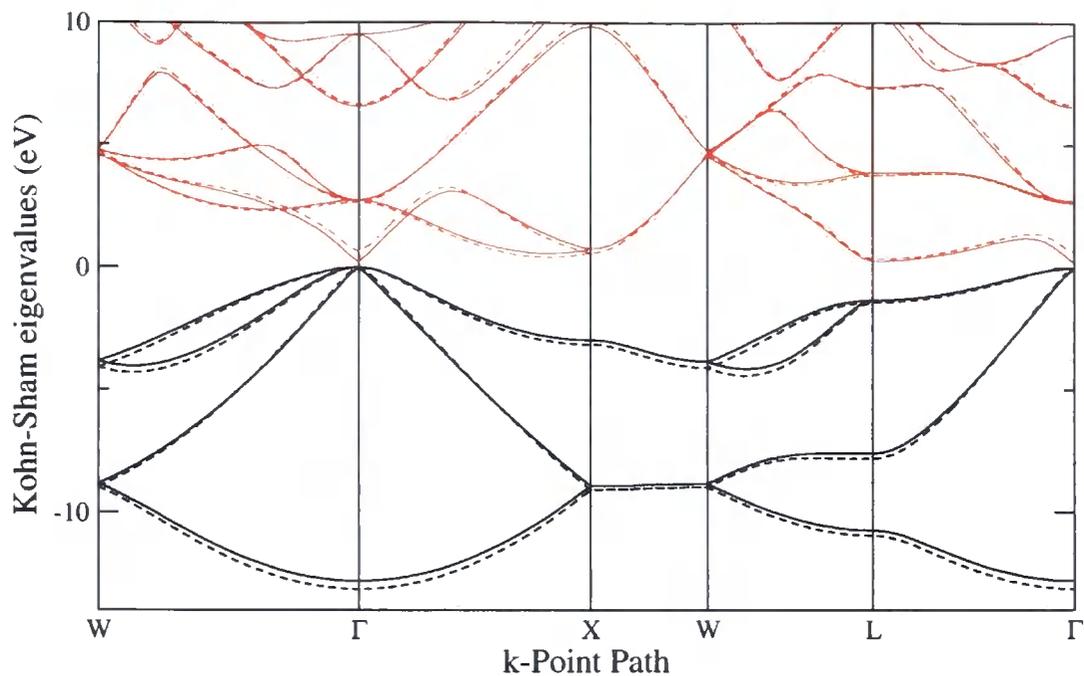
Figure 6.4: As for Figure 6.2, but for Germanium.
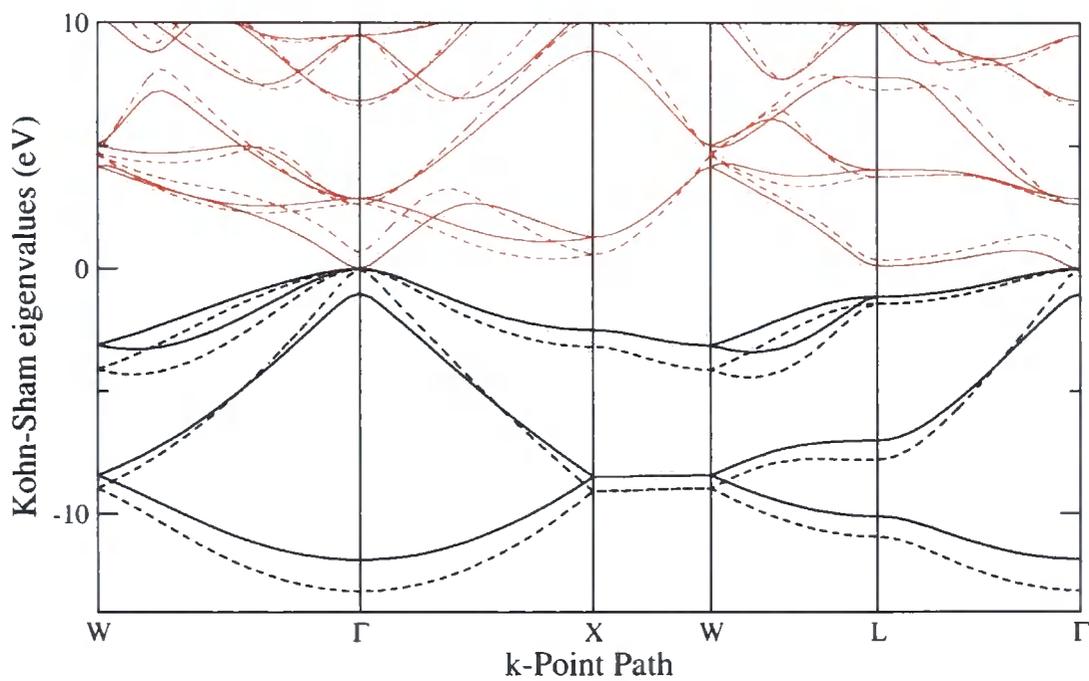
Figure 6.5: As for Figure 6.3, but for Germanium.

in the case of diamond/zincblende. In each case the experimental lattice parameter was used and a Monkhorst-Pack grid of $6 \times 6 \times 6$ was used to sample the Brillouin zone for the self consistent calculation. LDA ultrasoft pseudopotentials were used and a plane wave cutoff energy was chosen according to the atoms in each cell. A list of the 20 rock salt and 36 zincblende crystals along with the kinetic energy cutoff and the lattice parameter used is shown in Table 6.3.

Full band structures were generated along a k-point path of W $\to$ L $\to$ Γ $\to$ X $\to$ W $\to$ K. With such a large list of materials a graphical display of all 56 two dimensional representations of the band structures would achieve little. Even tabulation of Kohn-Sham eigenvalues at the various points of symmetry would provide little insight into the performance of a particular functional with this volume of data. Instead we will plot the calculated band gaps against experimental values for each of the LDA, modified cusp Gaussian WDA, and modified cusp WSDA. This provides a simple graphical means of showing the performance of each functional in the calculation of band gaps – the closer the point to the $y = x$ line, the better the comparison to experiment. This plot is shown in Figure 6.6 For completeness, we also tabulate the band gaps (in eV) in Table 6.4.

The experimental values for the band gaps in Table 6.4 are from reference [93], with a few exceptions. The band gap for the rock salt form of MgS is from reference [94]. A collation of experimental data for the alkali halide band gaps can be found in reference [95]. Lithium iodide is missing from this summary. Reference [96] suggests the band gap may take a value around 6 eV but that the optical data is sparse. CuF is chemically unstable and no reliable data is available [97]. AlN, InN and ZnO are found in the wurtzite structure and it would seem that there are no reported experimental data on the zincblende structure. Values are given for 0 K, where available.

From Table 6.4, it is apparent that our WSDA (blue triangles) is generally outperforming the LDA (green crosses) and modified cusp corrected WDA (red squares). There are a few notable exceptions to this statement. For GaAs the LDA gives the closest value to experiment, followed by our WSDA and last the modified CWDA. However all three greatly underestimate the experimental value, by a factor of 5 or

Table 6.3: List of materials, crystal structure, lattice parameter and cutoff energy.

Material	Struct.	E_{cut} (eV)	a (Å)	Material	Struct.	E_{cut} (eV)	a (Å)
AlAs	zb	290	5.61	MgTe	zb	340	6.37
AlN	zb	250	4.36	SiC	zb	280	4.34
AlP	zb	160	5.45	SiSi	zb	160	5.43
AlSb	zb	205	6.14	SnSn	zb	250	6.47
BAs	zb	290	4.78	ZnO	zb	340	4.51
BeO	zb	340	3.81	ZnS	zb	310	5.41
BeS	zb	220	4.85	ZnSe	zb	310	5.67
BeSe	zb	240	5.08	ZnTe	zb	310	6.10
BeTe	zb	190	5.54	CaO	rs	340	4.80
BN	zb	250	3.63	CdO	rs	340	4.69
BP	zb	240	4.55	KBr	rs	200	6.60
CC	zb	280	3.57	KCl	rs	230	6.30
CdS	zb	260	5.82	KF	rs	330	5.34
CdSe	zb	260	6.07	KI	rs	210	7.06
CdTe	zb	260	6.49	LiBr	rs	300	5.50
CuCl	zb	290	5.41	LiCl	rs	300	5.14
CuF	zb	330	4.25	LiF	rs	330	4.02
GaAs	zb	295	5.66	LiI	rs	300	6.00
GaN	zb	295	4.48	MgO	rs	340	4.21
GaP	zb	295	5.45	MgS	rs	340	5.20
GaSb	zb	295	6.12	NaBr	rs	370	5.98
GeGe	zb	180	5.66	NaCl	rs	370	5.64
InAs	zb	310	6.05	NaF	rs	370	4.64
InN	zb	310	4.96	NaI	rs	370	6.48
InP	zb	310	5.86	RbBr	rs	180	6.90
InSb	zb	310	6.47	RbCl	rs	230	6.58
MgS	zb	340	5.66	RbF	rs	330	5.64
MgSe	zb	340	5.91	RbI	rs	210	7.36

Table 6.4: List of band gaps (eV). See main text for details.

Material	LDA	modified CWDA	WSDA	Experiment
AlAs	1.272	1.383	1.840	2.23
AlN	3.270	3.533	3.741	-
AlP	1.455	1.632	2.069	2.51
AlSb	1.102	1.145	1.510	1.69
BAs	1.097	1.189	1.536	1.46
BeO	6.656	6.909	7.047	10.59
BeS	2.945	3.131	3.554	>5.5
BeSe	2.379	2.490	2.946	5.6
BeTe	1.759	1.774	2.227	2.8
BN	4.339	4.638	4.905	6.4
BP	1.173	1.327	1.662	2.4
CC	4.122	4.342	4.618	5.48
CdS	0.964	0.936	1.160	2.56
CdSe	0.358	0.269	0.511	1.85
CdTe	0.524	0.349	0.560	1.61
CuCl	0.265	0.314	0.388	3.40
CuF	-0.225	-0.207	-0.207	-
GaAs	0.290	0.132	0.184	1.52
GaN	1.831	1.804	1.909	3.3
GaP	1.407	1.432	1.534	2.34
GaSb	0.000	0.000	0.000	0.81
GeGe	0.020	0.001	0.000	0.74
InAs	0.000	0.000	0.000	0.42
InN	0.000	0.000	0.000	-
InP	0.522	0.426	0.538	1.42
InSb	0.000	0.000	0.000	0.23
MgS(zb)	3.274	3.116	3.435	4.87
MgSe	2.483	2.269	2.614	4.05

table continues...

Table 6.4 continued.

Material	LDA	modified CWDA	WSDA	Experiment
MgTe	2.413	2.102	2.427	3.2
SiC	1.332	1.578	1.902	2.42
SiSi	0.499	0.602	0.977	1.17
SnSn	-0.076	-0.038	0.000	0.082
ZnO	0.680	0.788	0.852	-
ZnS	1.936	1.891	2.092	3.84
ZnSe	1.047	0.924	1.138	2.82
ZnTe	1.074	0.855	1.022	2.39
CaO	3.476	3.410	3.418	7.8
CdO	-0.510	-0.399	-0.354	0.84
KBr	4.043	3.913	4.353	7.8
KCl	4.754	4.580	4.947	8.5
KF	5.857	5.619	5.778	10.9
KI	3.619	3.419	3.918	6.2
LiBr	4.659	4.644	4.892	7.6
LiCl	5.965	5.903	6.075	9.4
LiF	8.901	8.653	8.577	13.6
LiI	4.076	3.931	4.208	-
MgO	4.729	4.617	4.739	7.9
MgS(rs)	2.605	2.455	2.838	2.7
NaBr	3.778	3.579	4.022	7.7
NaCl	4.691	4.464	4.833	8.6
NaF	5.933	5.630	5.759	11.7
NaI	3.325	3.003	3.474	5.8
IRbBr	3.906	3.772	4.202	7.7
RbCl	4.550	4.379	4.738	8.2
RbF	5.329	5.146	5.335	10.4
RbI	3.513	3.321	3.817	6.1
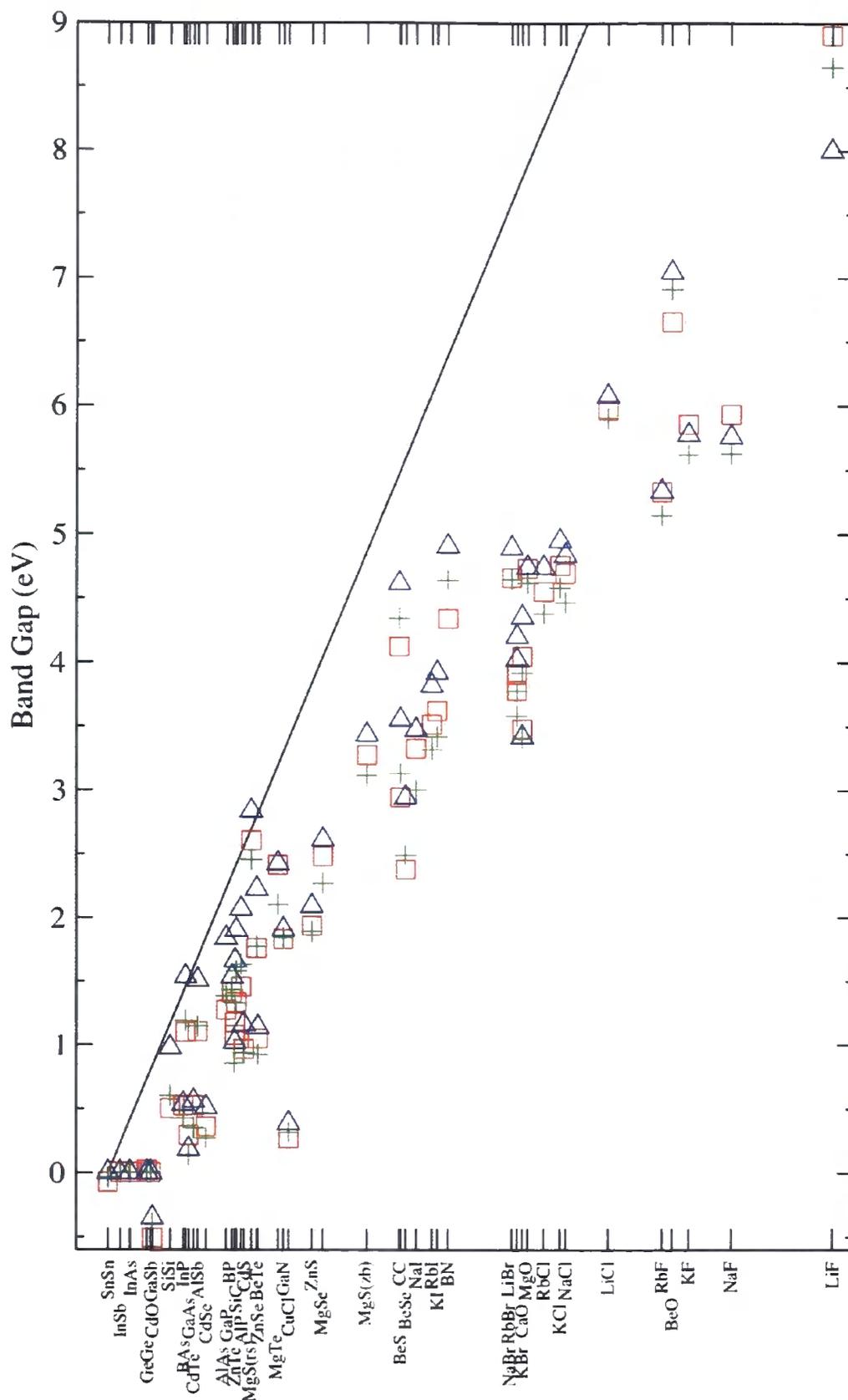
Figure 6.6: Comparison of band gaps. See main text for details.

more. The same holds for ZnTe and CaO, although the underestimation is closer to a factor of 2 in these cases. Diamond structure germanium was discussed earlier. All three models predict a zero gap for GaSb, InAs and InSb whereas experiment shows a gap is present in each of these materials. For the alkali metal fluorides, other than RbF, where values are almost identical, the LDA outperforms both other models. In LiF, the modified CWDA gives a value slightly better than the WSDA, the only material in our set in which this occurs. For α-tin only the WSDA gives a zero gap, whereas both the LDA and modified CWDA predict that it is a semimetal. All three models incorrectly predict that CdO is a semimetal. Although experimental data is not available for CuF, all three approximations predict that the material is metallic. When comparing only the LDA and modified CWDA, the LDA gives values closer to experiment for all the rock salt structures. For the zincblende structures performance is split half and half between the two. Overall, the differences in band gaps between the LDA and CWDA are minor, with only small fractions of eV between them. We will discuss possible reasons for the performance differences of our models later in this chapter.

6.3 WSDA Applied to Spin Polarised Systems

We have shown that our spin resolved weighted density approximation can be successfully applied to spin unpolarised systems. We now investigate how the WSDA behaves for some spin polarised situations.

6.3.1 Bulk Fe

Iron can be considered an obvious choice to start studying magnetic, and hence spin polarised systems. The LDA fails to determine the correct ground state structure of Fe [98]. In nature, Fe is found to be body centred cubic and ferromagnetic. According to the all-electron calculations of reference [98], the LDA gives the face centred cubic non-magnetic structure as the most stable and the PBE GGA predicts the correct structure. The body centred cubic (bcc) and face centered cubic (fcc) structures are shown graphically in Figure 6.7.
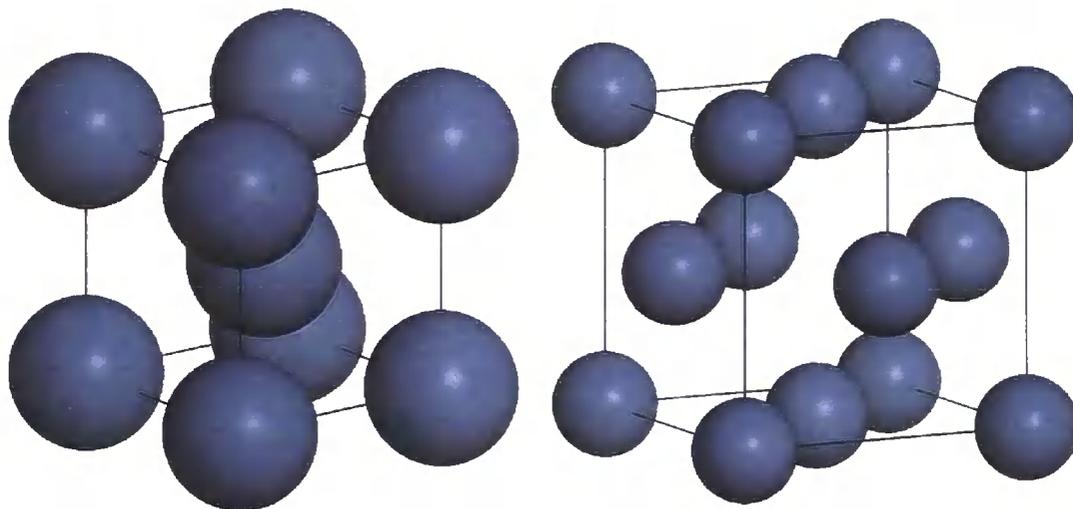
Figure 6.7: Fe in the bcc structure (left) and fcc structure (right).

We repeat the LDA and PBE calculations using ultrasoft pseudopotentials constructed with the LDA. We also perform calculations using our WSDA model including the modified cusp condition. To investigate the effect of using consistent pseudopotentials, we repeat the PBE calculations using PBE ultrasoft pseudopotentials. For each model of exchange-correlation, the non-magnetic fcc and bcc structures and the bcc ferromagnetic structures were used. In each of these cases the plane wave kinetic energy cutoff of 500 eV was used and a Monkhorst-Pack grid of dimensions $6 \times 6 \times 6$ was used to sample the Brillouin zone. This converges total energy differences to better than 13 meV per atom for the fcc structure and 3 meV per atom for the bcc structure. The total energies obtained are then used to construct an energy volume curve fitted to the Murnaghan equation of state, which allows us to determine the equilibrium lattice parameter and bulk modulus.

In Table 6.5 we show the equilibrium lattice parameter and bulk modulus for each of the structures and approximations used. For comparison, the experimental lattice parameter is 2.867 Å and the bulk modulus is 172 GPa [99]. The lattice parameter for the ferromagnetic body centred cubic structure is overestimated in all cases and the bulk modulus is underestimated. For the WSDA the predicted lattice parameter is slightly higher than for the other models and the bulk modulus
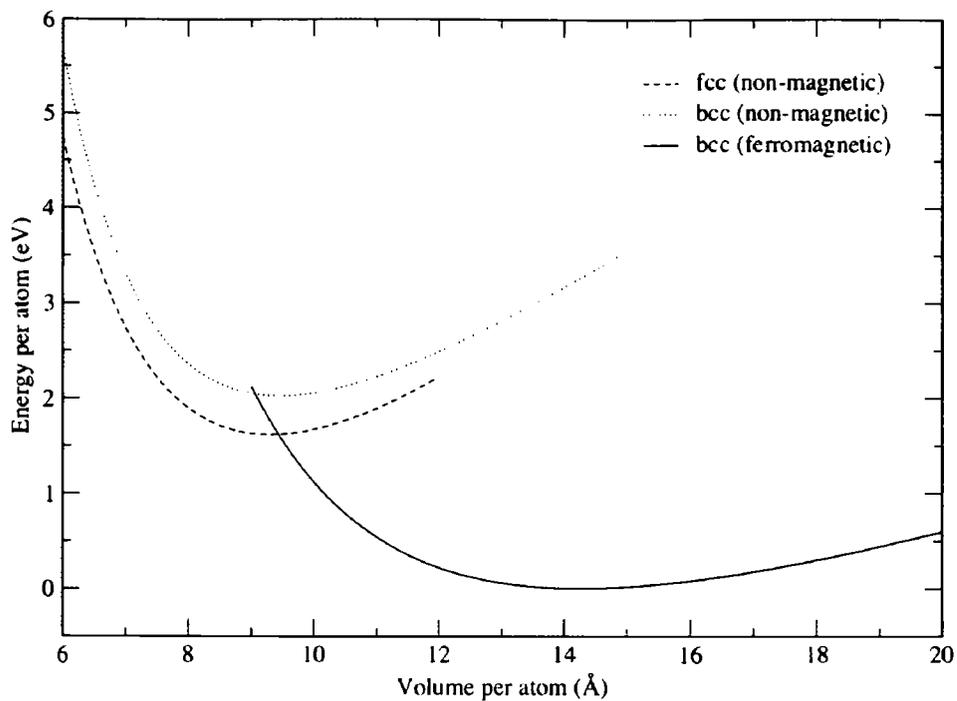
Figure 6.8: Total energy against volume for bulk Fe in a number of structures calculated using the LDA.
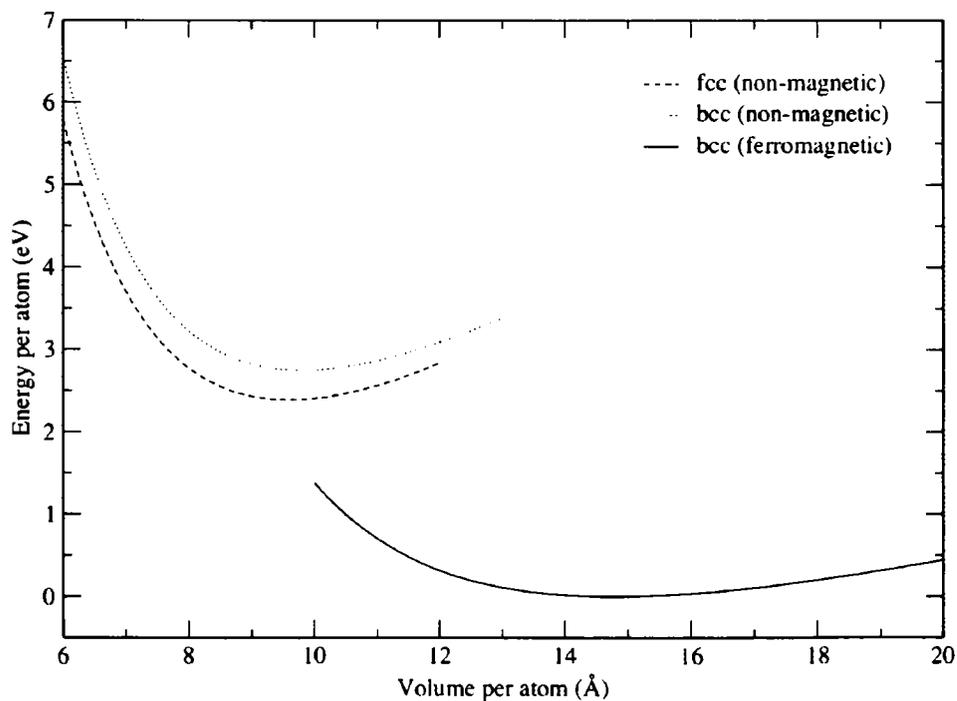
Figure 6.9: As for Figure 6.8 but for the PBE GGA with LDA pseudopotentials.
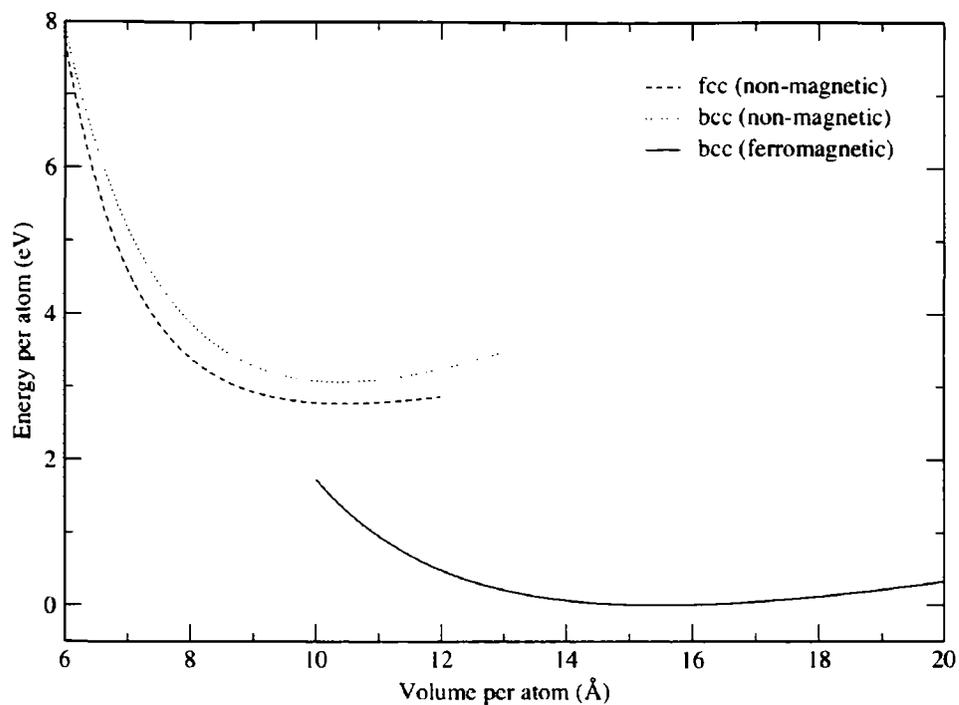
Figure 6.10: As for Figure 6.8 but for the PBE GGA with PBE pseudopotentials.
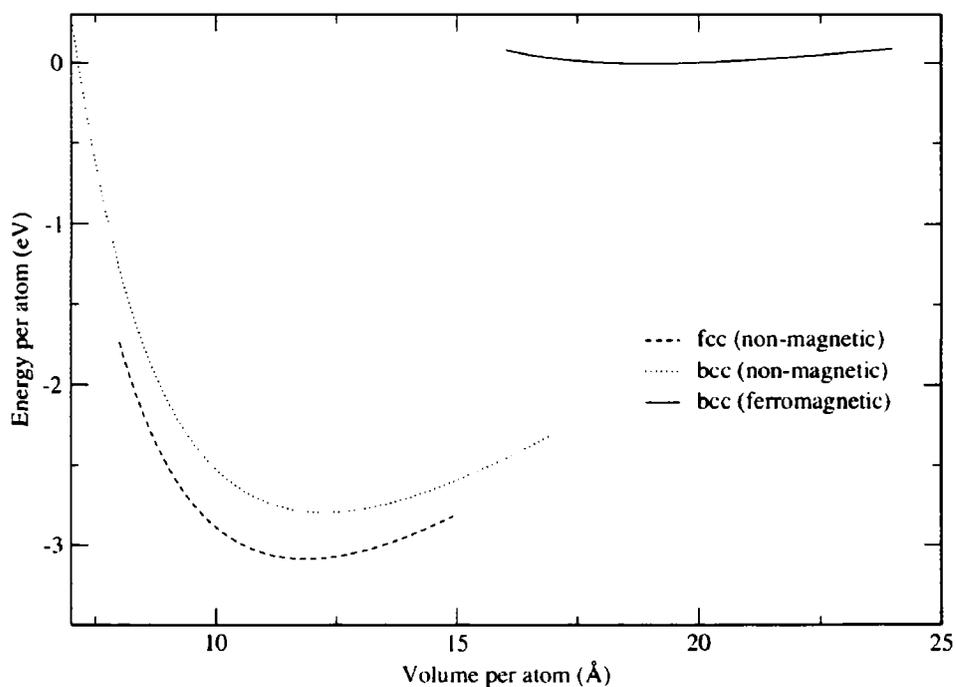
Figure 6.11: As for Figure 6.8 but for our WSDA.

is massively underestimated. This comparison between the WSDA and the other (semi-)local approximations used holds true for the other phases used.

Table 6.5: Equilibrium lattice parameter, a_0, and bulk modulus, B_0, of Fe for selected structures and models. All models use LDA pseudopotentials except where marked with *.

Model	a_0 (Å)			B_0 (GPa)		
	bcc(FM)	bcc(NM)	fcc(NM)	bcc(FM)	bcc(NM)	fcc(NM)
LDA	3.05	2.66	3.34	145	340	378
PBE	3.09	2.70	3.37	130	315	342
PBE*	3.14	2.74	3.47	122	296	178
WSDA	3.36	2.90	3.62	37.8	146	162

The energy volume curves obtained are shown in Figures 6.8 – 6.11. For each of the (semi-)local approximations the correct order, as reported in reference [98], is shown. That the correct order is shown by the LDA is possibly a result of fixing the distribution of spin density in our calculations. The differences for the PBE GGA using LDA and PBE pseudopotentials are minor in this case. The exception is the factor of 2 change in the bulk modulus for the face centred cubic non-magnetic phase. Our implementation of the WSDA fails to predict the correct phase order, in fact, the body centred cubic ferromagnetic phase is predicted to be the least stable. This appears to be because of a redistribution of charge between atomic orbitals, specifically to an excess of charge in the $3d$ orbital of one of the atoms, leading to an excess spin on one atom and a depletion on the other. This is likely to be a result of errors introduced by the model pair-correlation function taking a unphysical on-top value in regions of high electron density. We will discuss this further in section 6.4.

6.3.2 Band Structure of Fe(II) Oxide

Iron(II) oxide is an antiferromagnetic insulator that is commonly found as a black powder, chemical formula FeO. This should not to be confused with rust, which is iron(III) oxide, chemical formula Fe_2O_3. Semi-local functionals typically give FeO a
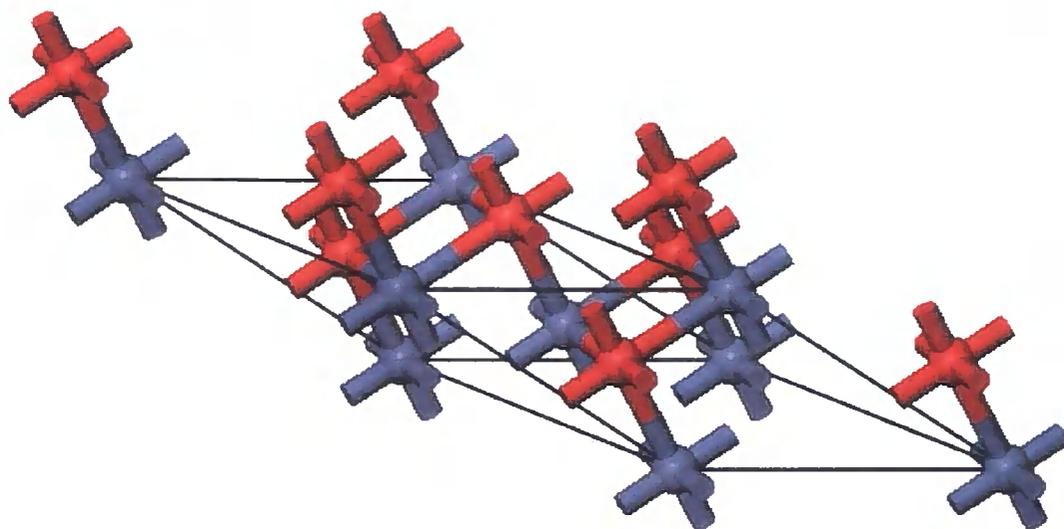
Figure 6.12: The iron(II) oxide structure used in our calculation. The direction of antiferromagnetic alignment is left-right in the plane of this diagram, parallel to the [111] direction in the cubic rock salt structure. Grey atoms represent Fe, red represent O atoms.

zero band gap whereas non-local functionals, particularly those that cancel exactly the self interaction in the Hartree potential [100], can describe the splitting of the d orbitals and predict a gap. This should provide an interesting test for our WSDA.

The crystal structure of FeO is face centered cubic rock salt. However, the antiferromagnetic alignment is along the [111] direction requiring a choice of cell that contains at least two unique Fe atoms in this direction. The rhombohedral centred hexagonal cell shown in Figure 6.12 is the smallest cell that satisfies this requirement. It has lattice parameters $a = b = c = 5.260$ with angles $\alpha = \beta = \gamma = 33.557$. Fe atoms are placed at fractional coordinates (0,0,0) and (0.5,0.5,0.5), and O atoms are placed at (0.25,0.25,0.25) and (0.75,0.75,0.75). In our calculation we use a plane wave kinetic energy cutoff of 1050 eV, we sample the Brillouin zone with a Monkhorst-Pack grid of $6 \times 6 \times 6$ k-points. These criteria converge differences in the total energy to better than 5 meV per atom. We use optimised norm conserving GGA pseudopotentials generated using Opium [101].

The three dimensional band structure was generated along a k-point path of F
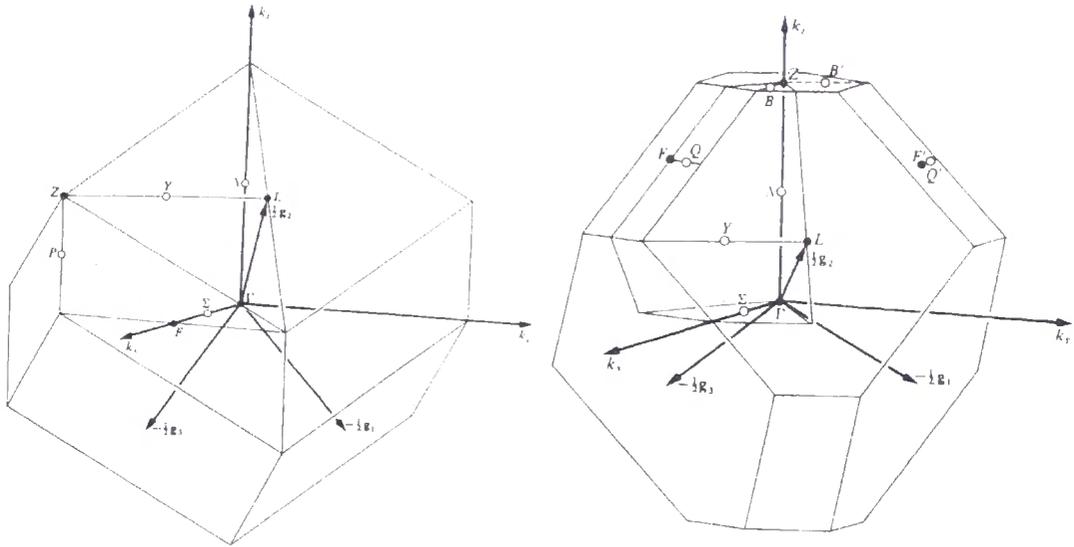
Figure 6.13: Two equivalent representations of the rhombohedral Brillouin zone.

$\rightarrow \Gamma \rightarrow Z \rightarrow L \rightarrow \Gamma$. Two equivalent representations of the Brillouin zone (from reference [102]) are shown in Figure 6.13. As can be seen from Figure 6.14 the WSDA predicts that FeO is metallic, as is found with similar calculations with the LDA [103]. We will now discuss possible explanations for the failings of our WSDA.

6.4 Discussion

In this chapter we have applied the WDA and WSDA with model pair-correlation functions that satisfy the modified cusp condition for the coupling-constant averaged pair-correlation function, $\bar{g}$. Although this is an added physical constraint to our models, the "exact" on-top value of $\bar{g}$ is not given in the homogeneous limit, as was shown in Chapter 5. Even if the correct on-top value was returned in the homogeneous limit, this would not be true in inhomogeneous systems when using the W(S)DA. Because the on-top value is ultimately short range, one expects the true on-top value to be related to the local electron density, however in the W(S)DA the on-top value is solely determined by the weighted density. A possible method for correcting this is given in the following chapter.

There are some simplifying approximations in our implementation of the WSDA
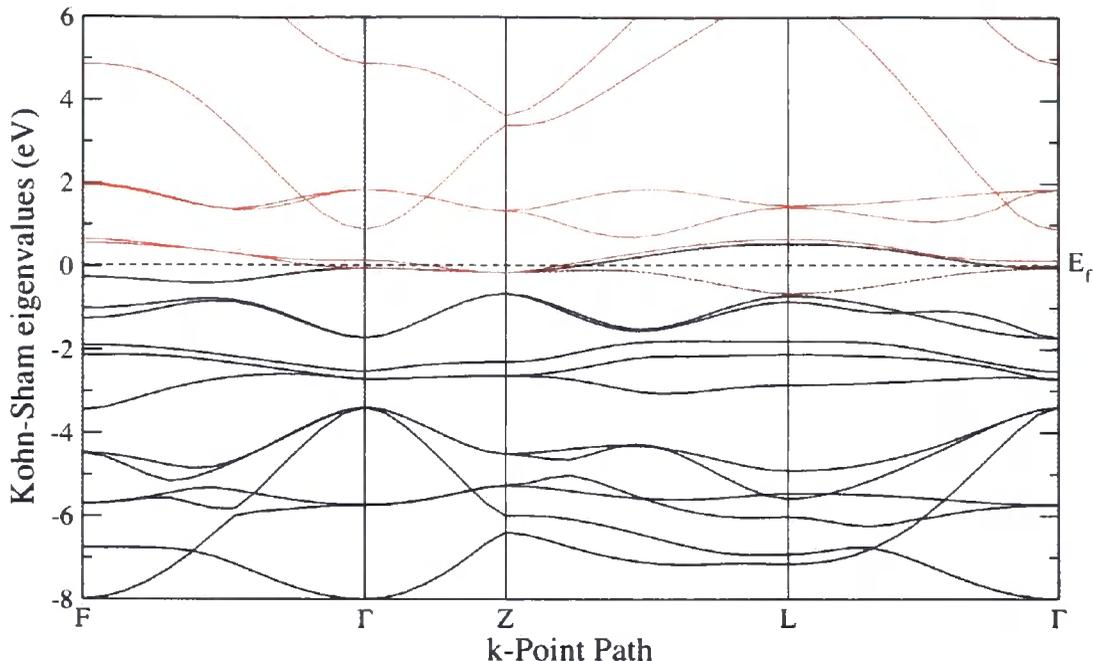
Figure 6.14: Kohn-Sham band structure for FeO. Black lines represent valence bands, red lines represent conduction bands. The dotted line marks the Fermi energy.

that could be the cause of the failings found in our results. First is the matter of the sum rule. In our implementation the weighted up and down densities are determined from the sum rule for parallel spin pairs. These values are then used for the model pair-correlation function used for antiparallel spin pairs. In the uniform limit the sum rule on the antiparallel spin contribution to the exchange-correlation hole is zero, as required. This does not necessarily hold true generally, which can be seen from inspection of equation 4.74. As the C and λ parameters are determined from the homogeneous limit, the combination of F_2^a and F_2^b in general is not zero. However, it is the sum over G-vectors that satisfies the sum rule, so some cancellation may occur. In practice we find that the sum over the full exchange-correlation hole is off from the required -1 by $10^{-3} - 10^{-2}$. Although this is small, it is unclear how much of an effect this may have on the accuracy of physical predictions with our model.

Second, and possibly more concerning, is the failure of our WSDA to correctly

spin resolve the exchange-correlation energy. While the spin resolved pair-correlation function is reasonably approximated in the uniform limit, the energy is not. This is shown in the unphysical on-top values given by our model at (weighted) densities higher than $r_s \approx 0.4$. To refresh the memory, this is because the simple Gaussian used for the parallel spin contribution to the model pair-correlation function overestimates the magnitude of the total exchange-correlation energy at high densities, forcing the antiparallel contribution to become positive and hence λ becomes negative and C positive. As C determines the on-top value, a positive value of C gives a non-physical on-top value greater than 0.5.

The problems caused by this are particularly evident in our calculations on ferromagnetic iron. The high up electron density in this case leads to an error in the exchange-correlation energy contribution for each combination of spin pairs. This means we have a non-physical value of the coupling-constant averaged pair-correlation function at a significant proportion of the simulation space, in this case. We believe the WSDA will be improved by adding the additional constraint that the spin resolved exchange-correlation energy in the homogeneous limit is satisfied.

6.5 Summary

In this chapter we have extended the cusp condition satisfying model for the WDA introduced in Chapter 2 to include the modified cusp condition of Perdew and Wang [61]. This model, and the others introduced throughout this thesis were then applied to selected systems. A detailed study of the bulk properties of silicon and germanium showed that the modified cusp WDA made little difference over the corresponding original WDA model while the application of the spin resolved model pair-correlation function in our WSDA overestimated the lattice parameters and greatly underestimated the bulk moduli. The modified cusp WDA showed a small improvement over LDA for the indirect band gap in silicon but still underestimated by approximately a factor of two. Our WSDA, on the other hand, gave a value for the band gap very close to that found experimentally. All of our models severely underestimate or give a zero direct band gap in germanium. This may be from

including the $3d$ electrons in the pseudopotential [92] or could be an artifact of model pair-correlation functions chosen.

We applied the LDA, modified cusp WDA and modified cusp WSDA to calculate the band gaps for a number of materials in the rock salt and zincblende structures at their experimental lattice parameters. Overall the WSDA provided the best calculations of band gaps, with the differences between those calculated in the LDA and modified CWDA being minor. It is likely that the WSDA would overestimate the equilibrium lattice parameter for each of these materials.

The WSDA was then applied to spin polarised systems of bulk iron and iron(II) oxide. Disappointingly, the WSDA failed to predict the correct phase order for Fe, giving the experimentally most stable ferromagnetic body centred cubic structure as the least stable. The electronic properties of FeO were predicted to be metallic by the WSDA whereas experiment finds the material to be insulating. These failures are most likely because of the breakdown of our model pair-correlation function at high electron densities and the incorrect spin resolution of the exchange-correlation energy.

It would appear that the choice of model pair-correlation function for our initial implementation of the WSDA is too simplistic. However, the framework for describing a spin resolved pair-correlation function in a weighted density scheme is sound. More appropriate model pair-correlation functions based on the homogeneous electron gas would remove the issues of unphysical on-top values of the pair-correlation function and the spin resolution of the exchange-correlation energy. Further refinements to the weighted density approach can be made in symmetrising the model pair-correlation function and controlling the on-top value of the pair-correlation function through the true electron density. We will discuss these and other avenues for refinement in the next chapter. That improved band gaps are produced by even the simple WSDA model we use is promising nonetheless.

Chapter 7

Conclusions and Future Work

Here we will summarise the conclusions of the previous chapters. We will outline issues yet to be resolved in WDA based models and address problems with our choice of model pair-correlation function in the WSDA.

7.1   Summary of Conclusions

Throughout this thesis we have concentrated on improving a non-local approximation to exchange and correlation in density functional theory. In Chapter 1 we discuss the uses of and difficulties in solving the many-electron Schrödinger equation. Density functional theory can be used to make the problem solvable exactly, in principle. The plane wave pseudopotential method for applying DFT is outlined. The formulation of DFT leaves an unknown in the form of the exchange-correlation energy functional. Approximations to exchange-correlation are discussed in Chapter 2 where the WDA is discussed in detail as a non-local approach of modeling the exchange-correlation hole directly. Some of the possible models for the coupling-constant averaged pair-correlation function are discussed. We show that given an appropriate choice of model, excellent results can be obtained for the bulk properties of copper. However there is no method of selecting the "correct" model *a priori*. The models that give good results for the properties of copper do not necessarily give good results for silicon [57] and vice versa. Therefore we look towards improving the model used by satisfying more physical constraints such as the Kimball cusp con-

dition. A method of including the cusp condition is refined and implemented, then applied to determine bulk properties of silicon. These preliminary results suggest that existing WDA models can be improved by satisfying even one extra physical constraint.

Surfaces are systems that one would intuitively think require a non-local treatment of exchange-correlation. In Chapter 3 we successfully demonstrate this by calculating the exchange-correlation hole using the WDA for metal surfaces. A good approximation to an image charge is shown and the importance of finite cell effects is discussed. The WDA is applied to determine a two dimensional section of the potential energy surface for H_2 dissociation on Cu(100). When compared to the LDA, we show that a non-local approximation for exchange-correlation is required to adequately simulate surfaces using DFT.

In Chapter 4 we derive a new framework for model pair-correlation functions in the WDA by including spin resolution. We refer to this as the weighted spin density approximation, WSDA, a fully non-local approach to treating spin polarised systems in the WDA. By spin resolving the model pair-correlation function, we allow for the possibility of a greater number of physical constraints to be satisfied when approximating the exchange-correlation hole.

We compared the spin resolved pair-correlation function for our WSDA in the uniform limit with quantum Monte Carlo data for the homogeneous electron gas in Chapter 5. The on-top values of the pair-correlation function for the homogeneous electron gas were investigated and discussion was made comparing different first principles methods, concluding that definitive work in this area is still to be done. The importance of including the correct modified cusp condition for the coupling-constant averaged pair-correlation function was raised. We amended the model constructed in Chapter 4 to include the modified cusp condition for antiparallel spin pairs. Comparison was made between the full coupling-constant averaged pair-correlation function from our WSDA models and a high quality first principles model produced by Gori-Giorgi and Perdew [81]. This comparison was done at a number of densities and spin polarisations, finding that the long range part agreed well at metallic densities while the short range and on-top value for our model was closer

at lower densities. The correct on-top value of zero is obtained by our model in the fully polarised limit, as long as the electron density is not higher than $r_s \approx 0.4$.

We began Chapter 6 by extending the cusp condition satisfying model derived in Chapter 2 to include the modified cusp condition. These models were then applied for spin unpolarised and polarised systems. A detailed study of the bulk and electronic properties of silicon and germanium was performed. In silicon, the modified CWDA improved a little on the lattice parameter and indirect band gap from the LDA and did slightly worse for the bulk modulus. The WSDA showed a dramatic improvement for the band gap in silicon overestimating the lattice parameter by $\sim 3\%$. The bulk modulus, however, was found to be approximately half that of the experimental value. Similar statements for the CWDA used on germanium can be made, but with a slight worsening of the predicted band gap. The bulk germanium properties predicted by the WSDA were similar in differences to experiment as for the silicon calculation. However, the WSDA predicted a zero band gap for germanium. The failures in predicting the electronic properties of germanium could be because the $3d$ electrons were included in the pseudopotential – the band structure has been found to be sensitive to whether the d electrons are treated as valence or not [92]. Band gaps for a number of materials in the rock salt and zincblende structures were calculated using the LDA, modified CWDA, and WSDA. Overall the WSDA provided the greatest improvements in calculating the band gap. Although not tested, it is likely that our WSDA would overestimate the lattice parameters for these materials. Calculations were also performed on spin polarised systems in the form of bulk iron and iron(II) oxide. In bulk iron, the total energy-volume curves for the non-magnetic body centred cubic and face centred cubic phases were comparable to those calculated with the LDA and PBE GGA. The ferromagnetic body centred cubic phase was predicted to be the least stable by the WSDA, as opposed to being the most stable as found in nature. The band structure in antiferromagnetic iron(II) oxide was found to be metallic, in contrast to the insulating properties found in nature. Possibilities for explaining these failures were briefly discussed.

Our implementation of the WSDA shows promise in improving the predicted band gap in a large number of materials. However there are failings in both the

model used and the implementation that we will now address.

7.2 Implementation of WSDA

We have shown in the previous chapter that the implementation and model pair-correlation function used in our WSDA still requires improvement. However, the underlying framework developed in this thesis for a fully non-local WSDA remains valid. Furthermore, using a spin resolved model pair-correlation function allows for more physical constraints to be satisfied by the model. This is especially true in comparison to the suggestion by Gunnarsson and Jones [55] of neglecting spin polarisation completely from the model pair-correlation function (apart from its inclusion in the LSDA exchange-correlation energy density) when applying the WDA to spin polarised systems.

The main problems in our WSDA are the choice of model pair-correlation function and the failure to satisfy the sum rule on the exchange-correlation hole. Problems with the choice of model can be resolved by using the spin resolved coupling-constant averaged pair-correlation function for the homogeneous electron gas. Although explicit forms are not currently available, the parts required to do so are available through a combination of references [81] and [104].

Satisfying the sum rule for the exchange-correlation hole reduces to the way the weighted density is used. In general, if the weighted density is determined solely from the sum rule for parallel spin pairs, as it is in our implementation, then the zero sum rule for the antiparallel spin pairs cannot be satisfied. However, there is no need for a single weighted (spin) density parameter, one can instead have separate weighted density parameters for parallel and antiparallel spin contributions, respectively. This does cause an implementation problem for determining the weighted density for antiparallel spins, essentially a two dimensional logarithmic grid would have to be searched through to select the weighted spin densities that satisfy the sum rule and spin resolved exchange-correlation energy. Construction of this 2D grid would likely be prohibitively expensive. To avoid this issue, the model could be recast in terms of the spin polarisation parameter of the true electron density so that there is only

a single weighted density parameter for antiparallel spin pair contributions.

7.3   A New Model Pair-Correlation Function

It has been shown that the WDA shows promise, but still suffers from a number of problems that come back to fitting physical constraints. The WDA does not return correct on-top values for the coupling-constant averaged pair-correlation function. This applies even if one uses the coupling-constant averaged pair-correlation function from the homogeneous electron gas as the basis for the WDA. In this case the correct on-top value will only be returned in the slowly varying limit because of the model's dependence on the weighted density parameter. Burke, Perdew and Ernzerhof [105] have shown that the success of the LDA and other semi-local functionals can be related to correct, or nearly correct on-top values being returned. Physically this follows from the on-top value being the test of correct short range exchange-correlation interactions.

Upon examining our framework for models used in the WDA, we can enforce the correct on-top value through the parameter C. Instead of depending on the weighted density, we can let it be determined from the electron density at each point in space. In order to retain the sum rule on the exchange-correlation hole and the energy in the uniform limit, we take κ from the model incorporating the Kimball cusp condition and allow it to vary with the weighted density. For the model with the corrected modified cusp condition on the coupling-constant averaged pair-correlation function, we must treat the parameter H in the same way as C and have it depend on the local electron density. It should be pointed out that all the ingredients of this WDA based method are determined from physical constraints, so the method remains non-empirical. Below we will suggest a possible implementation within our existing framework for the modified cusp condition in the spin unpolarised case and using the Gaussian function as the base for the model pair-correlation function.

We follow from equation 6.3 for the model pair-correlation function satisfying the modified cusp condition:

$$
\begin{aligned}
G^{\text{WDA}}[|r - r'|; \tilde{n}(r), n(r)] &= C(n(r))f\left(\frac{|r - r'|}{\lambda(\tilde{n}(r))}\right) \\
&+ H(n(r))(C(n(r)) + 1)|r - r'|f\left(\frac{|r - r'|}{\lambda(\tilde{n}(r))\kappa(\tilde{n}(r))}\right).
\end{aligned}
\tag{7.1}
$$

Here, the function $f(u) = e^{-u^2}$, is the simple Gaussian model. The on-top value and the on-top derivative are determined solely through C and H, the latter can be determined from Perdew and Wang's [61] model or the more recent model of Gori-Giorgi and Perdew [81]. To determine λ and κ we take the homogeneous limit of the exchange-correlation energy and the sum rule for the exchange-correlation hole. In this case, with the simple Gaussian model, we obtain a ninth order polynomial in λ. We have not tested if this polynomial is poorly conditioned for finding roots numerically.

A more straightforward solution could be to use a model function based on the homogeneous pair-correlation function. This would then return the correct energy in the uniform limit while allowing us to control the on-top value from the electron density rather than the weighted density. An implementation of either or both of these methods is beyond the scope of this thesis. However, the general success of semi-local exchange-correlation functionals that give on-top values from the homogenous electron gas [105] leads us to believe that this extension to the WDA should be investigated further. The same principles can be applied to the WSDA.

7.4 Remaining WDA Problems

There are other remaining problems with the WDA approach. Mazin and Singh [106] demonstrate that simple WDA model functions do not give the correct exchange-correlation dielectric response, i.e. the second derivative of the exchange-correlation energy, $\delta^2 E_{\text{xc}}/\delta n(r)\delta n(r')$. This is a failing for the LDA and GGAs also [106]. They provide a method of testing model pair-correlation functions for satisfying this criteria and suggest a method of altering existing models.

In general WDA implementations are vastly more computationally expensive than (semi-)local approximations. The single most time consuming step is in determining the weighted density. In our implementation this could be done more efficiently by performing the sums over G-vectors within an irreducible wedge, rather than the entire simulation cell, when a system has some symmetry. Care would have to be taken in a parallel implementation of this scheme.

Generating consistent WDA pseudopotentials is a subtle task. It is, however, quite desirable as mixing the exchange-correlation functional used for the self consistent calculation with another approximation to construct the pseudopotentials can lead to some discrepancies [107, 108]. The range of the model pair-correlation function is comparable to the size of atoms, so the WDA would treat core electrons with as much importance as valence electrons. A shell partitioning scheme has been suggested [54, 62] in which the core electrons are treated with the LDA and the valence electrons with the WDA. If the exact pair-correlation function for a particular system was used the intershell interactions would be correctly described [109] and shell partitioning would not be required. This mixture of local and non-local approximations is, in our opinion, counter to the goal of attaining a purely *ab initio* approximation for exchange-correlation. Improved WDA model pair-correlation functions that fit more physical constraints could approximate the true exchange-correlation hole accurately and remove the issue of shell partitioning. This could be investigated by using the WDA in all electron calculations.

Finally we will discuss the problem of symmetry in the model pair-correlation function. As discussed previously, the true coupling-constant averaged pair-correlation function is symmetric upon interchange of particle positions. The model pair-correlation function used in the WDA is based on radial symmetry, but only a single weighted parameter, so the interchange symmetry does not hold. This leads to the asymptotic behaviour of the exchange-correlation potential differing from the correct limit by a factor of two.

Suggestions based on symmetrising the model by replacing the $\lambda(\tilde{n}(r))$ parameter with a combination of $\lambda(\tilde{n}(r))$ and $\lambda(\tilde{n}(r'))$ have been made and shown to be unphysical in reference [72]. Wu, Cohen and Singh suggest an alternative method of con-

structing a symmetrised WDA [68], by simply replacing the model pair-correlation function with a sum of two model functions of the original type. One model function depends on the weighted density at r while the other depends on the weighted density at r':

$$G^{\text{SWDA}}(r, r') \equiv \frac{1}{2} \left\{ G^{\text{WDA}}[|r - r'|; \tilde{n}(r)] + G^{\text{WDA}}[|r - r'|; \tilde{n}(r')] \right\}. \tag{7.2}$$

This then requires a more complicated self consistent iteration scheme to determine the weighted density at all points. It is unclear how physical the resulting model symmetrised pair-correlation function and associated exchange-correlation hole would compare to, say, quantum Monte Carlo data for a real system.

7.5 Closing Remarks

In this thesis we have demonstrated that use of non-local functionals such as the WDA is promising, particularly in the case of surfaces, but still needs refinement in several areas. A new framework for modeling the coupling-constant averaged pair-correlation with spin resolution allows more physical constraints to be applied than with previous models. This can be further refined by resolving the parallel spin contributions into separate exchange and correlation parts. We feel that the approach of refining the model coupling-constant averaged pair-correlation function used in the WDA through satisfying physical constraints will lead to a definitive implementation of the WDA. With improvements to the algorithms used and increased computational capability, such an implementation of the WDA could become an invaluable tool in the field of electronic structure calculations. Non-local functionals are a strong alternative to improving approximations of exchange-correlation over the popular "Jacob's ladder" [110] route.

Appendix A

Integrals Used in WDA
Implementation

In the implementation of the WDA that we use, we have a number of $F_x(q)$ functions that are related to the spherical Fourier transform of the model pair-correlation function used and its derivatives. Here we will provide general forms for the $q = 0$ limit of these functions for each of the four groups of model described in Chapter 2. These are then used to numerically construct the full $F_x(q)$.

In general, for a model pair-correlation function $f(u)$, we have:

$$F_1(0) = \int_0^\infty u f(u) du, \tag{A.1}$$

$$F_2(0) = \int_0^\infty u^2 f(u) du, \tag{A.2}$$

$$F_3(0) = \int_0^\infty u^2 \frac{\partial f(u)}{\partial u} du, \tag{A.3}$$

$$F_4(0) = \int_0^\infty u^3 \frac{\partial f(u)}{\partial u} du. \tag{A.4}$$

The general form for each of the models is given in section 2.3.

152

A.1 Gaussian

For the Gaussian (and fourth order Gaussian) models we will make much use of the following standard integral:

$$\int_0^\infty u^n e^{-\left(\frac{u}{\kappa}\right)^p} du = \frac{1}{p} \kappa^{\frac{n+1}{p}} \Gamma\left(\frac{n+1}{p}\right),$$

(A.5)

which is paraphrased from reference [111]. We include κ for use in the cusp modifications that we will tackle later. For now, we take $\kappa = 1$ and set $p = 2$ for the Gaussian. $\Gamma(z)$ is, of course, the well known Gamma function. The general relations for the $F_x(0)$ values are:

$$F_1(0) = \frac{1}{2} \sum_{n=0,even}^{N} \frac{\Gamma\left(\frac{n+2}{2}\right)}{\frac{n}{2}!} = \frac{\frac{N}{2}+1}{2},$$

(A.6)

$$F_2(0) = \frac{1}{2} \sum_{n=0,even}^{N} \frac{\Gamma\left(\frac{n+3}{2}\right)}{\frac{n}{2}!},$$

(A.7)

$$F_3(0) = -\frac{\Gamma\left(\frac{N+4}{2}\right)}{\frac{N}{2}!},$$

(A.8)

$$F_4(0) = -\frac{\Gamma\left(\frac{N+5}{2}\right)}{\frac{N}{2}!},$$

(A.9)

where N is the order of the polynomial that is multiplied with the Gaussian.

A.2 Fourth Order Gaussian

The general forms for the fourth order Gaussian based models are similar:

$$F_1(0) = \frac{1}{4} \sum_{n=0,even}^{N} \frac{\Gamma\left(\frac{2n+2}{4}\right)}{\frac{n}{2}!}, \tag{A.10}$$

$$F_2(0) = \frac{1}{4} \sum_{n=0,even}^{N} \frac{\Gamma\left(\frac{2n+3}{4}\right)}{\frac{n}{2}!}, \tag{A.11}$$

$$F_3(0) = -\frac{\Gamma\left(\frac{2N+6}{4}\right)}{\frac{N}{2}!}, \tag{A.12}$$

$$F_4(0) = -\frac{\Gamma\left(\frac{2N+7}{4}\right)}{\frac{N}{2}!}, \tag{A.13}$$

except that here, the order of the preceding polynomial is $2N$.

A.3 Lorentzian

For the Lorentzian-like functions, we make use of a standard integral from reference [111]:

$$\int_0^\infty \frac{u^{\mu-1}}{1+u^\nu} du = \frac{\pi}{\nu} \text{cosec}\left(\frac{\mu\pi}{\nu}\right). \tag{A.14}$$

The general relations for the $F_x(0)$ values are:

$$F_1(0) = \frac{\pi}{n}\text{cosec}\left(\frac{2\pi}{n}\right),$$
(A.15)

$$F_2(0) = \frac{\pi}{n}\text{cosec}\left(\frac{3\pi}{n}\right),$$
(A.16)

$$F_3(0) = 2F_1(0),$$
(A.17)

$$F_4(0) = 3F_2(0),$$
(A.18)

where n is the order of the Lorentzian-like function used.

A.4   Gunnarsson-Jones

For the Gunnarsson and Jones-like functions, we make use of a standard integral from reference [111]:

$$\int_0^\infty u^{\nu-1}\left(1 - e^{-u^p}\right)du = -\frac{1}{|p|}\Gamma\left(\frac{\nu}{p}\right).$$
(A.19)

The general relations for the $F_x(0)$ values are:

$$F_1(0) = -\frac{1}{n}\Gamma\left(-\frac{2}{n}\right),$$
(A.20)

$$F_2(0) = -\frac{1}{n}\Gamma\left(-\frac{3}{n}\right),$$
(A.21)

$$F_3(0) = -\left(\frac{2}{n}\right)!,$$
(A.22)

$$F_4(0) = -\left(\frac{3}{n}\right)!,$$
(A.23)

where n is the power in the exponential part of the Gunnarsson and Jones-like function used. Of course, non-integer factorials can be evaluated by relating the Gamma function to the factorial, $\Gamma(n + 1) = n!$.

A.5 Cusp Condition Integrals

In our implementation of a model pair-correlation function that satisfies the (modified) Kimball cusp condition, we introduce a second function $f^b(u, \kappa)$ to the model. Here we will give the integrals for the simple Gaussian and fourth order Gaussian functions introduced in Chapter 2. For the Gaussian based model, $f^b(u, \kappa) = ue^{-u^2/\kappa^2}$. The corresponding $F_x^b(0)$ values are therefore:

$$F_1^b(0) = \frac{\kappa^3}{2}\Gamma\left(\frac{3}{2}\right) = \frac{\sqrt{\pi}}{4}\kappa^3, \tag{A.24}$$

$$F_2^b(0) = \frac{\kappa^4}{2}\Gamma\left(\frac{4}{2}\right) = \frac{\kappa^4}{2}, \tag{A.25}$$

$$F_3^b(0) = F_1^b(0) - \kappa^3\Gamma\left(\frac{5}{2}\right) = F_1^b(0) - \kappa^3\frac{3\sqrt{\pi}}{4} = -2F_1^b(0), \tag{A.26}$$

$$F_4^b(0) = F_2^b(0) - \kappa^4\Gamma\left(\frac{6}{2}\right) = F_2^b(0) - 2\kappa^4 = -\frac{3}{2}F_2^b(0), \tag{A.27}$$

where κ is set to a constant value for each model, as discussed in Chapter 2. Similarly, for the fourth order Gaussian based model, where $f^b(u, \kappa) = ue^{-u^4/\kappa^4}$, we have:

$$F_1^b(0) = \frac{1}{4}\kappa^3\Gamma\left(\frac{3}{4}\right), \tag{A.28}$$

$$F_2^b(0) = \frac{1}{4}\kappa^4\Gamma\left(\frac{4}{4}\right) = \frac{\kappa^4}{4}, \tag{A.29}$$

$$F_3^b(0) = F_1^b(0) - \kappa^3\Gamma\left(\frac{7}{4}\right), \tag{A.30}$$

$$F_4^b(0) = F_2^b(0) - \kappa^4\Gamma\left(\frac{8}{4}\right) = F_2^b(0) - \kappa^4 = -\frac{3}{4}F_2^b(0), \tag{A.31}$$

A.6 WSDA – Antiparallel Spin Pair Model

Finally, we use a slightly different Gaussian based model in the model pair-correlation function for antiparallel spin pairs within our implementation of the WSDA. We suggested, in Chapter 4, that $f^b(u, \kappa) = (u + u^2)e^{-u^2/\kappa^2}$. The $F_x^b(0)$ values are therefore:

$$F_1^b(0) = \frac{\sqrt{\pi}}{4}\kappa^3 + \frac{\kappa^4}{2}, \tag{A.32}$$

$$F_2^b(0) = \frac{\kappa^4}{2} + \frac{3\sqrt{\pi}\kappa^5}{8}, \tag{A.33}$$

$$F_3^b(0) = \frac{\sqrt{\pi}\kappa^3}{2} + \kappa^4, \tag{A.34}$$

$$F_4^b(0) = \frac{3\kappa^4}{2} + \frac{9\sqrt{\pi}\kappa^5}{8}. \tag{A.35}$$

Appendix B

Other Publications

Work not included in this thesis that has been published or will be submitted for publication:

Andrew J. Robbins, William T. K. Ng, D. Jochym, Thomas W. Keal, S. J. Clark, David J. Tozer and Paul Hodgkinson, *Combining insights from solid-state NMR and first principles calculation: applications to the ^{19}F NMR of octafluoronaphthalene*, Phys. Chem. Chem. Phys., **9**, 2389–2396, (2007).

Robin K. Harris, D. B. Jochym, Vadim E. Zorin, Anuji Abraham, S. J. Clark, D. J. Tozer, P. Hodgkinson, *A study of the value and limitations of GIPAW computations of chemical shifts for organic solids*, to be submitted.

Combining insights from solid-state NMR and first principles calculation: applications to the ^{19}F NMR of octafluoronaphthalene†

Andrew J. Robbins,[a] William T. K. Ng,[a] Dominik Jochym,[b] Thomas W. Keal,[a] Stewart J. Clark,[b] David J. Tozer[a] and Paul Hodgkinson*[a]

Advances in solid-state NMR methodology and computational chemistry are applied to the ^{19}F NMR of solid octafluoronaphthalene. It is demonstrated experimentally, and confirmed by density functional theory (DFT) calculations, that the spectral resolution in the magic-angle spinning spectrum is limited by the anisotropy of the bulk magnetic susceptibility (ABMS). This leads to the unusual observation that the resolution improves as the sample is diluted. DFT calculations provide assignments of each of the peaks in the ^{19}F spectrum, but the predictions are close to the limits of accuracy and correlation information from 2-D NMR is invaluable in confirming the assignments. The effects of non-Gaussian lineshapes on the use of 2-D NMR for mapping correlations of spectral frequencies (e.g. due to the ABMS) are also discussed.

1. Introduction

Octafluoronaphthalene ($C_{10}F_8$) [or perfluoronaphthalene] has been regularly used as a model system in the development of ^{19}F solid-state NMR. Mehring et al.[1] used multi-pulse RF decoupling on static (non-spinning) samples to resolve the two chemically distinct fluorine types (i.e. α and β), while Harris et al.[2] combined multi-pulse decoupling with slow magic angle-spinning (CRAMPS, combined rotation and multi-pulse spectroscopy) to resolve the two resonances into pairs of signals corresponding to the four crystallographically distinct fluorine sites in the crystal structure, Fig. 1b.

The structural chemistry of octafluoronaphthalene is intriguing, as the structure at room temperature is not well-defined by current techniques. It is thought to adopt the same structure as the normal naphthalene structure above 281.5 K,[3] but the extent of diffuse scattering in X-ray and neutron diffractograms, combined with the relatively poor quality of the resulting fits (as measured by the statistical R factors), indicates that considerable disorder (static or dynamic) is present. Based on a drop in the width of the static ^{19}F spectrum (as measured by its second moment), previous NMR studies[1] suggest that this disorder is dynamic, with the molecules re-orienting about the C_2 axis perpendicular to the molecular plane. This is consistent with the proposed X-ray structure, Fig. 1b, in which fluorine sites related by the molecular centre of inversion are identical.

Fast magic–magic spinning is now used routinely to obtain resolved solid-state NMR spectra from abundant nuclei such as ^{1}H and ^{19}F which are broadened by the extensive dipolar couplings between the abundant spins.[4,5] As shown in Fig. 1c,

the fast MAS spectrum clearly resolves the four sites into two pairs corresponding to α sites (attached to carbons 1, 4, 5 and 8) and β sites (attached to carbons 2, 3, 6 and 7). The α and β pairs are readily assigned, as shown, on the basis of solution-state shift values.[2] Unfortunately it is not possible to assign the individual resonances to F sites in the crystal structure from these NMR data alone.

In this paper we revisit octafluoronaphthalene both to complete the assignment of its ^{19}F spectrum and to examine the factors that affect the ^{19}F spectral resolution. Unusually, the resolution is observed to depend on the sample concentration, and this effect is shown to be a consequence of the large anisotropy of the bulk magnetic susceptibility (ABMS) of this solid. Section 3 discusses the consequences of this ABMS broadening for 2-D NMR .

In section 4, Kohn–Sham density functional theory (DFT) is used to calculate the NMR chemical shifts of octafluoro-naphthalene, using both structures as derived from X-ray studies and from DFT energy minimisation. The agreement between calculated and experimental shifts is not quantitative, but the combination of 2-D NMR experiments and DFT finally permits the full assignment of the NMR spectrum, allowing each of the peaks in the solid-state NMR spectrum to be identified with specific sites in the crystal structure.

2. ^{19}F resolution under fast magic-angle spinning

Fast rotation of solid samples about an axis inclined at the "magic angle" of 54.7° with respect to the magnetic field axis effectively averages the dipolar couplings that are largely responsible for broadening the solid-state NMR spectra of abundant nuclear spins such as ^{1}H or, in this case, ^{19}F. Particularly at high static magnetic fields (corresponding to ^{1}H NMR frequencies of about 400 MHz or higher) useful ^{1}H resolution can be obtained at spinning rates in excess of about 20 kHz.[4] We have recently analysed the factors that determine resolution in ^{1}H MAS experiments and demonstrated that

[a] Department of Chemistry, University of Durham, South Road, Durham, UK DH1 3LE
[b] Department of Physics, University of Durham, South Road, Durham, UK DH1 3LE
† The HTML version of this article has been enhanced with colour images.
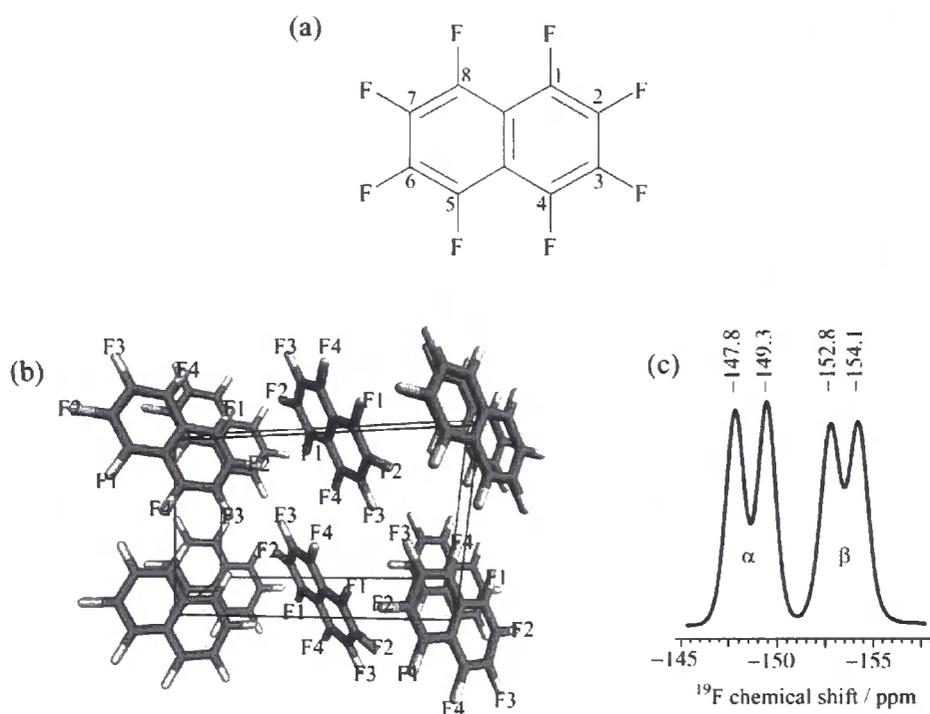
Fig. 1 (a) Molecular structure of octafluoronaphthalene, (b) Ambient temperature crystal structure (reference code OFNAPH01 from the Cambridge Structural Database). (c) Ambient temperature ^{19}F MAS spectrum (MAS spin rate of 22 kHz and ^{19}F Larmor frequency of 470 MHz), showing four clearly resolved sites.

proton linewidths can be understood in terms of a "homogeneous" linewidth that is determined by the strength and nature of the dipolar coupling network relative to the sample spinning rate, and an "inhomogeneous" linewidth which is independent of sample spinning.[5]

As part of a related study exploring ^{19}F resolution in solid-state NMR, we have revisited octafluoronaphthalene (OFN) as an example of a system that was expected to exhibit substantial line-broadening in its ^{19}F spectrum due to the large magnetic susceptibility broadenings caused by aromatic ring currents. Magic-angle spinning is effective at removing local isotropic variations of the bulk susceptibility, χ, due to the presence of interfaces etc. (which may help to explain why significantly better resolution was obtained in the multi-pulse decoupling experiments involving magic-angle spinning[2] compared to those on static samples[1]). However, MAS is only partially successful if the χ is anisotropic and so is time-dependent under spinning.[6–8] This residual broadening is determined by $\Delta\chi$—the anisotropy of the bulk magnetic susceptibility (ABMS) of the material. As the effect of $\Delta\chi$ is only partially averaged by magic-angle spinning, an individual crystallite experiences an average bulk susceptibility over the rotation period, $\langle\Delta\chi\rangle$, which will depend on its orientation (with respect to the rotation axis). Hence the lineshape of a powder sample will be broadened.

As a result of the packing in the naphthalene structure, we expect both $C_{10}H_8$ and $C_{10}F_8$ to have relatively large values of $\Delta\chi$ and so have broadened lines in their NMR spectra. This is confirmed by DFT calculations of $\Delta\chi$ (see below for more details of the calculations) which predict an anisotropy of the

(volume) magnetic susceptibility of $\Delta\chi \approx 1.6 \times 10^{-7}$ for octafluoronaphthalene. This can be compared to a prediction of -2.7×10^{-8} for an analogous DFT calculation on the β-form of testosterone. Testosterone was used as a comparison since the ^{13}C linewidths for typical crystalline steroids are generally very sharp, which is indicative of little inhomogeneous broadening. These $\Delta\chi$ values are expressed (as is conventional) in unrationalised cgs units and so we define an SI "ABMS linebroadening factor", $|4\pi\Delta\chi|$, which corresponds to 2.0 ppm for octafluoronaphthalene and 0.33 ppm for testosterone. The final effect of $\Delta\chi$ depends non-trivially on the details of crystallite morphology and sample packing and the effect of averaging by the sample spinning.[8] However, these values of $|4\pi\Delta\chi|$ do coincide reasonably well with experimentally observed linewidths in the two systems, and other calculations on a number of molecular crystals confirm this strong correlation between calculated ABMS factors and experimental linewidths. This broadening could be removed by working with monocrystals, but it is rarely practical to grow crystals of sufficient size for NMR spectroscopy. Alternatively, the effects of $\Delta\chi$ can be weakened by diluting the sample by a material with a much lower or zero $\Delta\chi$.[6]

Physical mixtures of different relative composition of octafluoronaphthalene and sodium chloride (zero ABMS) were weighed out, ground together in a pestle and mortar, and firmly packed into 2.5 mm o. d. zirconia rotors. ^{19}F NMR MAS spectra were acquired on a Varian/Chemagnetics InfinityPlus spectrometer operating at 470 MHz for ^{19}F at a spinning rate of 22 kHz. As the linewidth is dominated by inhomogeneous factors, there was no useful improvement in

resolution at increasing spinning rates towards the maximum specified for the probe (30 kHz). A lower spin rate was used throughout to avoid unnecessary sample heating (a typical increase of 50 °C in sample temperature due to frictional heating from spinning close to the probe limit would bring octafluoronaphthalene uncomfortably close to its melting point of 87–88 °C). Chemical shifts were referenced to the fluorine peak in Teflon which is at −123.2 ppm relative to the primary reference of $CFCl_3$. Natural linewidths were measured by fitting a 75% Gaussian/Lorentzian lineshape and the peak widths at half height of the four resonances determined.

Spin-echo experiments were performed to estimate the "homogeneous" component of the linewidth. [19]F spectra were recorded as a function of the spin-echo delay, 2τ, using ten increments up to a time of 1.7 ms, and peak intensities extracted by fitting as above. The resulting decays (intensity vs. spin-echo delay) fitted well to single exponentials with effective "T_2" values of about 2.4 ms. It is important to stress that the magnetisation decay is largely determined by the dipolar coupling network and its interaction with magic-angle spinning rather than true relaxation. This decay time constant corresponds to a linewidth contribution of about 180 ± 10 Hz. As would be expected, the spin-echo decay rates were independent of the mixture composition within experimental error.

Fig. 2 shows the natural (full width at half maximum) of the four ^{19}F resonances as a function of composition. The composition is expressed as a volume fraction (using the known sample densities of NaCl, 2.16 g cm^{-3}, and OFN, 2.07 g cm^{-3}) which is a more natural metric for expressing bulk susceptibility effects on mixtures, although it does not account for the volume taken up by voids, which may have a measurable impact on bulk susceptibility broadenings.[9] The linewidths for the different resonances are expected to be essentially identical, reflecting their very similar environments, and contributions from the bulk susceptibility will be strictly identical across the unit cell. The variation in linewidth between the resonances is most likely to result from the difficulty of fitting overlapping lineshapes when the lineshape function is

not well defined. The spread of values is therefore useful as an indicator of the error bar on the fitted peak widths rather than revealing any fundamental differences between the four resonances.

Analogous effects of composition on linewidths have been observed previously for ^{13}C linewidths by VanderHart et al.,[6] with the effect of adding a material with a large ABMS (hexamethylbenzene, HMB) on linewidths of samples with a low ABMS (adamantane) being considered. In their example, the adamantane linewidths were approximately doubled in a 50:50 mixture of adamantane/HMB in comparison to a pure adamantane sample, while the relative effect on the much broader HMB linewidths was considerably smaller. In this case we are interested in the line-narrowing effect of adding a material with a low ABMS to a system with large susceptibility broadenings. Here we find that even a 50:50 dilution considerably reduces the observed linewidth, which reaches a minimum when the sample is diluted to 10–20%. The linewidth appears to slightly increase in the limit of very high dilution, but the lineshape fitting becomes increasingly unreliable as the signal to noise increases at these low dilutions and so this effect is unlikely to be significant.

The minimum linewidth of about 400 Hz is significantly still larger than the limit of about 180 Hz set by the homogeneous linewidth, indicating that substantial inhomogeneous broadenings are present at all dilutions. Although other sources of inhomogeneous broadenings, such as chemical shift distributions caused by poor sample crystallinity cannot be dismissed, it is likely that susceptibility effects are still at work. As discussed in detail in ref. 6, an elliptically-shaped crystallite in a uniform external magnetic field (e.g. surrounded by a uniform material with zero ABMS) will show zero ABMS broadening under magic-angle spinning. Broadenings will be observed, however, if the crystallite deviates from this ideal shape or if its surroundings are not isotropic. The exact broadening will depend on the interaction between these factors. Since deliberate dilution of samples is not a very practical route to improved resolution, we have not attempted to disentangle these factors. Moreover different behaviour has been observed in other cases where dilutions of less than 10% were required for significant linewidth reductions.[10]

It is encouraging to note, however, that sample dilution can have favourable effects on the resolution (and hence sensitivity) of solid-state NMR spectra. The ability to detect low concentrations of active ingredients in formulated products, for instance, is of great interest.[11] Fortunately typical excipient materials, such as lactose, do not exhibit significant susceptibility broadenings (as observed in their ^{13}C NMR spectra) and so will help to reduce overall ABMS broadenings for active ingredients with large $\Delta\chi$ values.

3. 2-D lineshapes in correlation spectra

It has recently been demonstrated that lineshapes in correlation spectra are often limited by the homogeneous linewidth alone (rather than the total linewidth), allowing considerably more information to be obtained from inhomogeneously broadened spectra than might be anticipated.[12] The frequency shifts due to ABMS at different sites in the same crystallite will
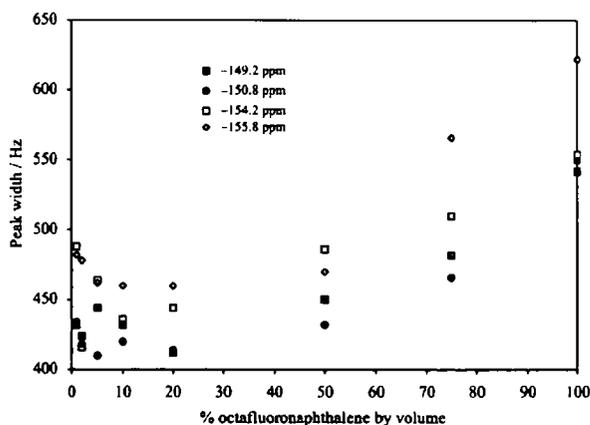
Fig. 2 Full-width-at-half-maximum linewidths for the ^{19}F resonances of octafluoronaphthalene as a function of sample composition. Filled symbols are used for the α sites and open symbols for the β fluorines.

be 100% correlated. This should be apparent in 2-D spectra as an elongation of the peak shape along the diagonal of the spectrum.

Having confirmed that ABMS broadenings made a substantial contribution to the ^{19}F linewidths, we then obtained homonuclear correlation spectra with the double purpose of assisting the assignment of the ^{19}F spectrum and looking for the characteristic peak shapes expected from strongly correlated inhomogeneous broadenings.

2-D ^{19}F homonuclear correlation spectra were obtained from octafluoronaphthalene using the EXSY/NOESY[13] pulse sequence and a short mixing time of 2.3 ms. The presence of off-diagonal peaks in Fig. 3a indicates that magnetisation transfer has occurred between fluorine sites. The correlations observed between α and β resonances cannot be due to physical site exchange due to motion since this will not mix chemically-distinct sites. Hence this transfer must be due to "spin diffusion" *via* the dipolar couplings between close spins. The couplings between adjacent α and β sites are significantly stronger than between more remote α and β pairings. This is true even when intermolecular couplings are included by using the XRD crystal structure to compute the root-sum-square coupling between a given spin and all its neighbours of a given type.[14] As a result, the pattern of off-diagonal peaks between α and β resonances allows a clear connection to be made between peaks at −147.8 and −152.8 ppm, and also the peaks at −149.3 and −154.1 ppm. Hence the magnetisation exchange experiment establishes a *relative* assignment of the four ^{19}F resonances. However it does not provide a full assignment since the two α/β pairs cannot be assigned to crystal sites using this NMR information alone. Note that similar proximity relationships could be obtained, in principle, using other 2-D NMR techniques. For instance, radio-frequency driven recoupling (RFDR)[15] has previously been used to study F–F proximity in fluoropolymers.[16,17] EXSY/NOESY was used in this case as the absence of RF pulses during the mixing time in this simple three-pulse sequence avoids any unwanted interactions between RF irradiation and the substantial molecular motion that was known to be present.

The correlation between frequencies in f_1 and f_2 resulting from the ABMS shifts is observable in Fig. 3a for the four diagonal peaks as a distinct elongation of the peak shape along the diagonal of the spectrum. However, this shape is far from clear for the off-diagonal peaks, and could be mistakenly attributed to unequal scaling of the two axes (care has been taken in the plotting of the figures to ensure that the range for both axes is identical and that the aspect ratio is 1 : 1). Moreover, the cross-peaks are tilted away from the diagonal. As a result, the correlation of the inhomogeneous broadenings could be overlooked.

The poor quality of the correlation information in Fig. 3a can be traced to two effects: the consequences of Lorentzian-like lineshapes and the effects of t_1 ridges on weak cross-peaks. Fig. 4a and b illustrates the former effect using simulated magnetisation exchange spectra. The overall lineshapes for each peak are the convolution of the 2-D homogeneous fundamental lineshapes and the lineshape due to the inhomogeneous distribution of frequencies. This is modelled here as a Gaussian function aligned along $f_1 = f_2$ corresponding to a 100% correlation between inhomogeneous frequency shifts.

In Fig. 4a, the underlying homogeneous lineshape is Lorentzian. A 2-D Lorentzian lineshape has a variable cross-section and, depending on the contour level, typically has a distinct "star" shape.[13] As seen in Fig. 4a, this non-circular cross-section obscures the correlation of the inhomogeneous line-broadenings since the overall shape is dominated by the 2-D Lorentzian "star". In contrast, a 2-D Gaussian function has a circular cross-section and calculating the same spectra with a 2-D Gaussian function of the same width gives a spectrum in which the correlation of the inhomogeneous broadenings is much clearer, Fig. 3b. Moreover the Gaussian lineshape also decays to the baseline more quickly than a Lorentzian, further improving the effective resolution.

We can perform the equivalent change of lineshape on the experimental spectrum by a Lorentzian-to-Gaussian lineshape transformation prior to Fourier transformation. Fig. 3b is the result of "subtracting" 300 Hz of Lorentzian lineshape (multiplying the time domain data by an appropriate rising
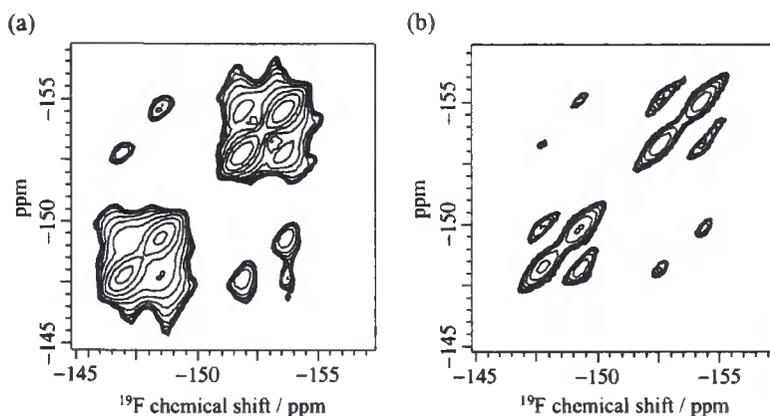
Fig. 3 ^{19}F NOESY/EXSY spectra of octafluoronaphthalene using a short mixing time of 2.3 ms: (a) without lineshape transformation, (b) after Lorentzian–Gaussian transformation (subtracting 300 Hz of Lorentzian linewidth and adding 300 Hz of Gaussian line broadening). The experiments used a 4.5 µs 90° pulse for ^{19}F with 48 time steps in the indirect dimension and a spectral width of 14.66 kHz in the indirect dimension. The sample was spun at 22 kHz and the recycle delay was 16 s.
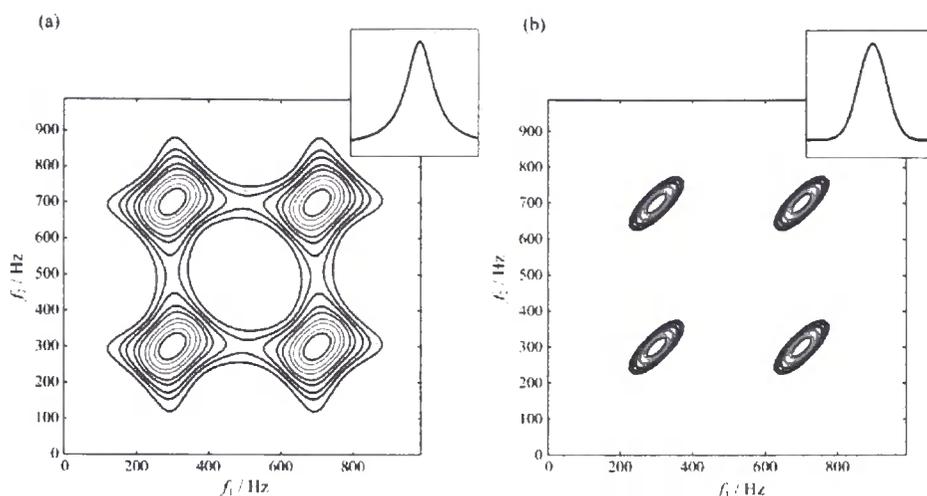
Fig. 4 Calculated 2-D magnetisation exchange line-shapes in which inhomogeneous broadenings between the two sites are perfectly correlated: (a) using a Gaussian lineshape with a width of 100 Hz to represent the inhomogeneous distribution of frequencies and a 30 Hz homogeneous (Lorentzian) fundamental line-shape, (b) as before, but with a 30 Hz Gaussian homogeneous lineshape. The peak shape now clearly reveals the underlying correlation between the inhomogeneous broadenings which is obscured by "star" profile of the homogeneous lineshape in (a). Insets show the respective 1-D Gaussian and Lorentzian lineshapes.

exponential) and adding 300 Hz of Gaussian lineshape. Such a transformation is linear (and hence information-preserving) so there is no risk that such a transformation could introduce artifacts unless an excessively strong apodisation function is applied. This would result in clearly visible high-frequency oscillations ("sinc-wiggles"). Indeed, it can be argued that the original spectrum is a poor representation of the correlation between line frequencies since this "correlation map" is obscured by the convolution with the natural lineshape. It is only when this lineshape is replaced by an "isotropic" function that the underlying correlation information is correctly displayed.

Varying the added Gaussian linewidth will determine whether the overall effect of the lineshape transformation is to smooth the data set (and improve signal-to-noise ratio) or "enhance" the resolution.[18] However, the information-preserving nature of the lineshape transformation means that accurate estimations of homogeneous lineshape are not important, and suitable values for the transformation can be determined by eye.

The spectrum after Lorentzian-to-Gaussian lineshape transformation, Fig. 3b, clearly shows a strong correlation between the inhomogeneous broadenings at different sites. The transformation also significantly sharpens the peaks in anti-diagonal cross-section. This improvement is essentially cosmetic, however; poorly-resolved features will be easier to distinguish after "resolution enhancement", but it will not be possible to resolve features that are not distinct in the 1-D spectrum. Note that ultra-fast magic-angle spinning will have a similar effect in so far as it suppresses the homogeneous component of the linewidth leaving a purely inhomogeneous lineshape. Unfortunately the homogeneous linewidth only decreases as the reciprocal of the magic-angle spinning rate[5] resulting in significant homogeneous linewidths for strongly coupled abundant spins such as ^{19}F and ^{1}H even at the fastest available spinning rates. In this example, for instance, increasing the

MAS rate from 22 to 30 kHz decreases the homogeneous linewidth by only 25% and the overall linewidth by a mere 8%.

Comparing Fig. 3a and b, it is noticeable that the orientation of the cross-peaks between the α and β sites seems to have shifted, with the peaks in (b) now being aligned along the diagonal, as expected. Close inspection of a stack plot of the original data set, Fig. 3, shows this to be a consequence of t_1 ridges.[19] These are reduced, but not entirely eliminated, by adjusting the scaling of the first point prior to Fourier transformation of the direct acquired dimension. Sharpening the peaks by lineshape transformation increases the size of the off-diagonal peaks relative to the ridges, reducing the latter's distorting effects. This leads to the "correct" correlation pattern observed in Fig. 3b.

4. Calculation of chemical shifts

As the NMR experiments are unable to provide an absolute assignment of the individual resonances to the different fluorine sites in the crystal structure, the shielding constants in solid octafluoronaphthalene were calculated by density functional theory using the first principles electronic structure package, CASTEP.[20]

The wavefunction of the system is expanded in a plane wave basis set to an energy cut-off of 1110 eV which converges total energy differences of the system to better than 1.0 meV cell^{-1}. Brillouin zone integration is performed using a Monkhurst-Pack k-point set of a density of 0.05 Å^{-1}. The total energy is then observed to converge to a similar level of accuracy. The optimised structures were determined by relaxed atomic positions within this symmetry group using *ab initio* forces, considering the calculation to have converged when the components of all forces are below 0.01 eV Å^{-1}. We also simultaneously perform relaxation of the unit cell parameters

This journal is © the Owner Societies 2007

Phys. Chem. Chem. Phys., 2007, **9**, 2389–2396 | **2393**

using *ab initio* stresses. Calculations of the NMR properties were performed using the methods described in ref. 21 and as implemented in the CASTEP code.

Calculations were performed using the Perdew-Burke-Ernzerhof (PBE)[22] and Keal-Tozer-3 (KT3)[23] generalised gradient approximation to the exchange–correlation interactions. The former (PBE) is a non-empirical approximation, which is widely used in solid-state physics and describes many physical properties of solid state systems accurately. The latter (KT3) is a semi-empirical approximation which was specifically designed to provide improved quality absolute shielding constants. Initial calculations were performed at the original X-ray structure from the Cambridge Structural Database (reference code OFNAPH01). Calculated NMR parameters are known to be sensitive to atomic positions[24] and since the R-factor for this X-ray structure is rather poor, additional calculations were performed at optimised structures, determined self-consistently using the respective functionals.

As chemical shift referencing is difficult (not least due to bulk susceptibility effects), the calculated shielding values were compared to the experimental *shift* values after reversing the sign and adjusting the mean of the calculated values to match the experimental mean. The results are presented graphically in Fig. 5.

PBE and KT3 give similar results. They correctly predict that the α resonances appear at higher (less negative) chemical shift than the β peaks, although the overall correlation with experimental values is disappointing. In particular, the calculations fail to make clear the α *vs.* β distinction that is observed experimentally, *cf.* Fig. 1c, and the spread of the values is consistently greater than expected. At the X-ray geometry, the F4–F1 chemical shift difference is substantially smaller than

the F3–F2 difference, contrary to experiment. At optimised geometries, the differences are more equalised, but are still well above the experimental values. In line with previous observations, KT3[23] absolute shielding constants (not presented) are uniformly above the PBE values. However, any improvement in absolute shieldings is cancelled when chemical shifts are determined due to the referencing which is invariably applied.

Given the above deviations, it is interesting to make the comparison between solution-state NMR results and calculations for isolated (gas phase) molecules. In the solution-state, the α and β resonances are separated by about 9.1 ppm,[2] which is *larger* than the complete spread of the shifts in the solid-state (6.4 ppm). This is slightly counterintuitive since we might expect differential packing effects to lead to a larger range in the solid. DFT calculations of the ^{19}F shifts for the isolated molecule were performed with the DALTON program,[25] using the Huzinaga III basis set,[26] at cc-pVTZ[27] optimised geometries. Geometry optimisation is essential here since the X-ray structure is not fully symmetrical. PBE and KT3 yield separations of 11.5 and 11.7 ppm, respectively, which are only marginally larger than the experimental value from solution-state NMR.

Although calculations from packages such as CASTEP are proving of great value in assigning NMR spectra from a wide variety of nuclei,[24,28] these results highlight inadequacies in DFT descriptions. This is consistent with previous studies that have demonstrated much larger errors in chemical shift predictions for electronegative atoms such as [19]F.[29–32] Despite their limitations, the calculations do successfully predict the correlation between the pairs of α *vs.* β peaks established from the 2-D correlation spectrum. This provides strong reassurance that the quantum chemical calculations are correctly
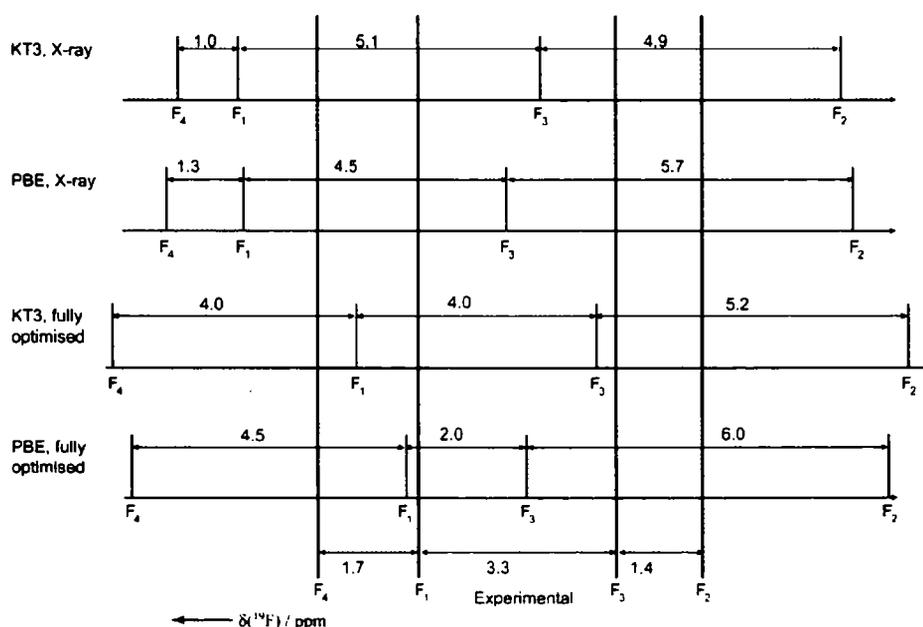

Fig. 5 Comparison of experimental chemical shifts for octafluoronaphthalene with calculated chemical shifts using both optimised and unoptimised geometries, and PBE or KT3 functionals. The mean of each set of calculated shifts has been adjusted to match the mean of the experimental values. Figures give the separations (in ppm) between shift values.

Assignment of ^{19}F resonances to crystallographically distinct fluorine sites using the labelling scheme of Fig. 1b

Observed shift / ppm	Site label
−147.8	F4
−149.3	F1
−152.8	F3
−154.1	F2

predicting the *order* of the chemical shifts, even if the shift values themselves may only be accurate to ±2 ppm. This leads us to propose the assignment summarised in Table 1.

Summary

The ^{19}F NMR of octafluoronaphthalene has been revisited in the light of new developments in the understanding and practice of solid-state NMR. The ^{19}F linewidth was found to be largely inhomogeneous in character *i.e.* most of the decay of the ^{19}F NMR signal is refocused by a spin-echo. This inhomogeneous linewidth could be largely attributed to the large anisotropy of the bulk magnetic susceptibility (ABMS) expected for this material (in turn, due to aromatic ring stacking). As a consequence, the spectral resolution increased significantly on dilution in a material of low ABMS. This phenomenon has favourable implications for the observation of low concentrations of materials susceptible to ABMS broadenings in formulated products. Deliberate sample dilution is not a practical route to improved resolution, however, since the extent of the resolution improvement is difficult to predict *a priori* and unacceptably high degrees of dilution may be required for the effects to be noticeable. Quantum chemical computations have been shown to provide useful estimates of the magnitude of these effects.

Technological and methodological developments, such as higher static magnetic fields, faster MAS rates, and improved decoupling techniques, mean that the inhomogeneous contributions to linewidths are often larger than "homogeneous" contributions from dipolar couplings or motional effects. This distinction is of limited significance in 1-D NMR, but in multi-dimensional NMR the correlations between inhomogeneous broadenings can lead to well-resolved features and significant additional information. However, these correlations may be easily overlooked, or may be distorted by effects of t_1 ridges. We have shown that appropriate processing of the 2-D spectra is important for weak correlations to be correctly characterised. Applying a lineshape transformation that increases Gaussian character of the 2-D lineshapes improves the apparent resolution and ensures that the correlation spectra more closely correspond to plots of the correlation between inhomogeneous broadenings. This will be important if 2-D maps are being used to provide structural information such as bond-angle distributions.

Finally, the combination of DFT calculations with correlation information from multi-dimensional NMR is found to be invaluable in assigning ^{19}F NMR resonances. Comparison between experiment and calculation and between calculations show that individual shifts are predicted with accuracies of about 1% (2 ppm) of the typical ^{19}F shift range which is

significantly poorer than typical experimental resolution. There are clear systematic discrepancies between calculated and experimental shifts which mean that the assignments cannot be made confidently on the basis of calculations alone. On the other hand, simple 2-D homonuclear correlation experiments readily identify sites in close spatial proximity, but are often insufficient in themselves to make a complete assignment to individual sites in the crystal structure. However, the combination of the correlation experiments with the calculated shifts has provided a convincing full assignment in this case and should be readily applicable to more complex cases. Co-workers have recently made other demonstrations of the effective combination of DFT calculation and connectivity (rather than proximity) relationships provided by the solid-state NMR variant of the INADEQUATE experiment.[28]

Acknowledgements

References

1 M. Mehring, R. G. Griffin and J. S. Waugh, *J. Chem. Phys.*, 1971, **55**, 746.
2 R. K. Harris, P. Jackson and G. J. Nesbitt, *J. Magn. Reson.*, 1989, **85**, 294.
3 G. S. Pawley and O. W. Dietrich, *J. Phys. C: Solid State Phys.*, 1975, **8**, 2549.
4 S. P. Brown and H. W. Spiess, *Chem. Rev.*, 2001, **101**, 4125.
5 V. E. Zorin, S. P. Brown and P. Hodgkinson, *J. Chem. Phys.*, 2006, **125**, 144508.
6 D. L. VanderHart, W. L. Earl and A. N. Garroway, *J. Magn. Reson.*, 1981, **44**, 361.
7 A. N. Garroway, D. L. VanderHart and W. L. Earl, *Philos. Trans. R. Soc. London, Ser. A*, 1981, **299**, 609.
8 M. Alla and E. Lippmaa, *Chem. Phys. Lett.*, 1982, **87**, 30.
9 T. Terao, H. Miura and A. Saika, *J. Chem. Phys.*, 1981, **75**, 1573.
10 D. C. Apperley, unpublished results, available on request..
11 D. C. Apperley, R. K. Harris, T. Larsson and T. Malmstrom, *J. Pharm. Sci.*, 2003, **92**, 2487.
12 D. Sakellariou, S. P. Brown, A. Lesage, S. Hediger, M. Bardet, C. A. Meriles, A. Pines and L. Emsley, *J. Am. Chem. Soc.*, 2003, **125**, 4376.
13 T. D. W. Claridge, *High resolution NMR techniques in organic chemistry*, Elsevier Science, Amsterdam, 1999.
14 V. E. Zorin, S. P. Brown and P. Hodgkinson, *Mol. Phys.*, 2006, **104**, 293.
15 A. E. Bennett, C. M. Rienstra, J. M. Griffiths, W. G. Zhen, P. T. Lansbury and R. G. Griffin, *J. Chem. Phys.*, 1998, **108**, 9463.
16 U. Scheler, *Bull. Magn. Reson.*, 1999, **19**, 1.
17 P. Wormald, D. C. Apperley, F. Beaume and R. K. Harris, *Polymer*, 2003, **44**, 643.
18 A. G. Ferrige and J. C. Lindon, *J. Magn. Reson.*, 1978, **31**, 337.
19 R. Freeman, *A Handbook of Nuclear Magnetic Resonance*, Longman Scientific and Technical, 1987.
20 M. D. Segall, P. J. D. Lindan, M. J. Probert, C. J. Pickard, P. J. Hasnip, S. J. Clark and M. C. Payne, *J. Phys.: Condens. Matter*, 2002, **14**, 2717.
21 C. J. Pickard and F. Mauri, *Phys. Rev. B: Condens. Matter Mater. Phys.*, 2001, **63**, 245101.
22 J. P. Perdew, K. Burke and M. Ernzerhof, *Phys. Rev. Lett.*, 1996, **77**, 3865.

This journal is © the Owner Societies 2007

Phys. Chem. Chem. Phys., 2007, **9**, 2389–2396 | 2395

23 T. W. Keal and D. J. Tozer, *J. Chem. Phys.*, 2004, **121**, 5654.

24 M. Profeta, F. Mauri and C. J. Pickard, *J. Am. Chem. Soc.*, 2003, **125**, 541.

25 DALTON; A molecular electronic structure program Release 2.0 see http://www.kjemi.uio.no/software/dalton/, 2005.

26 W. Kutzelnigg, U. Fleischer and M. Schindler, *NMR Basic Principles and Progress*, Springer-Verlag, New York, 1990, vol. 23.

27 T. H. Dunning, *J. Chem. Phys.*, 1989, **90**, 1007.

28 R. K. Harris, S. A. Joyce, C. J. Pickard, S. Cadars and L. Emsley, *Phys. Chem. Chem. Phys.*, 2006, **8**, 137.

29 M. J. Allen, T. W. Keal and D. J. Tozer, *Chem. Phys. Lett.*, 2003, **380**, 70.

30 J. C. C. Chan and H. Eckert, *J. Mol. Struct.*, 2001, **535**, 1.

31 S. Patchkovskii, J. Autschbach and T. Ziegler, *J. Chem. Phys.*, 2001, **115**, 26.

32 J. Poater, E. van Lenthe and E. J. Baerends, *J. Chem. Phys.*, 2003, **118**, 8584.

Bibliography

[1] M. Born and J. R. Oppenheimer, *Ann. Physik* **84**, 457 (1927).

[2] P. Hohenberg and W. Kohn, *Phys. Rev.* **136**, 864 (1964).

[3] W. Kohn and L. J. Sham, *Phys. Rev.* **140**, 1133 (1965).

[4] M. C. Payne et al., *Reviews of Modern Physics* **64**, 1045 (1992).

[5] R. Martin, *Electronic Structure: Basic Theory and Practical Methods* (Cambridge University Press, Cambridge, 2004).

[6] N. W. Ashcroft and N. D. Mermin, *Solid State Physics* (Saunders College Publishing, Philadelphia, PA, 1976).

[7] H. J. Monkhorst and J. D. Pack, *Phys. Rev. B* **13**, 5188 (1976).

[8] J. Phillips, *Phys. Rev.* **112**, 685 (1958).

[9] J. Phillips and L. Kleinman, *Phys. Rev.* **116**, 287 (1959).

[10] M. L. Cohen and V. Heine, *Solid State Physics* **24**, 37 (1970).

[11] L. Kleinman and D. M. Bylander, *Phys. Rev. Lett.* **48**, 1425 (1982).

[12] D. Vanderbilt, *Phys. Rev. B* **41**, 7892 (1990).

[13] E. Polak, *Computational methods in optimization* (Academic Press, New York, NY, 1971).

[14] P. Gill, W. Murray, and M. Wright, *Practical optimization* (Academic Press, London, 1981).

[15] M. P. Teter, M. C. Payne, and D. C. Allan, *Phys. Rev. B* **40**, 12255 (1989).

[16] M. D. Segall et al., *J. Phys.: Condens. Matter* **14**, 2717 (2002).

[17] S. J. Clark et al., *Z. Kristallogr.* **220**, 567 (2005).

[18] P. J. Hasnip, *Bands-parallelism in Castep: A dCSE Project*, http://www.hector.ac.uk/support/cse/distributedcse/reports/ castep/castep_performance_xt.pdf, (2008).

[19] J. C. Kimball, *Phys. Rev. A* **7**, 1648 (1973).

[20] J. P. Perdew and Y. Wang, *Phys. Rev. B* **45**, 13244 (1992).

[21] U. Barth and L. Hedin, *J. Phys. C* **5**, 1629 (1972).

[22] D. Ceperley and B. Alder, *Phys. Rev. Lett.* **45**, 566 (1980).

[23] J. P. Perdew and A. Zunger, *Phys. Rev. B* **23**, 5048 (1981).

[24] R. Jones and O. Gunnarsson, *Reviews of Modern Physics* **61**, 689 (1989).

[25] J. P. Perdew and Y. Wang, *Phys. Rev. B* **33**, 8800 (1986).

[26] J. P. Perdew, K. Burke, and Y. Wang, *Phys. Rev. B* **54**, 16533 (1996).

[27] J. P. Perdew, K. Burke, and M. Ernzerhof, *Phys. Rev. Lett.* **77**, 3865 (1996).

[28] L. A. Curtiss, K. Raghavachari, G. W. Trucks, and J. A. Pople, *J. Chem. Phys.* **94**, 7221 (1991).

[29] A. D. Becke and M. R. Roussel, *Phys. Rev. A* **39**, 3761 (1989).

[30] J. Tao, J. P. Perdew, V. N. Staroverov, and G. E. Scuseria, *Phys. Rev. Lett.* **91**, 146401 (2003).

[31] V. N. Staroverov, G. E. Scuseria, J. Tao, and J. P. Perdew, *J. Chem. Phys.* **119**, 12129 (2003).

[32] V. N. Staroverov et al., *Phys. Rev. A* **70**, 12502 (2004).

[33] J. P. Perdew, J. Tao, V. N. Staroverov, and G. E. Scuseria, *J. Chem. Phys.* **120**, 6898 (2004).

[34] V. N. Staroverov et al., *Phys. Rev. A* **70**, 012502 (2004).

[35] P. Stephens, F. Devlin, C. Chabalowski, and M. Frisch, *J. Phys. Chem.* **98**, 11623 (1994).

[36] A. D. Becke, *Phys. Rev. A* **38**, 3098 (1988).

[37] C. Lee, W. Yang, and R. G. Parr, *Phys. Rev. B* **37**, 785 (1988).

[38] S. Vosko, L. Wilk, and M. Nusair, *Canadian Journal of Physics* **58**, 1200 (1980).

[39] J. P. Perdew, J. Tao, and S. Kümmel, in *Recent Advances in Electron Correlation Methodology*, edited by A. Wilson and K. Peterson (ACS Books, Washington, D.C., 2004).

[40] J. P. Perdew, V. N. Staroverov, J. Tao, and G. E. Scuseria, *Phys. Rev. A* **78**, 052513 (2008).

[41] Z. Yan, J. Perdew, and S. Kurth, *Phys. Rev. B* **61**, 16430 (2000).

[42] F. Furche, *Phys. Rev. B* **64**, 195120 (2001).

[43] M. Fuchs and X. Gonze, *Phys. Rev. B* **65**, 235109 (2002).

[44] J. Dobson, J. Wang, and T. Gould, *Phys. Rev. B* **66**, 81108 (2002).

[45] L. Constantin et al., *Phys. Rev. Lett.* **100**, 36401 (2008).

[46] F. Gygi and A. Baldereschi, *Phys. Rev. B* **34**, 4405 (1986).

[47] A. Seidl et al., *Phys. Rev. B* **53**, 3764 (1996).

[48] A. Görling, *Phys. Rev. B* **53**, 7024 (1996).

[49] M. Städele, J. Majewski, P. Vogl, and A. Görling, *Phys. Rev. Lett.* **79**, 2089 (1997).

[50] M. Städele et al., *Phys. Rev. B* **59**, 10031 (1999).

[51] J. Talman and W. Shadwick, *Phys. Rev. A* **14**, 36 (1976).

[52] J. Krieger, Y. Li, and G. Iafrate, *Phys. Rev. A* **45**, 101 (1992).

[53] J. A. Alonso and L. Girifalco, *Solid State Communications* **24**, 135 (1977).

[54] O. Gunnarsson, M. Jonson, and B. I. Lundqvist, *Solid State Communications* **24**, 765 (1977).

[55] O. Gunnarsson and R. O. Jones, *Physica Scripta* **21**, 394 (1980).

[56] J. P. A. Charlesworth, *Phys. Rev. B* **53**, 12666 (1996).

[57] P. P. Rushton, D. J. Tozer, and S. J. Clark, *Phys. Rev. B* **65**, 235203 (2002).

[58] F. Murnaghan, *Proc. Natl. Acad. of Sci. USA* **30**, 244 (1944).

[59] P. Rushton, Ph.D. thesis, University of Durham, 2002.

[60] R. Feynman, *Phys. Rev.* **56**, 340 (1939).

[61] J. P. Perdew and Y. Wang, *Phys. Rev. B* **46**, 12947 (1992).

[62] D. J. Singh, *Phys. Rev. B* **48**, 14099 (1993).

[63] B. Hammer, K. W. Jacobsen, and J. K. Nørskov, *Phys. Rev. Lett.* **69**, 1971 (1992).

[64] J. A. White and D. M. Bird, *Chem. Phys. Lett.* **213**, 422 (1993).

[65] J. A. White, D. M. Bird, M. C. Payne, and I. Stich, *Phys. Rev. Lett.* **73**, 1404 (1994).

[66] B. Hammer, M. Scheffler, K. W. Jacobsen, and J. K. Nørskov, *Phys. Rev. Lett.* **73**, 1400 (1994).

[67] J. E. Inglesfield and I. D. Moore, *Solid State Communications* **26**, 867 (1978).

[68] Z. Wu, R. E. Cohen, and D. J. Singh, *Phys. Rev. B* **70**, 104112 (2004).

[69] P. H. Acioli and D. M. Ceperley, *Phys. Rev. B* **54**, 17199 (1996).

[70] D. B. Jochym and S. J. Clark, *Phys. Rev. B* **76**, 075411 (2007).

[71] J. Friedel, *Advances In Physics* **3**, 446 (1954).

[72] P. García-González, J. E. Alvarellos, E. Chacón, and P. Tarazona, *Phys. Rev. B* **62**, 16063 (2000).

[73] O. Gunnarsson and B. I. Lundqvist, *Phys. Rev. B* **13**, 4274 (1976).

[74] W. R. Tyson and W. Miller, *Surface Science* **62**, 267 (1977).

[75] A. Forni, G. Wiesenekker, E. J. Baerends, and G. F. Tantardini, *J. Phys: Condens. Matter* **7**, 7195 (1995).

[76] H. Michelsen and D. Auerbach, *J. Chem. Phys.* **94**, 7502 (1991).

[77] O. Gritsenko et al., *Phys. Rev. A* **48**, 4197 (1993).

[78] M. Sadd and M. Teter, *Phys. Rev. B* **54**, 13643 (1996).

[79] P. Dirac, *Proc. Cambridge Phil. Soc* **26**, 70 (1930).

[80] A. D. Becke, *J. Chem. Phys.* **88**, 1053 (1988).

[81] P. Gori-Giorgi and J. P. Perdew, *Phys. Rev. B* **66**, 165118 (2002).

[82] A. Rajagopal, J. Kimball, and M. Banerjee, *Phys. Rev. B* **18**, 2339 (1978).

[83] H. Yasuhara, *Solid State Communications* **11**, 1481 (1972).

[84] A. W. Overhauser, *Canadian Journal of Physics* **73**, 683 (1995).

[85] P. Gori-Giorgi and J. P. Perdew, *Phys. Rev. B* **64**, 155102 (2001).

[86] Z. Qian, *Phys. Rev. B* **73**, 035106 (2006).

[87] P. Gori-Giorgi, F. Sacchetti, and G. B. Bachelet, *Phys. Rev. B* **61**, 7353 (2000).

[88] J. G. Zabolitzky, *Phys. Rev. B* **22**, 2353 (1980).

[89] D. Geldart, *Canadian Journal of Physics* **45**, 3139 (1967).

[90] J. C. Kimball, *Phys. Rev. B* **14**, 2371 (1976).

[91] G. Ortiz, M. Harris, and P. Ballone, *Phys. Rev. Lett.* **82**, 5317 (1999).

[92] M. Gibson, Ph.D. thesis, University of Durham, 2006.

[93] *Landolt-Börnstein - Group III Condensed Matter Numerical Data and Functional Relationships in Science and Technology* (Springer, Berlin, 2006).

[94] G. Kalpana, B. Palanivel, R. Thomas, and M. Rajagopalan, *Physica B: Physics of Condensed Matter* **222**, 223 (1996).

[95] R. T. Poole, J. G. Jenkin, J. Liesegang, and R. C. G. Leckey, *Phys. Rev. B* **11**, 5179 (1975).

[96] A. B. Kunz, *Phys. Rev.* **180**, 934 (1969).

[97] O. Madelung, *Semiconductors-Basic Data* (Springer, Berlin, 1996).

[98] E. Blanca, C. Rodriguez, J. Shitu, and D. Novikov, *J. Phys.: Condens. Matter* **13**, 9463 (2001).

[99] A. Jephcoat, H. Mao, and P. Bell, *Journal of Geophysical Research* **91**, 4677 (1986).

[100] M. Alfredsson et al., *Phys. Rev. B* **70**, 165111 (2004).

[101] http://opium.sourceforge.net/.

[102] C. Bradley and A. Cracknell, *The Mathematical Theory of Symmetry in Solids: Representation Theory for Point Groups and Space Groups* (Clarendon Press, Oxford, 1972).

[103] V. Anisimov, M. Korotin, and E. Kurmaev, *J. Phys.: Condens. Matter* **2**, 3973 (1990).

[104] P. Gori-Giorgi and J. P. Perdew, *Phys. Rev. B* **69**, 041103 (2004).

[105] K. Burke, J. P. Perdew, and M. Ernzerhof, *J. Chem. Phys.* **109**, 3760 (1998).

[106] I. I. Mazin and D. J. Singh, *Phys. Rev. B* **57**, 6879 (1998).

[107] M. Fuchs, M. Bockstedte, E. Pehlke, and M. Scheffler, *Phys. Rev. B* **57**, 2134 (1998).

[108] E. Engel et al., *Phys. Rev. B* **64**, 125111 (2001).

[109] Z. Wu et al., *Phys. Rev. B* **69**, 085104 (2004).

[110] J. Perdew and K. Schmidt, in *Density Functional Theory and Its Application to Materials*, edited by V. V. Doren, C. V. Alsenoy, and P. Geerlings (American Institute of Physics, Melville, NY, 2001).

[111] I. Gradshteyn and I. Ryzhik, *Table of Integrals, Series and Products (corrected and enlarged edition)* (Academic Press, London, 1980).